Theses and Dissertations

8-2018

Opto-Thermal Characterization of Plasmon and Coupled Lattice Resonances in 2-D Metamaterial Arrays

Vinith Bejugam
University of Arkansas, Fayetteville

Follow this and additional works at: https://scholarworks.uark.edu/etd

Part of the Electromagnetics and Photonics Commons, Nanoscience and Nanotechnology Commons, Sustainability Commons, and the Thermodynamics Commons

Opto-Thermal Characterization of Plasmon and Coupled Lattice Resonances in 2-D
Metamaterial Arrays

A dissertation submitted in partial fulfillment
of the requirements for the degree of
Doctor of Philosophy in Engineering

by

Vinith Bejugam
Jawaharlal Nehru Technological University
Bachelor of Technology in Chemical Engineering, 2012

August 2018
University of Arkansas

This dissertation is approved for recommendation to the Graduate Council.

_____
D. Keith Roper, Ph.D.
Dissertation Director

_____   _____
Jerry A. Havens, Ph.D.   Robert R. Beitle, Ph.D.
Committee Member   Committee Member

_____   _____
Charles L. Wilkins, Ph.D.   Rick L. Wise, Ph.D.
Committee Member   Committee Member

ProQuest Number: 10841542

ProQuest 10841542

ABSTRACT

Growing population and climate change inevitably requires longstanding dependency on sustainable sources of energy that are conducive to ecological balance, economies of scale and reduction of waste heat. Plasmonic-photonic systems are at the forefront of offering a promising path towards efficient light harvesting for enhanced optoelectronics, sensing, and chemical separations. Two-dimensional (2-D) metamaterial arrays of plasmonic nanoparticles arranged in polymer lattices developed herein support thermoplasmonic heating at off-resonances (near-infrared, NIR) in addition to regular plasmonic resonances (visible), which extends their applicability compared to random dispersions. Especially, thermal responses of 2-D arrays at coupled lattice resonance (CLR) wavelengths were comparable in magnitudes to their counterparts at plasmon wavelengths. Opto-thermal characterization of 2-D arrays was conducted with a white light irradiation in the current work. Finite element analysis involving a three-dimensional (3-D) COMSOL model mimicked the heat transfer and average temperature increases in these systems at plasmon resonances with a ≤ 0.5 % discrepancy at the absorbed, extinguished power of the radiation. All-optical, mesoscopic characterization of 2-D arrays involving trichromatic particle analysis allowed detailed investigation of effects of particle populations and ordering on the optical signals of plasmon and CLR in addition to indicating a critical point of emergence for CLR. Overall, engineering these thermoplasmonic metamaterials for enhanced optothermal dissipation at visible to near-IR radiation supports their rapid implementation into emerging sustainable energy and healthcare systems.

ACKNOWLEDGEMENTS

DEDICATION

I dedicate this dissertation to my incredible Bejugam family. No matter what happens, they will

be with me through thick and thin.

TABLE OF CONTENTS

LIST OF FIGURES

LIST OF TABLES

NOMENCLATURE

Chemical Symbols, Acronyms, and Abbreviations

Ag	Silver
Au	Gold
AU	Absorbance Units
AuNP	Gold Nanoparticle
BF	Bright Field
CDA	Coupled Dipole Approximation
CLR	Coupled Lattice Resonance
CVD	Chemical Vapor Deposition
DDA	Discrete Dipole Approximation
DF	Dark Field
DI	Deionized Water
DNA	Deoxyribonucleic Acid
EBL	Electron Beam Lithography
EELS	Electron Energy Loss Spectroscopy
EL	Electroless plating
EUV-IL	Extreme Ultraviolet Interference Lithography
FIB	Focused Ion Beam
FGMS	Fixed Glass and Mobile Substrate
FOI	Field-of-Illumination

FOV	Field-of-view
Ge	Germanium
HCI	Hot Carrier Injection
HER	Hydrogen Evolution Reaction
IR	Infrared
ITU	International Telecommunion Union
LMS	Long, Medium, and Short Wavelengths of Light
LPR	Lattice Plasmon Resonance
LSPR	Localized Surface Plasmon Resonance
MoS2	Molybdenum Disulfide
MoSe2	Molybdenum Diselenide
NIL	Nanoimprint Lithography
NIR	Near-Infrared
NP	Nanoparticle
NSL	Nanosphere Lithography
1-D	One-Dimensional
PDMS	Polydimethylsiloxane
PDMS-b-PEO	Poly(dimethylsiloxane-b-ethyleneoxide)
PDMS-PEO	Poly(dimethyloxane-ethyleneoxide)
PH	Peak Height

Pt	Platinum
RGB	Red, Green, and Blue (Linear Form)
R'G'B'	Red, Green, and Blue (Non-Linear Form)
ROI	Region of Interest
rsa-CDA	Rapid Semi-Analytical Solution, Coupled Dipole Approximation
SEM	Scanning Electron Microscopy
SHG	Second Harmonic Generation
SiO2	Silicon Dioxide
SPR	Surface Plasmon Resonance
TMD	Transition Metal Dichalcogenide
2-D	Two-Dimensional
WS2	Tungsten Disulfide

Symbols and Popular Units

d	Interparticle Distance [nm]
ω	Eigenmode Frequency or Natural Frequency of the Oscillator [rad s^{-1}]
γ	Linear Damping Coefficient [dimensionless]
a	Amplitude of the External Force [units vary] or Radius of the Sphere [nm]

c	Steady-State Amplitude of the Oscillator [units vary]
v	Coupling Factor [dimensionless] or Kinematic Viscosity of the fluid [m^2 s^{-1}]
θ	Phase Shift [rad]
$|i\rangle$	Incident Photon [dimensionless]
$|c\rangle$	Continuum State [dimensionless]
$|d\rangle$	Discrete State [dimensionless]
q	Excitation Probability Ratio[dimensionless] or Heat Flux [W m^{-2}]
w	Coupling Factor Corresponding to Discrete State [dimensionless]
g	Coupling Factor Corresponding to Continuum State [dimensionless] or Acceleration Due to Gravity [m s^{-2}]
ε	Reduced Energy [eV], Electric Permittivity [F m^{-1}], or Emissivity of the material [dimensionless]
E	Energy of Incident Photon [eV] or Incident Field [V m^{-1}]
Γ	Line width [nm]
Y	Luma or Photometric Brightness [dimensionless]
σ	Cross Section [m2] or Stefan-Boltzman Constant [~5.67e-8 W m^{-2} K^{-4}]
α	Polarizability [C m^2 V^{-1}] or Thermal Diffusivity of the

Fluid [m^2 s^{-1}]

Q Efficiency [dimensionless]

P Polarization [C m^{-2}]

S Retarded Dipole Sum [dimensionless]

k Wavevector [rad per unit distance] or Thermal Conductivity

                     [W m^{-1} K^{-1}]

ρ Density of the Material [Kg m^3]

C_p Specific Heat Capacity of the Material [KJ K^{-1}]

T Temperature [K]

n Normal vector to the film surface [dimensionless]

∇ Del Operator [dimensionless]

t Time [s]

Q Total Heat Sources or Sinks [W m^{-2}]

h Heat Transfer Coefficient [W m^2 K^{-1}]

L Plate Height [m]

Ra Rayleigh Number [dimensionless]

Pr Prandtl Number [dimensionless]

β Coefficient of Thermal Expansion [K^{-1}]

Θ Dimensionless Temperature

η Dimensionless Distance

x Length of the Slab [m]

Subscripts

o	Initial Condition
p	Plasmon (Continuum Resonance) or
	Specific Heat Capacity
d	Discrete Resonance
m	Modified Line Width of Discrete Resonance
x	Absorption, Scattering, or Extinction
1	Specific Temperature Value
inf	Ambient temperature of the Fluid
inc	Incident Field

Superscript(s)

$'$	Non-Linear Representation of Luma

1.   INTRODUCTION

This chapter primarily focuses on the motivation for the present work, and introduction of plasmon and Fano dual-resonances. Models pertaining to classical and quantum physics will be introduced that describe these dual-resonances in metamaterial arrays. This chapter finally ends by enumerating key advances of the present work, and an overall summary.

1.1 Motivation

1.1.1. Sustainable energy

Population explosion in the last 60 years led to an increased demand of global energy.[1,2] According to a recent estimate, power consumption in 2050 would be around 30 TW compared to 17 TW today which would correspond to a 1.7-fold increase.[3] Primary sources of energy, i.e., fossil fuels have already been on the verge of decline. Conversely, coal reserves will remain intact for a long time;[4] nevertheless, both fossil fuels and coal contributed largely to greenhouse effect (carbon dioxide emissions) resulting in global warming.[5] In 2015-16, world economies agreed upon two important sets of goals for future considering the current environmental conundrums: Sustainable Development Goals and the Paris Agreement on Climate Change action for phasing out fossil fuels by 2100.[6] Sustainable energy for: supporting escalating demands of growing population, complementing ecological balance, and reducing waste heat is imperative in the current global scenario.

Sustainable energy sources such as wind,[7] geothermal,[8] solar,[9] fuel cells[10] and biofuels[11] have already been on the rise for the past 50 years.[12] A crossover between plasmonics and photonics in recent decades paved the path for utilization of plasmonic nanomaterials for progressive advancement of some of these systems at the lab scale. Specific examples include augmentation

1

of electron-hole pairs, i.e., excitons (and photocurrent) in solar photovoltaics,[13] and efficient catalytic activity in fuel cells.[14] However, challenges pertaining to ohmic losses limit the performance of these plasmonic systems.[15,16] This work focuses on thermalization aspects of plasmonic nanomaterials arranged into two-dimensional (2-D) arrays in polymer media, and implementation of such systems for applications requiring enriched energy dissipation.

1.1.2. Healthcare

Viable interactions of biological substances such as peptides, deoxyribonucleic acid (DNA), antigens, and oligonucleotides with functionalized nanomaterials *via* ligand transfer, covalent bonding or passive adsorption has resulted in unique applications of plasmonic nanomaterials in therapeutics, point-of-care diagnostics, anti-bacterial activity, ablation of cancer cells, and drug delivery.[17–23] For example, energy exchange between conductive nanoparticles (NPs) and redox proteins (e.g. cytochrome) supports development of amperometric biosensors wherein redox enzymes act as sensing entities, and NP arrays function as the conductive matrix onto which the enzyme molecules adhere.[17] The changes in surrounding dielectric due to external biomolecules/biological specimens affect the overall system-sensitivity in tandem with opto-thermal responses of such arrays.[17,20] Understanding the dynamic energy exchange pathways in these systems vis-à-vis plasmonic dissipation and thermal changes due to 'diffractive coupling' in NP arrays is imperative for further advancement of these nano-bio-photonic systems.

1.2. Background

1.2.1. Plasmon resonance

Surface plasmon resonance (SPR) is a surface phenomenon where conduction electrons in noble metals such as gold (Au), silver (Ag), and platinum (Pt) collectively oscillate at a resonant

2

frequency of the incident light. Unlike metallic surfaces, NPs owing to a large-surface area-to-volume ratio (ca.10^7:1 ratio for a 10 nm NP compared to a regular cricket ball) have an exceptional tendency to scatter and absorb light. Geometric confinement of plasmons at the metal-dielectric interface of a NP leads to a localized surface plasmon resonance (LSPR), which is dependent on particle shape, size, and the surrounding dielectric environment.[24–29] Figure 1 schematically shows formation of dipoles in NPs due to a light wave with wavevector k propagating from left to right with an orthogonal electric field (y-polarization).
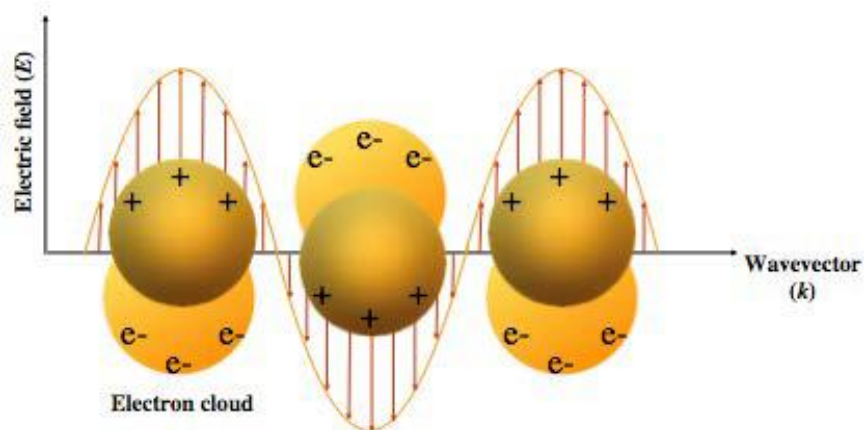
Figure 1. Electron cloud oscillations in plasmonic NPs induced by light with wave vector k and electric field E.

As the LSPR decays, excited electron cloud couples with phonons, or crystal lattice vibrations, resulting in an increase in thermal energy. This thermal energy is eventually dissipated to the surrounding environment *via* phonon-phonon interactions.[30–32] Thermoplasmonic heating in NPs induced by electromagnetic radiation has been used for applications pertaining to solar photovoltaics and healthcare, as outlined in the preceding sections, and advancements in microelectronics for over 50 years which led to the progressive increase in computing power at decreased relative costs (Moore's law).[33] Figure 2a (inset), for example, shows the extinction response in absorbance units (AU) of a random ensemble of AuNPs on soda lime glass (Figures

2a and 2b) deposited *via* tin pre-sensitization on glass and electroless (EL) plating of AuNPs.[34]

The maxima of the LSPR occurred at ca. 560 nm.
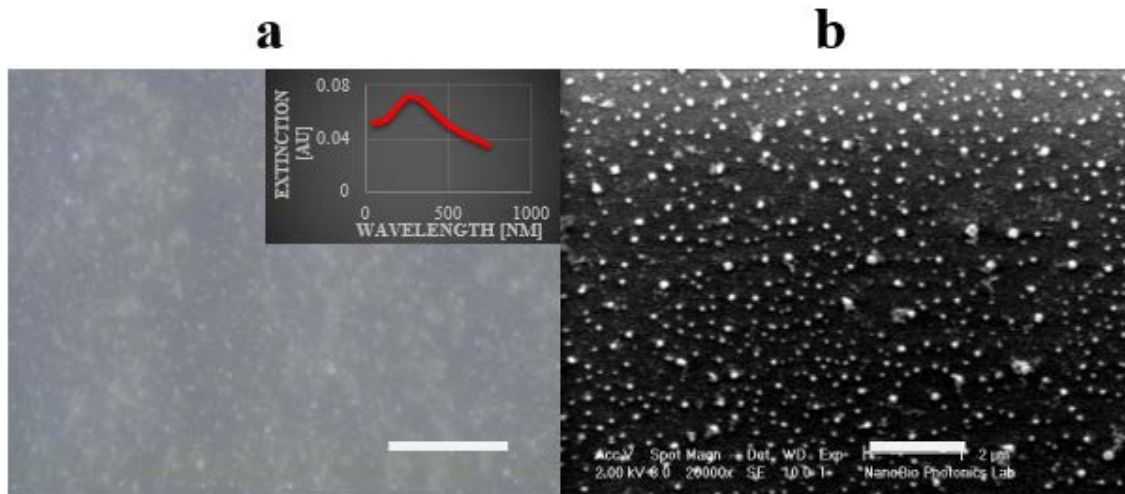
Figure 2. a) 20x dark field (DF) microscope image (scale bar: 50 μm) of the sample with its corresponding LSPR response in the inset, and b) shows an SEM image of random AuNPs of sizes 20-50 nm (scale bar: 2 μm).

1.2.2. Fano resonance (coupled lattice resonance)

Italian-American physicist Ugo Fano was the pioneer in exploring asymmetric peaks arising from coupling between a discrete resonance and a broadband resonance. [35] Fano resonances can be observed in many areas of physics and engineering. The focus of this work is to describe the Fano resonance occurring in 2-D arrays. AuNPs ordered into 2-D arrays support coupling of a plasmon-enriched local electromagnetic field to diffracted light, resulting in a coupled lattice resonance (CLR)/Fano resonance. For example, Figure 3 shows a 2-D array (100 μm x74 μm) of 13223 sites filled with AuNPs, and 700 nm lattice spacing (grating constant). The inset shows the extinction peak of the array, where CLR feature appears at ca.725 nm due to periodic arrangement in addition to a lattice plasmon resonance (LPR) feature that appears at ca. 560 nm. Note that the CLR feature was absent in the inset of Figure 1a for random ensembles.
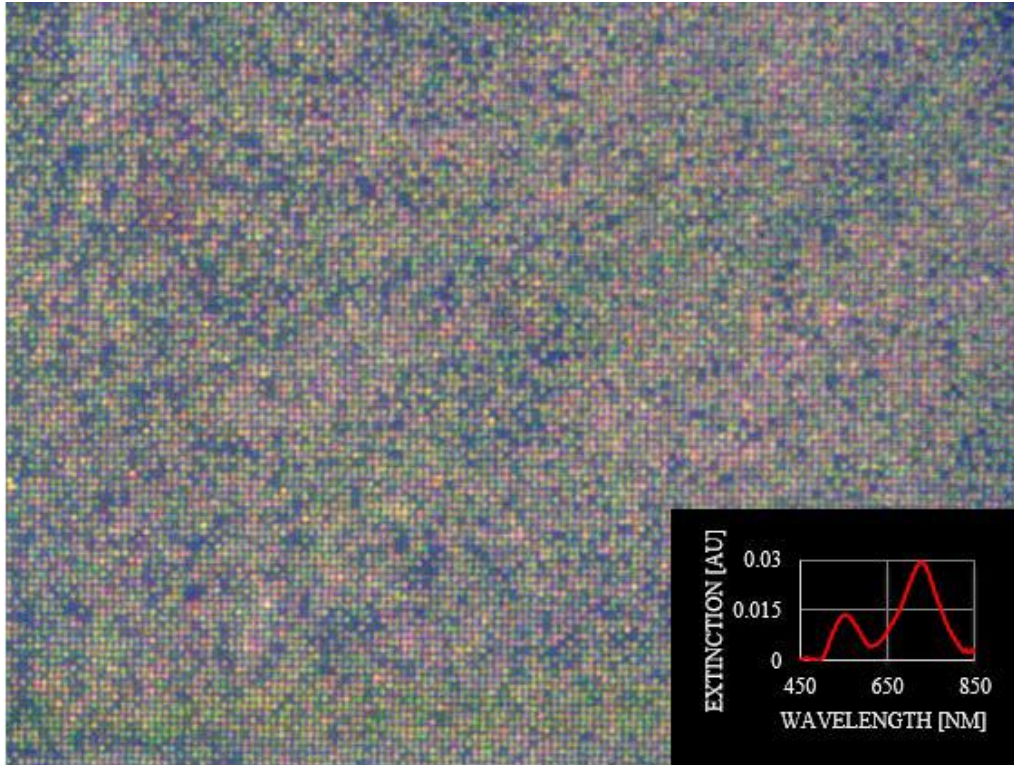
Figure 3. 2-D array (100 μm x74 μm) with 13223 filled AuNP sites and 700 nm lattice spacing; inset shows the extinction spectrum of the array with CLR and LPR peaks at ca.725 and ca.560, respectively.

The LPR and CLR features can be generally tuned in relation to the polarization of the incident electromagnetic field,[36] grating constant,[37] NP geometry[28,29], and refractive index of the medium.[38] This work particularly shows important effects of particle density on the intensity of LPR and CLR features.

Figure 4 schematically illustrates a square lattice of NP sites (nodes) subjected to orthogonal incidence (into the plane) of light with x-polarization. The periodic, center-to-center spacing between the nodes is d. The diffractive modes in the upper right-hand quadrant are shown vis-à-vis a reference black node at the center. Nodal elements in axial (y-axis), and diagonal (y=x) are green and red, respectively. Remaining nodes in off-axial and off-diagonal (OAD) directions are violet. Nodes separated by $2d$ are lighter in color than their counterparts at a spacing 'd' within a

5

chain of each diffractive mode. Constructive and destructive interferences are illustrated with respect to the direction of wave propagation.
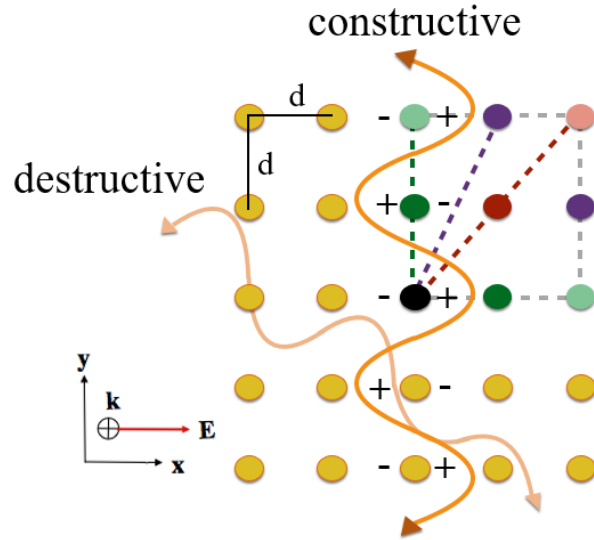
Figure 4. Constructive and destructive interference in a square lattice with periodic, center-to-center spacing 'd' between nodes (NP sites) under normal incidence of light that is x-polarized. The diffractive modes in axial (green), diagonal (red) and OAD (violet) in the upper right quadrant are illustrated with respect to a black node as a reference point. Nodes separated by '2d' are lighter in color.

Nodes present along the direction of polarizability (x-axis) are not conducive to far-field diffraction coupling, as dipoles do not radiate along their dipole moment.[39,40] Square lattices ($d_x = d_y$) represent a special case of rectilinear lattices and exhibit $\pi/2$ rotational symmetry for an isotropic response to x- and y-polarization. The present work primarily considered far-field diffractive coupling effects from square lattices. Far-field effects are predominant, with a dependence of d^{-1}, when the interparticle distance (d) is greater than the size of the NP, and near or above LSPR wavelength (λ_{LSPR}) of the NP. Near-field interactions dominate and show a d^{-3} dependence as the interparticle distance decreases to dimensions comparable to NP size. [41,42]

Two models pertaining to classical and quantum-mechanical theories of dual-resonant systems were reported in literature, which have an important relevance to the present work. The following discussion will focus on the illustration of these models.

Systems exhibiting dual-resonances has been famously expounded by the classical model of harmonic oscillators.[43] Consider two oscillators coupled by a weak spring, as shown in Figure 5, where and external force is driving oscillator ω_1.
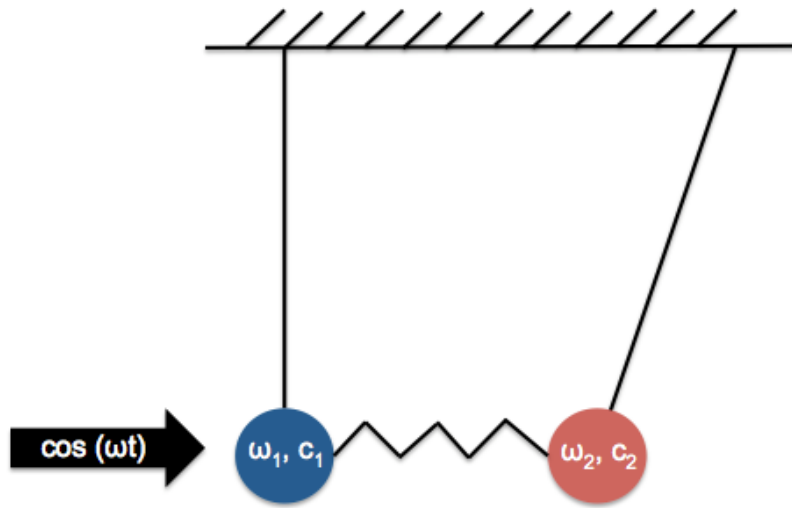
Figure 5. Two-coupled harmonic oscillator system.

The equations of motion for these oscillators may be written as:

$$\ddot{x}_1 + \gamma_1 \dot{x}_1 + \omega_1^2 x_1 + v_{12} x_2 = a_1 e^{i\omega t} \tag{1.1}$$

$$\ddot{x}_2 + \gamma_2 \dot{x}_2 + \omega_2^2 x_2 + v_{12} x_1 = 0 \tag{1.2}$$

where ω_1 and ω_2 are the natural frequencies/eigenmodes of oscillators, γ_1 and γ_2 are linear damping coefficients, v_{12} corresponds to the coupling of oscillators, ω is the external driving frequency, and a_1 is the amplitude of the external driving force.

The coupling term is zero in the event of no external force acting on the system, i.e., oscillators swing independently according to their natural frequencies. But coupled oscillators have two normal modes (eigenmodes): a) oscillators swing to and fro together, and b) oscillators swing in opposite directions. The coupled eigenmodes in this system are expressed as follows:

$$\bar{\omega}_1^2 \approx \omega_1^2 - \frac{v_{12}^2}{\omega_2^2 - \omega_1^2} \tag{1.3}$$

$$\bar{\omega}_2^2 \approx \omega_2^2 + \frac{v_{12}^2}{\omega_2^2 - \omega_1^2} \tag{1.4}$$

where $\bar{\omega}_1$ and $\bar{\omega}_2$ are the displaced eigenmodes due to the coupling between oscillators. The amplitudes for these oscillators from the steady-state harmonic solutions of Equations 1.1 and 1.2 are:

$$c_1 = \frac{\omega_2^2 - \omega^2 + i\gamma_2\omega}{(\omega_1^2 - \omega^2 + i\gamma_1\omega)(\omega_2^2 - \omega^2 + i\gamma_2\omega) - v_{12}^2} a_1 \tag{1.5}$$

$$c_2 = \frac{v_{12}}{(\omega_1^2 - \omega^2 + i\gamma_1\omega)(\omega_2^2 - \omega^2 + i\gamma_2\omega) - v_{12}^2} a_1 \tag{1.6}$$

where c_1, and c_2 are the steady-state amplitudes for these oscillators. The phases of the two oscillators are defined by:

$$c_1(\omega) = |c_1(\omega)|e^{-i\varphi_1(\omega)} \tag{1.7}$$

$$c_2(\omega) = |c_2(\omega)|e^{-i\varphi_2(\omega)} \tag{1.8}$$

where the phase difference and phase shift (θ) are given as:

$$\varphi_2 - \varphi_1 = \pi - \theta \tag{1.9}$$

$$\theta = tan^{-1}\left(\frac{\gamma_2\omega}{\omega_2^2 - \omega^2}\right) \tag{1.10}$$

Increasing the coupling factor, v_{12}, diminishes the coupled eigenmode frequency of oscillator 1, $\bar{\omega}_1^2$ (Equation 1.3), and causes a red-shift in wavelength (due to a reciprocal relation between frequency and wavelength). But eigenmode frequency of oscillator 2, $\bar{\omega}_2^2$ (Equation 1.4), would increase showing a concomitant blue-shift in wavelength. Imagine a simplest case when the frictional parameter (damping coefficient), γ_1, is zero from Equation 1.5. When an external force drives the frequency of the first oscillator close to that of the second oscillator, c_1 becomes zero. This frequency is referred to as zero-frequency, which induces an asymmetric profile that is commonly associated with a small dip. [43] This model could be primarily used to understand the energy shifts associated with coupling between continuum (plasmon) and discrete (lattice diffraction) states of square lattices.

A quantum mechanical equivalent of classical model was reported recently that delves deeper into the nature of continuum and discrete resonances in terms of three coupling factors.[44,45] Imagine a system where an incident photon, $|i\rangle$, excites either a continuum state ($|c\rangle$) with coupling factor g, or a discrete state ($|d\rangle$) with coupling factor w. Also, continuum and discrete states interact with a certain coupling strength v. Equation 1.11 represents the Fano profile of this system where ε is the reduced energy, and q is the excitation probability ratio (asymmetry parameter):

$$F(\varepsilon) = \frac{(\varepsilon+q)^2}{\varepsilon^2+1} \tag{1.11}$$

Equation 1.12 represents q in terms of v, w, and g, energy of the incident photon (E), plasmon energy (E_p), plasmon linewidth (Γ_p), and modified linewidth of the discrete resonance, $\Gamma_m(E)$, with an energy of (E_d):

$$q = \frac{vw/g}{\Gamma_m(E)/2} + \frac{E-E_p}{\Gamma_p/2} \tag{1.12}$$

The reduced energy (ε) may be written as:

$$\varepsilon = \frac{E}{\Gamma_m(E)/2} + \frac{E-E_p}{\Gamma_p/2} \qquad (1.13)$$

Equations 1.14 shows the relation between the modified linewidth of discrete state and

Lorentzian profile of plasmon resonance (Equation 1.15):

$$\Gamma_m(E) = 2\pi v^2 L(E) \qquad (1.14)$$

$$L(E) = \frac{1}{1+(\frac{E-E_p}{\Gamma_p/2})^2} \qquad (1.15)$$

The important insight that can be gained from this analytical model is that there is a probability to

excite either a discrete state (w) or a continuum state (g) first by an incident photon, and these

resonances interact *via* a coupling strength (v).[44,45] Figure 6 illustrates the essence of this model,

where the putative discrete resonance is shown by a sharp profile ($\frac{q^2-1}{\varepsilon^2+1}$), and continuum resonance

follows a flat profile (1). The mixing condition is represented by $\frac{q^2-1}{\varepsilon^2+1}$. The resultant Fano profile

is generally represented as shown in Equation 1.11. [35,46]
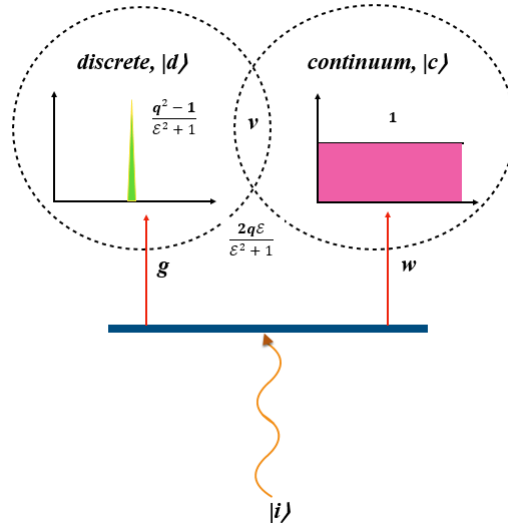
Figure 6. An incident photon, |i⟩, can either excite a discrete resonance (|d⟩) with a coupling factor w, or a continuum resonance (|c⟩) with a coupling factor g. A coupling strength v forms between the discrete and continuum states.

1.3. Key advances of the present work

The significant advances made in this study are:

1. Creation of 2-D metamaterial arrays using template-assisted self-assembly *via* modification of polydimethylsiloxane (PDMS) with poly (dimethylsiloxane-b-ethylene oxide) (PDMS-b-PEO).

2. Opto-thermal characterization of 2-D metamaterial arrays in visible as well as near-infrared (NIR) wavelengths.

3. Energy dissipation from 2-D arrays at CLR resonances (NIR) in addition to plasmon reosnances (visible).

4. Extension of three-dimensional (3-D) slab model (COMSOL) for embedded NPs into a dual-slab model (2-D lattices on a film)

5. Implementation of an all-optical approach that includes image analysis and statistical analysis for characterizing metamaterial arrays.

1.4. Summary

Integration of plasmonics with photonics paved the path for key research opportunities for advancement of sustainable energy and healthcare systems. Enhanced energy generation due to plasmon-photon interactions could result in *economies of scale* in the long-run concerning production of biofuels, or order-of-magnitude increases in electron-hole pair generation and photocurrent in solar photovoltaics. Plasmonic/photonic metamaterials with augmented opto-thermal responses and energy dissipation pathways could be used for diagnosing biological molecules, direct thermal ablation of cancer cells, drug delivery, etc. Particularly, 2-D metamaterial arrays which exhibit diffractive coupling as a result of interaction of lattice diffraction with plasmons can be used to provide alternate energy dissipation pathways. The

concept of plasmon and Fano coupled lattice resonances (CLR) in 2-D arrays has been delineated in detail by considering deep-rooted models of Physics: classical analogy of harmonic oscillators and quantum-mechanical analytical model. Key advances in the present work have been enumerated, which will be discussed in detail in ensuing chapters.

2. FABRICATION OF 2-D ARRAYS

This chapter deals with traditional methods for fabrication of 2-D arrays, template-assisted self-assembly methods discussed in literature thus far, soft lithography for creating nanoimprinted PDMS-PEO square lattices, and variations of template-assisted self-assembly for depositing AuNPs in the cavities of PDMS-PEO lattices used in the present work.

2.1. Fabrication methods

Some of the traditional methods for creating 2-D arrays are listed as follows:

a) Electron beam lithography (EBL) allows intricate, user-defined patterning through lithography of a polymeric resist by an electron beam.[47,48]

b) Focused ion beam (FIB) entails milling of substrates using gallium (Ga) ion beams and offers high precision.[49,50]

c) Nanosphere lithography (NSL) involves masking of a substrate during metallization using colloidal spheres, where sphere dimensions govern the lattice spacing.[51,52]

d) Nanoimprint lithography (NIL) exploits a master image pre-lithographed using electron/ion beam or interference to mold template patterns onto substrates using resists.[53–55]

e) Soft lithography uses a pre-lithographic master stamp created by one of these top-down approaches to pattern a PDMS polymer. The negative geometry of the master is transferred to the polymer. Soft lithography is commonly used for applications involving microfluidics.[56,57]

2.2. Template-assisted self-assembly

2-D arrays of NPs could be produced inexpensively using bottom-up methods compared to top-down methods using self-assembly techniques such as colloidal/nanosphere lithography,[51,52,58] and template-assisted self-assembly.[59–64] Template-assisted self-assembly, in particular, has recently gained interest, owing to its economic viability and efficacy over other self-assembly techniques that depend on interfacial and inter-particle forces. Additionally, customized templates allow leverage over dense packing of NPs.[60] Chemical functionalization and topographical patterning of substrates is commonly employed for homogeneous distribution of forces that guide the particles to periodic cavities with special geometrical shapes. Packing density of cavities and overall lattice spacing could be tunable for multivalent applications. Commonly exploited forces/processes in template-assisted self-assembly are electrostatic, magnetic, convection, capillary, sedimentation, host-guest interactions, etc.

Table 1 summarizes template-assisted self-assembly techniques which were based primarily on capillary and convective forces. These techniques can be further grouped into two types: a) solvent enclosed between a fixed glass and mobile substrate (FGMS), and b) dip coating, where a template is immersed in a NP suspension.

Table 1. Template-assisted self-assembly methods involving capillary and/or convective forces.

Substrate	Templating method	Treatment	NP (size, nm)	NPs/mL	Cavity (holes) (nm)	Parameters		Self-assembly
						V_s [d] (μm/s)	T_s [e] (°C)	
PDMS bilayer[59]	Soft-lithography	O_2 plasma (substrate)	Au (88)	3e+10	D[a]=580 H[b]=140 P[c]=1300-1400	0.6	21	FGMS[f]
PDMS[60]	Soft-lithography	O_2 plasma (substrate)	Au (100)	5.6e+9 (Au)	D=120 H=80	0.2	28	FGMS
Mylar films[61]	Photo-lithography	none	PS beads (700-4300)	NA [g]	D=2000-6000 H=2000-5500	0.3	NA	FGMS
PMMA on Cr/SiO$_2$-Si[62]	EUV-IL	none	Au (15-50); Si (45-50)	4.5e+10 - 1.7e+14 (Au); 4.3e+11- 4.3e+14 (Si)	P=70-115	0.5	NA	Dip coating
SiO$_x$ layer on top of Si[63]	EBL	none	Au (50)	4.5e+10	D=50-110 H=ca.60	0	60	Dip coating
PDMS[64]	Soft-lithography	Triton X-45 and dodecyl sulphonate (surfactant for colloidal suspension)	Au (60-100)	2e+11	H=40-45 P[f]=280-1000	0.3	27	FGMS
Present work	Soft-lithography	PEO (substrate)	Au (80-100)	1e+8-1e+9	D=195-260 H=150-350 P=600-700	0	25	FGMS

[a] diameter; [b] height; [c] pitch; [d] substrate/dip velocity; [e] substrate temperature; [f] solvent trapped between a fixed glass and movable substrate; [g] not available

Especially, the FGMS technique entails moving a substrate on motorized platforms at low velocities. Evaporation-induced convective transport of solvent in conjunction with capillary forces support NP depositions into cavities near the receding contact line of solvent. Substrate velocity in μm/s, and substrate temperature can be controlled relative to NP volume to obtain ordered NP deposition. Dip coating, on the other hand, involves substrate immersion in a NP suspension. The dip velocity, NP concentration and solvent temperature can be tuned to monitor the deposition process. Templates of diverse materials such as mylar films, PDMS, and SiO$_x$ have

been used in these techniques. In particular, PDMS has been widely used owing to its extensive applications in microfluidics.

The present work led to the design and fabrication of 2-D arrays based on FGMS technique. In contrast to intricate methods such as extreme ultraviolet interference lithography (EUV-IL), EBL and FIB, soft-lithography was used to create templates comprised of PDMS and PEO for the self-assembly process.

Table 2 shows the figures of merit of template-assisted methods listed in Table 1. Varying the concentration of NP solvent, and lattice configuration permitted formation of NP ensembles with varying spatial conformations (monomers to heptamers) in FGMS systems. Ensemble types ranging from monomers to dodecamers were reported with assorted lattice geometries in dip coating. Cluster yields varied from 32% (PDMS) to 90% (mylar).

Table 2. Figure of merits for template-assisted methods listed in Table 1.

Ensemble Conformations	Yield (%)	Characterization Method	Optical Resonances
Heptamers[59]	32 (PDMS)	SEM	Plasmon and Fano
Monomers[60]	NA	SEM	NA
Monomer, dimers, trimers, tetramers, pentamers[61]	ca.90 (mylar)	SEM	NA
Monomers at interstitial sites[62]	NA	SEM	NA
Monomers[63]	NA	SEM	NA
Monomers[64]	NA	SEM	NA

Characterization methods mostly involved analyzing ensembles with SEM. The proposed work includes alternate characterization methods such as diascopic and episcopic microscopy and image analysis. Charging effects on an insulating surface such as PDMS due to electron imaging techniques at high vacuum conditions may deteriorate the quality of images. Ultra-thin conductive coating on PDMS for SEM was further avoided, as it may cause the opto-thermal responses of samples to alter.

16

2.2.1. Enhancement of PDMS surface energy using PDMS-b-PEO copolymer

PDMS is fundamentally hydrophobic owing to a low surface free energy compared to water (PDMS: 20 mN/m; water: 72 mN/m).[65,66] Numerous techniques to increase the surface energy of PDMS have been attempted previously such as sol-gel coatings, oxygen plasma, UV/ozone, layer-by-layer deposition, chemical vapor deposition (CVD), etc.[59,60,67,68] However, PDMS is resilient to these treatments and recovers its hydrophobic nature eventually due to low glass transition temperature (-120 ˚C).

PDMS-b-PEO diblock copolymer was used in the present work to rapidly increase the surface energy of PDMS after mixing and curing steps with PDMS. Yao *et al.* [69] noted that the water contact angles decreased from 100˚ to 20˚ (5-fold) upon increasing the concentration of PDMS-PEO from 0% to 1.9%. Modulating the cross-linking density would allow further manipulation of the wetting property of PDMS.[70]

2.2.2. Soft Lithography for creating nanoimprinted polymer templates

PDMS base with curing agent (Sylgard 184 silicone elastomer kit; #240 401 9862) was purchased from Dow Corning Corporation (Midland, MI, U.S.A). A di-block copolymer of PDMS-b-PEO (75:25), methyl terminated (#09780-100), from Polyscience Inc. (Warrington, PA, USA) was used to make PDMS hydrophilic. The speed mixer (#DAC 150SP/601 0064) and its plastic containers were purchased from FlackTek Inc. (Landrum, SC, USA).

The polymer mixture was prepared by mixing x mg PDMS-b-PEO, y mg of PDMS monomer and y/10 mg of curing agent such that (x/y) * 100=2.07 % PDMS-b-PEO relative to PDMS monomer. The contents of the container were mixed for 6 minutes at 3000 rpm. Then, a 20-60 mg glob of PDMS-PEO (grey) was dropped on an iridescent Si master (black) and also on a 2.5 x 1 inch's rectangular glass slide (light blue) that had two 1 x 1 inch's square glass mounts on its sides, as

schematically depicted in Figures 7a and 7b, respectively. The Si master was pre-rinsed with acetone and deionized (DI) water, and dried with air. The Si master with the glob was then inverted (Figure 7c) and placed on top of square mounts at a 45-degree angle (Figures 7d and 7e). The construct was then degassed in a vacuum chamber at 25-30 mm Hg and placed on a hot plate at 45°-150° C. Cured PDMS-PEO templates were stored in polystyrene plastic boxes. Typical thickness of PDMS-PEO stamps produced by this method are ca.300 μm.
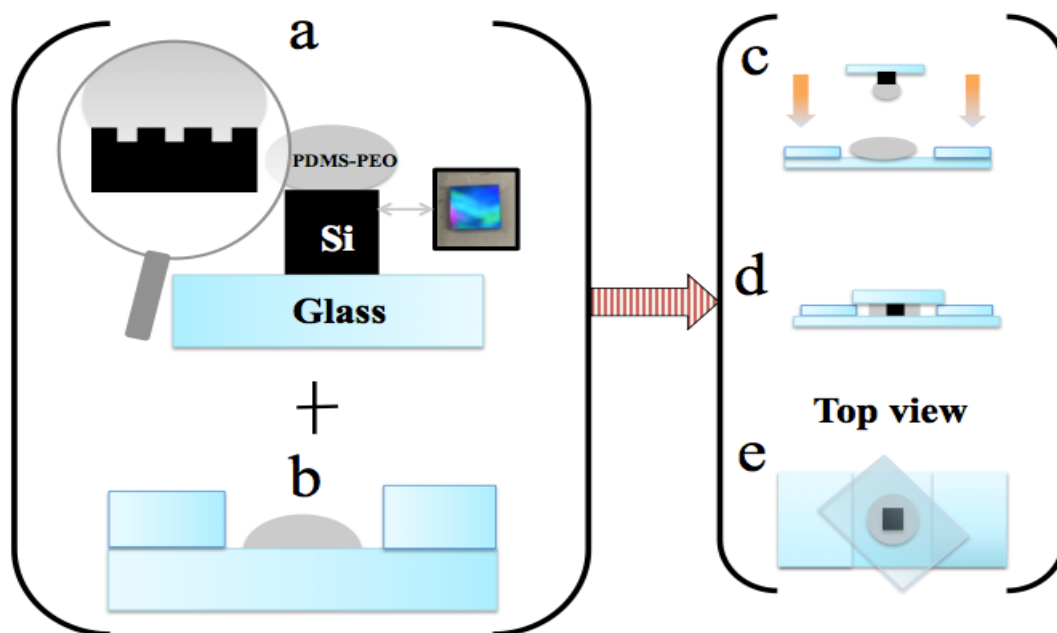
Figure 7. PDMS-PEO stamps: a) PDMS-PEO glob (grey) dropped on pre-treated Si stamp (black) placed on glass (blue), b) PDMS-PEO glob dropped on glass, c) Si stamp with PDMS-PEO glob face-down d) PDMS-PEO sandwiched between Si stamp and glass, and e) top view of the construct.

Table 3 enumerates the geometric configuration of PDMS-PEO templates negatively imprinted from Si master with posts.

Table 3. Lattice configurations.

Dimensions [nm]	Type 1	Type 2	Type 3
Lattice pitch	600	700	700
Cavity depth	150	150	350
Cavity diameter	195	260	260

Table 4 shows monolayer spatial confirmations of spherical NPs that can fit inside a PDMS-PEO cylindrical cavity (top view) based on the ratio of diameter of the cavity to diameter of the particle.[61]

Table 4. Commonly occurring spatial conformations of NP ensembles inside a cavity.

Ensemble Conformations (2D)	D/d
	1.00-2.00
	2.00-2.15
	2.15-2.41
	2.41-2.70
	2.70-3.00
	3.00-3.30

Two types of AuNPs were used in the current work: a) AuNPs with polyvinlypyrrolidone (PVP) shell that are stable due to steric stabilization in solutions, and b) citrate-stabilized AuNPs which

are stable due to electrostatic repulsions resulting from negatively charged citrate ions.[71] The citrate and PVP capping agents around NP surfaces are shown in Figure 8 schematically.
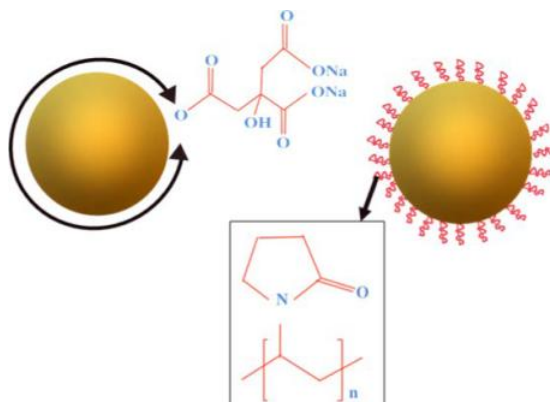
Figure 8. Citrate- (left) and PVP-stabilized (right) AuNPs.

2.2.3. Particle deposition *via* evaporative convection

Figure 9 schematically shows NPs (yellow) in a water drop on PDMS-PEO (grey), where the estimated contact angle was 47°. Additionally, the contact angle estimated for a water drop (dashed) on borosilicate cover slip (blue) was 61°. Due to evaporation (red arrows) of solvent at the interface, capillary forces drive particles at the center to the interface (indicated by green arrows). The contact line at the interface recedes continuously, thereby pinning the particles onto the substrate. Figure 9 represents a coffee-ring effect scenario. The NP assembly process is governed by surface energy of PDMS-PEO and cover slip, evaporation rate, AuNP concentration, volume of the drop/solution added, and pretreatment methods. Two approaches of template-assisted self-assembly were used in the present work. Both PDMS-PEO stamp and the glass/cover slip were immobile in these methods. Initial approach involved PDMS-PEO stamp with excess walls and a glass slab with 1/8th inch drilled hole. As shown in Case a (Figure 10), a 40 µL PVP-

AuNP (76 nm; 1.9e+9 NPs mg/mL) solution (pink) was pipetted through the glass (blue) hole into the PDMS-PEO receptacle (grey, Type 3 lattice, Table 3) with excess walls at the edges ($t_1 = 0$ s).
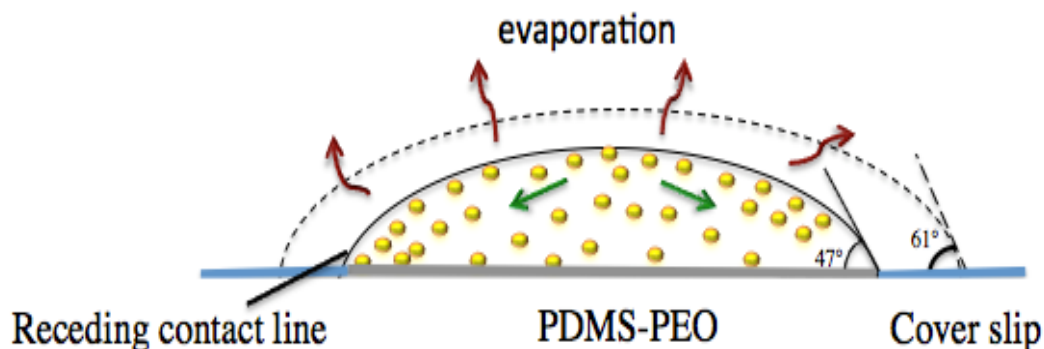
Figure 9. Evaporation-induced convection, and receding of contact line in a drop of water (AuNPs) on PDMS-PEO and cover slip (dashed) with corresponding contact angles of 47° and 61°, respectively.
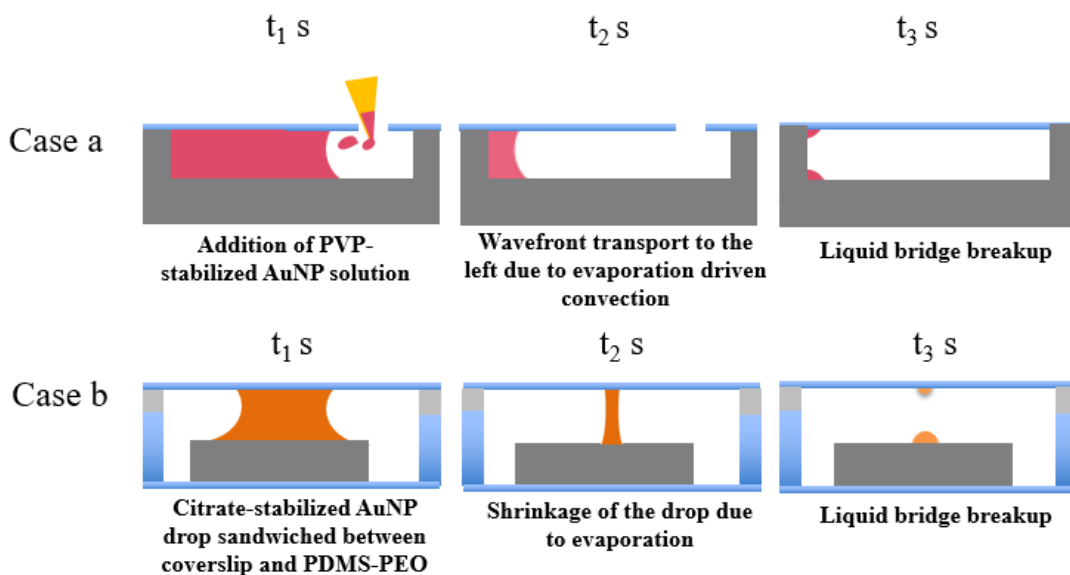
Figure 10. Template-assisted self-assembly: Case (a) t_1 s shows the addition of 40 μL PVP-stabilized AuNP solution onto PDMS-PEO with excess walls; t_2 s shows wavefront transport due to evaporation driven convection; t_3 s shows liquid bridge breakup into into satellite drops. Case (b) t_1 s shows addition of 1-2 μL citrate-stabilized AuNPs on PDMS-PEO; t_2 s shows shrinkage of the drop due to evaporation; t_3 s shows liquid bridge breakup upon prolonged evaporation.

Evaporation of solvent causes wavefront transport and supports contact line pinning of NPs in the cavities of PDMS-PEO template. Time, t_2 s, shows residual liquid with contact line receding, and solvent adherence to the PDMS-PEO edge on left. The liquid bridge breakup leads to formation of two satellite drops at t_3 s. Typical evaporation time in this process was 1.5-2 hr at 25°C and 18-22 % relative humidity. Due to conformal contact of glass with PDMS-PEO walls, solvent preferentially evaporated through the drilled hole in glass. The glass was washed with DI water, whereas PDMS-PEO (cured at 150°C) was soaked in DI water for 120 s and dried prior to self-assembly.

The second approach (Case b, Figure 10) involved a cage composed of cover slips (blue) with a wall height of 700 μm, and unsoaked PDMS-PEO (2 %) cured at 45 °C. At t_1 s, a 1-2 μL citrate-stabilized AuNP (100 nm) drop (6.86e+7 to 1.372e+8 NPs, orange, Nanopartz, CO, USA) was pipetted onto the unsoaked PDMS-PEO (grey), and in <30s, an untreated cover slip (150 μm) with vacuum grease (light grey) on edges for tight seal was placed over the walls of the cage to slow evaporation rate. Evaporation through the empty spaces between the cover slip and walls causes the surface area of the drop to shrink, as shown at t_2 s, and prolonged evaporation results in liquid bridge breakup into two satellite drops (t_3 s). Separation distances of 50-350 μm and evaporation times of 1-6 hr were obtained in this method based on stamp thicknesses of 300-500 μm, drop sizes of 1-2 microliter, pressed or un-pressed conditions of the cover slip, pre-treatment conditions of Si master (acetone + water rinse) and PDMS-PEO stamp (soaked versus unsoaked), concentration of PDMS-b-PEO (2%), lattice spacing (Type 1 or 2, Table 3), etc. These conditions for five samples labeled a-to-e are shown in Table 5. Untreated cover slips promoted AuNP deposition on PDMS-PEO compared to pre-treated cover slips in 23 % nitric acid. While a concentration of 6.86e+8

NPs in 1 µL resulted in excess aggregation over ordered areas, a concentration of 1.372+8 NPs in

2 µL drop resulted in dense ordering and relatively low aggregation.

Table 5. Experimental conditions and outcomes for five samples produced using Case b.

Sample	a	b	c	d	e
Separation distance (µm)	50-250	200-350	200-350	200-350	200-350
PEO (%)	2	2	2	2	2
Concentration in each iteration (NPs)	6.86E+08	6.86E+07	1.372E+08	1.372E+08	1.372E+08
Drop volume (µL)	1	1	2	2	2
Number of iterations	1	2	1	1	1
Water pre-treatment	none	none	none	none	none
Si pre-treatment	acetone + water rinse	acetone + water rinse (3x)	acetone + water rinse (3x)	acetone + water rinse (3x)	acetone + water rinse (3x)
Lattice spacing (nm)	700	700	700	600	600
Cover slip	pressed	pressed	unpressed	unpressed	unpressed
Evaporation time (min)	200	360	120	180	180

2.3. Summary

Traditional top-down methods for producing 2-D arrays were summarized. Bottom-up method

known as template-assisted self-assembly has been used in this work to produce 2-D arrays, as it

is an economically viable option. Enhancement of PDMS surface energy using a PDMS-b-PEO

block copolymer has been described in tandem with soft-lithography for fabrication of iridescent

PDMS-PEO templates. Finally, evaporation-driven convective self-assembly of particles in the

nanoimprinted cavities of PDMS-PEO at various conditions was demonstrated. Costs associated

with PDMS monomer base, curing agent, block copolymer for modification of PDMS surface

energy, pre-lithographed Si masters for nanoimprinting PDMS-PEO stamp, and gold nanoparticle

suspension accrued to be <$750 in the present work. Chapter 3 will discuss about characterization

of optical resonances from metamaterial arrays using an empirical, mesoscopic approach and *in

silico* methods.

3.   ALL-OPTICAL CHARACTERIZATION OF 2-D ARRAYS

This chapter discusses all-optical, mesoscopic characterization of AuNP population in PDMS-PEO lattices at differential fields-of-illumination (FOIs), correlation of optical properties of lattices with population of AuNPs, and comparison of empirically measured results with simulations based on Mie theory and coupled dipole models. A 2-D plasmonic lattice could be imagined as a network of NP sites that can receive and transmit optical signals similar to 'coupled dynamic nodes' in 'synchronization networks', where coherent features emerge based on coherent interactions between nodes.[72] Therefore, nanoimprinted cavities populated with AuNP(s) described herein are referred to as "optically active nodes" recognizing their contributions to the overall emergence of coherent diffractive coupling (CLR) in addition to lattice plasmon features (LPR). A 'chain' in the present work is referred to as a one-dimensional (1-D) chain of a certain number of continuous active nodes. Chains of differing sizes may be present based on how sparse the particles were distributed in the lattice.

3.1. Episcopic and diascopic illumination

Episcopic (reflection) and diascopic (transmission) illumination modes of a light microscope (Eclipse LV100 D-U, Nikon Instruments, Melville, NY, USA) connected to a spectrometer (Shamrock 303, Andor Technology, Belfast, UK) were used in the present work. Particularly, the following objectives of the microscope were used: 20x, 50x, and 100x. Lowest aperture size was 200 μm in diascopic mode and 60 μm in episcopic mode.

Figure 11 illustrates the mechanism of episcopic (left) and diascopic (right) modes. In episcopic illumination, light rays coming from a halogen lamp above (orange), hit the sample and reflect back (yellow) into a beam splitter *via* the objective. Beam splitter splits 50 % of the light to lumenera camera and the rest to a spectrum analyzer. In diascopic mode, light rays coming from a

halogen lamp from beneath (orange) are focused onto the sample *via* condenser lens. Beam splitter then collects the transmitted light *via* the objective and sends half of it to the camera and the other half to the spectrum analyzer. Dark field (DF) microscopy was used predominantly to capture images for high contrast, while bright field (BF) microscopy was used to capture spectral extinctions (AU). Spectra were captured by illuminating the FOI with linearly polarized light in x-direction.

a) light source; b) beam splitter; c) spectrum analyzer; d) camera
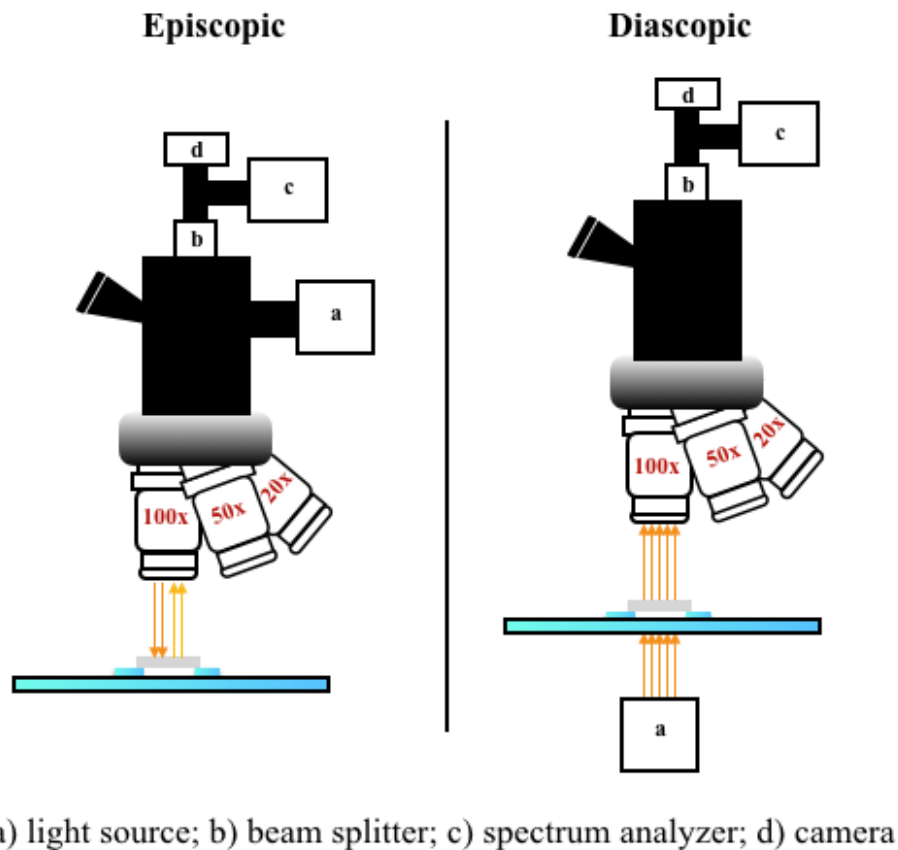
Figure 11. Mechanism of episcopic (left) and diascopic (right) modes of an optical microscope.

3.2. Mesoscopic analysis of optically active nodes in PDMS-PEO lattices

This work primarily focused on mesoscopic analysis since PDMS-PEO is an insulator and not conducive to imaging using scanning electron microscopy (SEM) at high vacuum, owing to

25

charging effects. Attempts of coating a conductive layer on PDMS-PEO surface were not tried to preclude any consequences pertaining to unforeseen changes in optical and thermal behavior. However, SEM characterization of AuNPs transferred to a glass surface from PDMS-PEO lattice will be discussed in a later section.

3.2.1. Trichromatic color model

As explained by Young-Helmholtz theory, a human eye contains three kinds of cone cells. These cone cells absorb long (L, 564-580 nm), medium (M, 535-545 nm) and short (S, 420- 440 nm) wavelengths of light. A coherent interaction between these signals reaching the brain through the optic nerve is interpreted as color in humans.[73] Figure 12 shows the schematic of a human eye with constituent elements, and LMS cone cells.
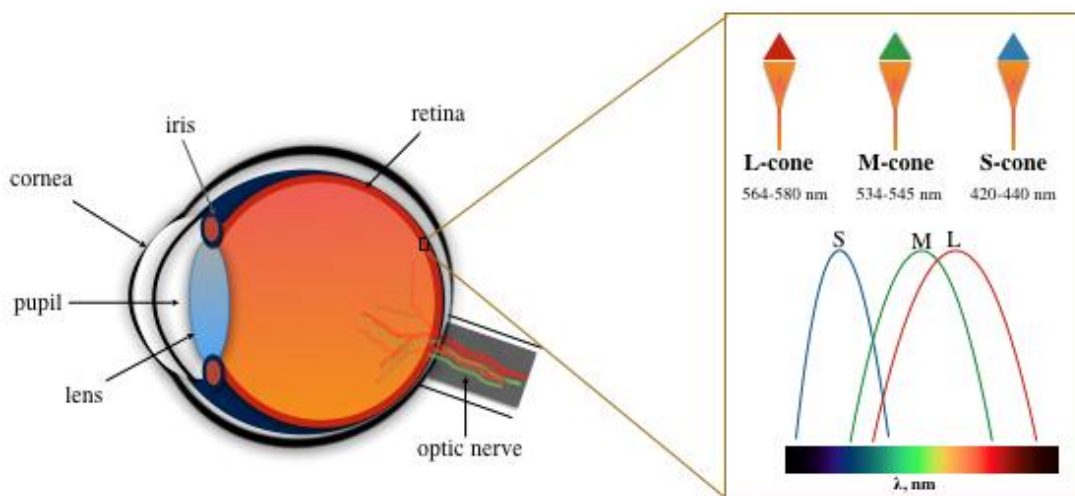
Figure 12. Illustration of Young-Helmholtz theory, and the trichromacy principle of human vision (LMS cones).

A color space model known as red, green and blue (RGB) was developed based on the trichromacy principle of human vision (LMS space). The RGB model is additive in nature, e.g., red, blue and green colors can be added in assorted proportions to reproduce a broad array of colors.[74] Electronic

devices generally save images in the form of non-linear RGB values, for optimization of memory bits, which are calculated by multiplying a non-linear transfer function to linear RGB values captured from an object. The non-linear color space is usually denoted by R'G'B'. Each pixel of an image is composed of a R'G'B' triplet. The values of the triplet combine in varying proportions to produce various colors. These R'G'B' values are correlated using the following Equation:

$$Y' = 0.299R' + 0.587\,G' + 0.114B' \tag{3.1}$$

where Y' is called as luma or photometric luminance of an image. It could have integer values between 0 and 255. Equation 3.1 was recommended by International Telecommunication Union (ITU) in 1982 for encoding analog signals in digital form.[75]

Trichromatic models are of growing interest for chemical sensing and differentiation of chemical samples with small spectral variations.[76,77] A recent work utilized trichromatic color space for SPR sensing in Fano resonant aluminium clusters.[78] The present work exploited photometric properties of AuNPs in microscope images for counting number of optically active nodes.

3.2.2. Manual tracking of optically active nodes

Image analysis packages available in MATLAB or ImageJ provide built-in plugins for particle counting by isolating particles with respect to the background *via* thresholding, converting the image to grayscale/binary form, changing brightness, deconvolution, filtering, etc. Dark field (DF) images captured in the current work contain NP sites ranging from 143 (100x objective) to 13223 (50x objective) active nodes that would render conventional automated particle counting difficult to implement due to problems associated with image contrast and isolating active nodes from inactive nodes. Therefore, initial approach for counting particles was based on a manual counting procedure using 'cell counter' plugin of ImageJ.[79] The plugin tracks the number of nodes that are

marked in real-time, as shown in Figure 13a for an image containing 1363 active nodes in the array

captured using 100x objective.
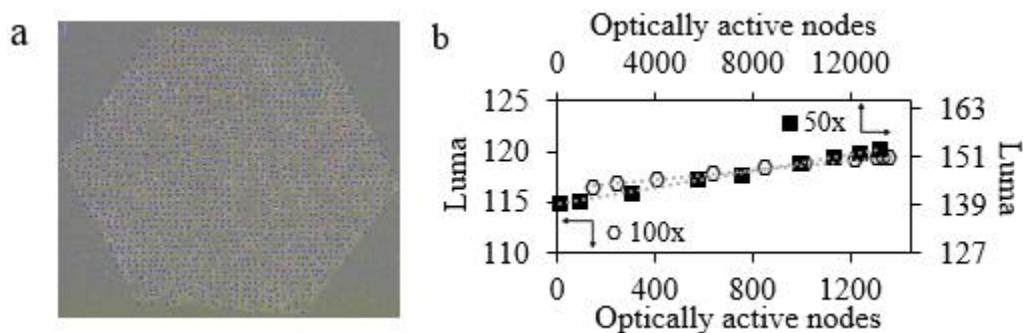
Figure 13. Field-of-view (FOV) image analysis: a) active nodes marked using cell counter plugin, b) linear dependence of luma and active nodes for images captured in episcopic (hexagons) and diascopic (filled black squares) modes.

An average of two manual counts was taken for images captured using 100x and 50x objectives.

The images captured by 50x objective have a rectangular FOI compared to hexagonal shape of

100x images. Hence, the data points representing 100x images are hexagonal, and 50x are

rectangular, respectively, as will be seen in all subsequent Figures. Figure 13b shows a linear

relation between the number of optically active nodes measured in episcopic (100x, hexagons) and

diascopic (50x, filled black squares) images and luma. This linear relation is taken as the basis for

developing an *ad hoc* subroutine for statistical analysis of active nodes in 2-D lattices.

3.2.3. Sequestration of 1-D chains from 2-D lattices

The MATLAB subroutine for counting active nodes and generating distribution of 1-D chains of

active nodes works as follows. A DF image captured by either 50x or 100x is first imported into

MATLAB. Each node in a standard 50x image (1920 x 2560 pixels) has dimensions in decimals,

but MATLAB works with whole numbers. Hence, each image will be resized to 1908 x 2556

pixels resulting in a unit node size of 18 x 18 pixels. Similarly, a 100x DF image (Figure 14a) will be resized to 1904 x 2516 pixels resulting in a unit node of 34 x 34 pixels. After resizing, luma for each pixel will be calculated using Equation 3.1, based on R'G'B' triplets at each pixel, as illustrated in Figures 14b and 14c.
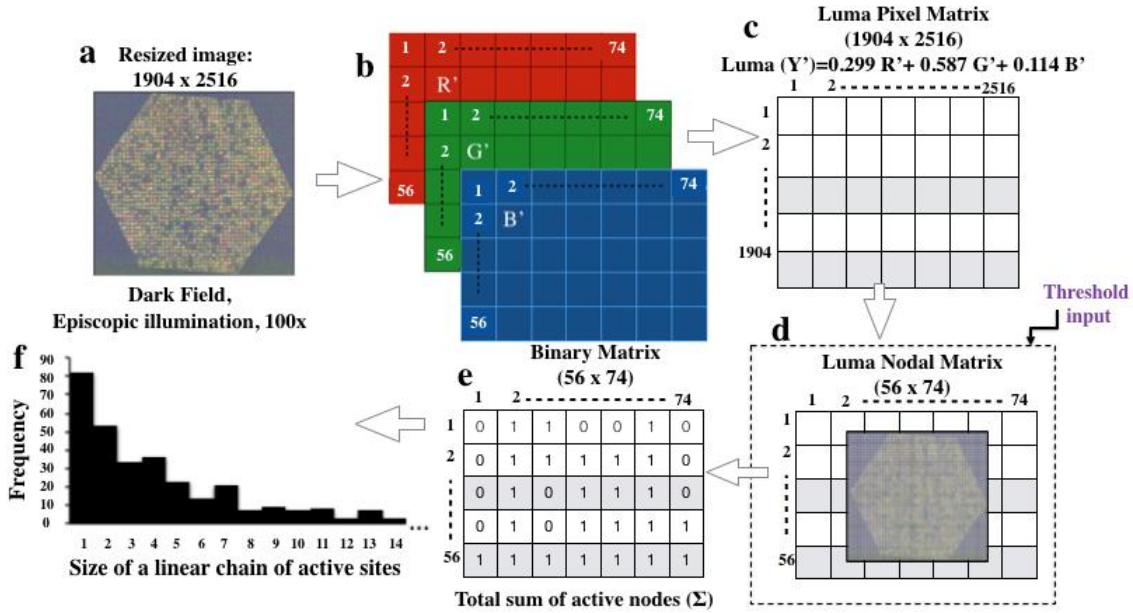
Figure 14. Working mechanism of the MATLAB subroutine: a) resized episcopic (100x) image, b) extraction of R'G'B' values for all pixels, c) luma pixel matrix generation, d) luma nodal matrix generation, e) binary matrix generation, summation of total active nodes, and sequestration of 1-D chains of varying sizes, and f) output containing distribution of 1-D chain sizes of continuous active nodes.

The luma values of a group of pixels corresponding to a unit node will be further averaged to produce a luma matrix corresponding to the nodal array (56 x 74 nodes), where demarcation of each node occurs, Figure 14 d. This luma matrix is transformed into a binary matrix of zeros and ones based a threshold value inserted as input to the subroutine (Figure 14e). Zero denotes an empty node and one denotes an active node. The subroutine sums all ones to give the count of active nodes in tandem with the distribution of varying 1-D chain sizes of continuous active nodes. For example, chain sizes with two active nodes was attributed a frequency of ca.50, i.e. there are

50 1-D chains with two active nodes in a sample containing 1363 total active nodes. This way, 2-D arrays were sequestered into 1-D chains for statistical analysis, especially in episcopic mode for detecting the minimum requirement of lattice ordering for producing a coupled resonance.

3.3. Detection of LPR and CLR resonances at differential fields-of-illumination (FOIs)

Three FOIs (60 μm, 200 μm, and ca.2000 μm) or aperture sizes were used in the present work for analyzing the spectra (images) from PDMS-PEO lattices whose nanoimprinted cavities were populated with AuNPs, as outlined in Chapter 2, utilizing evaporation-induced convective assembly (2.2.3 Particle deposition *via* evaporative convection). Sparse PDMS-PEO lattices (Type 3, Table 3) produced using the method delineated in Case a were analyzed using 60 μm and 200 μm apertures (short-range).[80] A ca.2000 μm aperture (long-range) was used for analyzing densely ordered lattices (Types 1 and 2, Table 3) spanning an area up to ca.3 x 3 mm of ordering, produced using the methods outlined in Case b.

3.3.1. Short-range illumination

3.3.1.1.   Episcopic illumination: 60 μm FOI

Figure 15a shows that the intensity (counts) of LPR at 540-560 nm increased in magnitude and blue-shifted, while CLR at 720-740 nm increased in magnitude and red-shifted as the number of optically active nodes in the hexagonal FOI increased. [80]
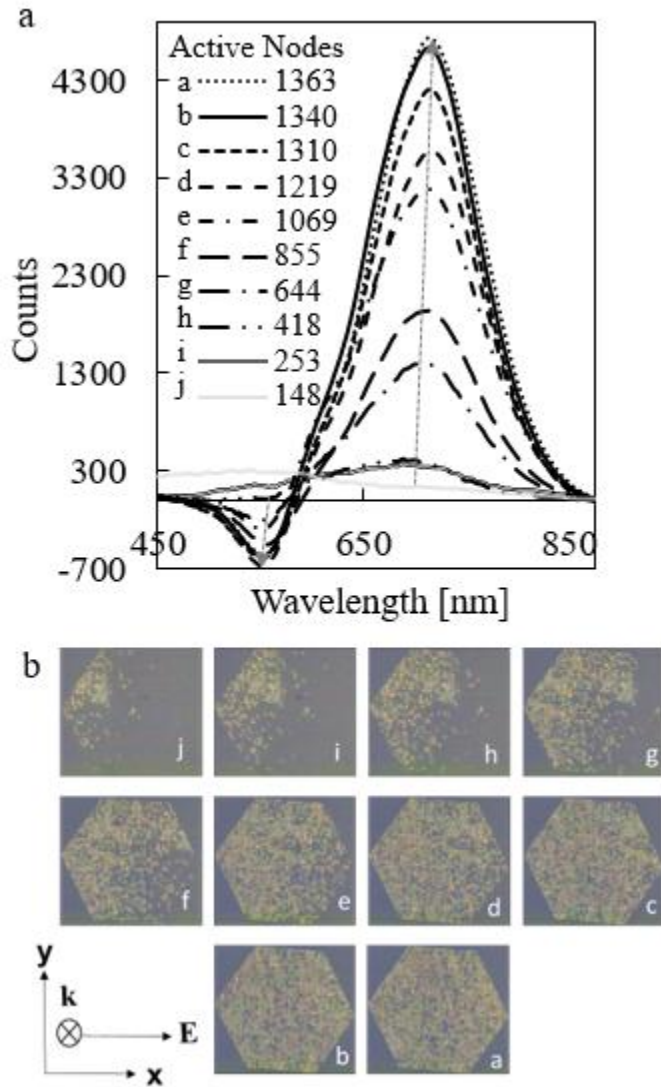
Figure 15. a) LPR (maxima at 540-560 nm) and CLR (maxima at 720-740 nm) magnitudes increased with increasing number of active nodes in the FOI (148 to 1363). Spectra (counts) were obtained at 100x magnification in episcopic illumination; b) Series of corresponding DF images (a to j) of the lattice.

The corresponding episcopic images captured using 100x objective are shown in Figure 15b where

Image (a) has the highest number of active nodes (1363), and Image (j) has the least count (148).

The successive series of images were captured horizontally by linear translation of the microscope

stage, where six columns of nodes separated each image. Negative counts of LPR signal was

obtained due to light being absorbed or scattered in-plane and not reflected back compared to a

31

bare PDMS-PEO reference. As CLR signal was an artifact of diffractive coupling, it showed positive counts.

Furthermore, statistical image analysis was conducted by considering 100x images to detect the least number of chain sizes, which contribute to the emergence of a CLR feature. Figure 16 shows the increase in chain sizes as the total population of active nodes in the image increased, i.e., homogeneity increased, or sparsity decreased
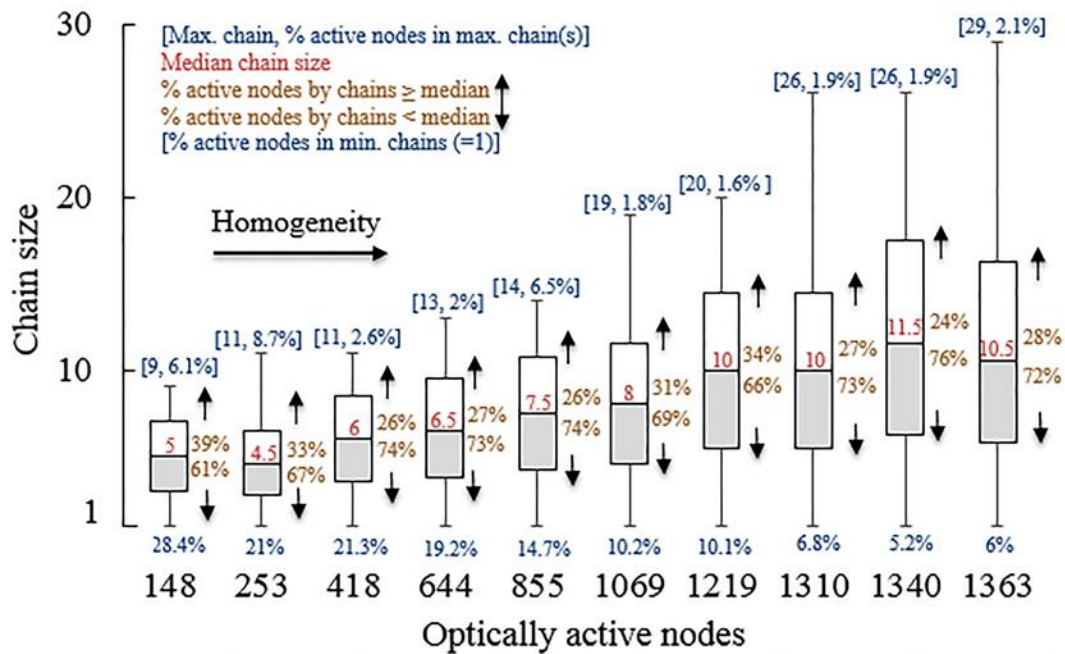
Figure 16. Distribution of chain sizes for sample areas captured with 100x containing active nodes in the range 148-1363.

Histograms generated for showing the frequency distribution of chain sizes in an array (Figure 14f) were combined and plotted in the box-and-whisker plot of Figure 16. Interesting trends that can be observed are, increase of homogeneity is accompanied by increase in maximum chain size (top whisker, blue text), increase in range (maximum chain size-minimum chain size), and increase in median chain size (red font). Figures 17a and 17b show that chain sizes containing as few as

five active nodes on average led to the emergence of a CLR peak (enclosed in solid rectangular box) even prior the emergence of LPR peak (dashed box).
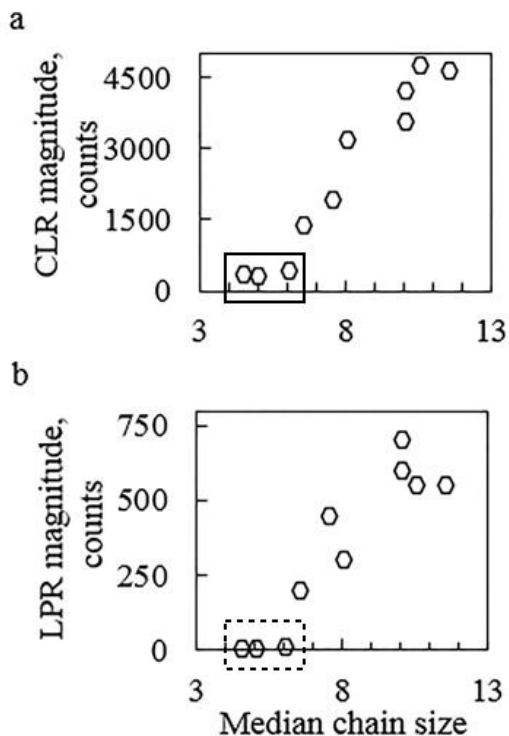
Figure 17. a) CLR and b) LPR features are plotted with the median chain size for each image captured in episcopic mode, 100x (hexagons). Increasing particle median chain size gave rise to higher intensities for both LPR and CLR features.

3.3.1.2.   Diascopic illumination: 200 μm FOI

Figure 18a shows that the extinction magnitude (AU) of LPR at 540-560 nm increased and blue-shifted, while that of CLR at 720-740 nm increased and red-shifted, as the number of optically active nodes in the hexagonal FOI increased.[80,81]
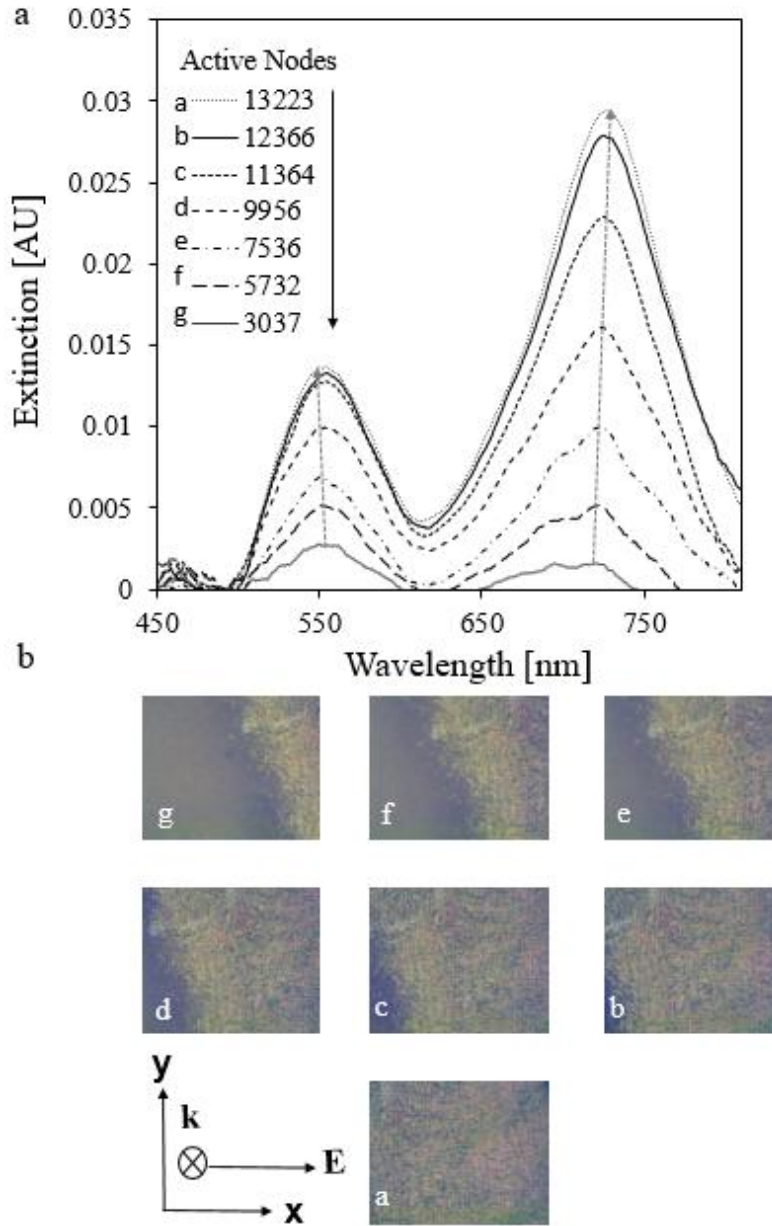
Figure 18. a) LPR (maxima at 540-560 nm) and CLR (maxima at 720-740 nm) magnitudes increased with increasing number of active nodes in the FOI (148 to 1363). Spectra (AU) were obtained at 50x magnification in episcopic illumination; b) Series of corresponding DF Images (a) to (g) of the lattice.

The corresponding diascopic images captured using 50x objective are shown in Figure 18b, where

Image (a) has the highest number of active nodes (13223), and Image (g) has the least count (148).

34

The successive series of images were captured horizontally by linear translation of the microscope stage, where 20-40 columns of nodes separated each image.

It is important to note that a 50x image accounted for only 18% of the number of total nodes present in the spectral FOI in diascopic mode, yet similar increases and energy shifts in LPR and CLR signals persisted as seen in episcopic mode.

3.3.2. Long-range illumination: ca.2000 μm FOI

Samples numbered a-to-e, produced using the method outlined in Case b are shown in Figure 19a. The conditions of self-assembly for each sample were listed in Table 5.
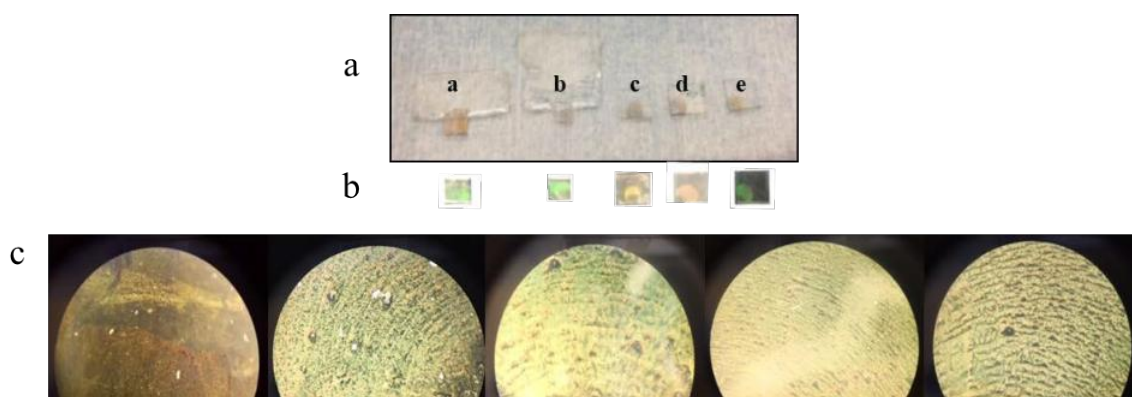
Figure 19. Long-range illumination: a) Samples a-e with ca.2 x 2 mm to ca.3 x 3 mm areas of ordering, b) iridescence observed commonly on samples, and c) glimpse of 20x FOIs as observed through the eyepiece.

The brownish hue on samples corresponds to the areas of ordering (ca.2 x 2 mm to ca.3 x 3 mm). Figure 19b shows iridescent behavior of lattices under illumination by light. Figure 19c shows a glimpse of 20x FOVs of the samples as observed through the eyepiece of the optical microscope (DF). Optically active nodes could exhibit different colors based on the number of AuNPs present inside each cavity (Table 4). The optical responses of these arrays (captured using a white light

35

source illumination set-up) will be discussed in tandem with thermal responses in the subsequent chapter.

3.4. Comparisons of optical behavior of 2-D arrays characterized empirically, with theoretical simulations

This section mainly emphasizes the role of population of active nodes on the strength of LPR and CLR signals. For the sake of simplicity, each active node in simulations is considered to contain one AuNP. However, more than one AuNP was deposited in the cavities of nanoimprinted PDMS-PEO cavities. Figures 20a and 20b with 2 μm and 1μm scale bars as insets, respectively, show SEM images of AuNPs from PDMS-PEO cavities (Type 3 lattice, Table 3) transferred to a positively charged glass.[80]
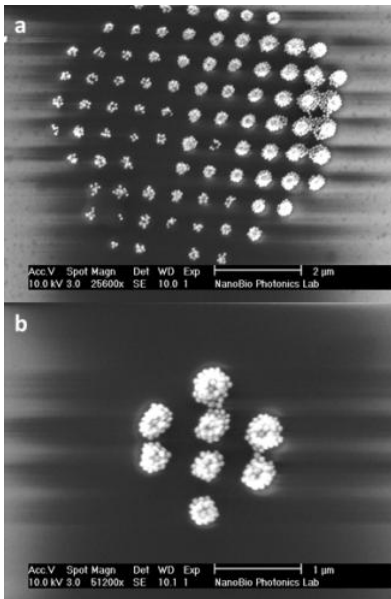
Figure 20. SEM images of AuNPs transferred to glass: a) 2 μm, b) 1 μm.

3.4.1. Single AuNP (Mie theory) versus AuNP array (present work)

Gustov Mie in 1908 published results concerning the interaction of light with sub-wavelength particles, and particles that had dimensions equal to wavelength of light.[82] He solved the solution to Maxwell's equations for the scattering of light from spherical particles. This path-breaking paper also augmented our understanding on polarization effects, and color of gold colloids. Mie theory defines the absorption, scattering and extinction cross sections (σ_x) for a sphere as follows:[83]

$$\sigma_x = \pi a^2 Q_x \tag{3.2}$$

where a is the radius of the sphere, Q is the efficiency, and the subscript x represents absorption, scattering or extinction. Scattering efficiency is written as:

$$Q_{scat} = \frac{2}{q^2} \sum_{\alpha=1}^{\infty} (2\alpha + 1)[|a_\alpha|^2 + |b_\alpha|^2] \tag{3.3}$$

where α denotes the frequency-dependent proportionality constant known as polarizability, and a_α, and b_α denote the electric and magnetic amplitudes respectively. These amplitudes are a function of dielectric permittivity ε, magnetic permeability μ, and a shape parameter which is shown in Equation 3.4:

$$q = \frac{\omega a}{c} \tag{3.4}$$

Here, ω is the frequency of incident light while c is the speed of light in vacuum. The scattering amplitudes are given as:

$$a_\alpha = \frac{\mathfrak{R}_\alpha^{(a)}}{\mathfrak{R}_\alpha^{(a)} + i\mathfrak{J}_\alpha^{(a)}}, b_\alpha = \frac{\mathfrak{R}_\alpha^{(b)}}{\mathfrak{R}_\alpha^{(b)} + i\mathfrak{J}_\alpha^{(b)}} \tag{3.5}$$

where $\mathfrak{R}$ and $\mathfrak{J}$ are spherical Bessel and Neumann Functions, respectively. Particularly, in random NP systems, the net exchange of signals between the particles or coupling is zero where Mie theory

provides excellent agreement with empirical data. The plasmon feature tends to blue-shift when particles are ordered into an array compared to a single particle as shown in Figure 21. Extinction cross section (cm^2) calculated using Mie theory for a single NP is compared to the extinction spectrum corresponding to a 50x image containing 13223 active nodes. The parameters used were particle size = 76 nm, medium refractive index = ca.1.45, PVP shell size = ca.10 nm, and PVP refractive index = ca.1.52).[84]
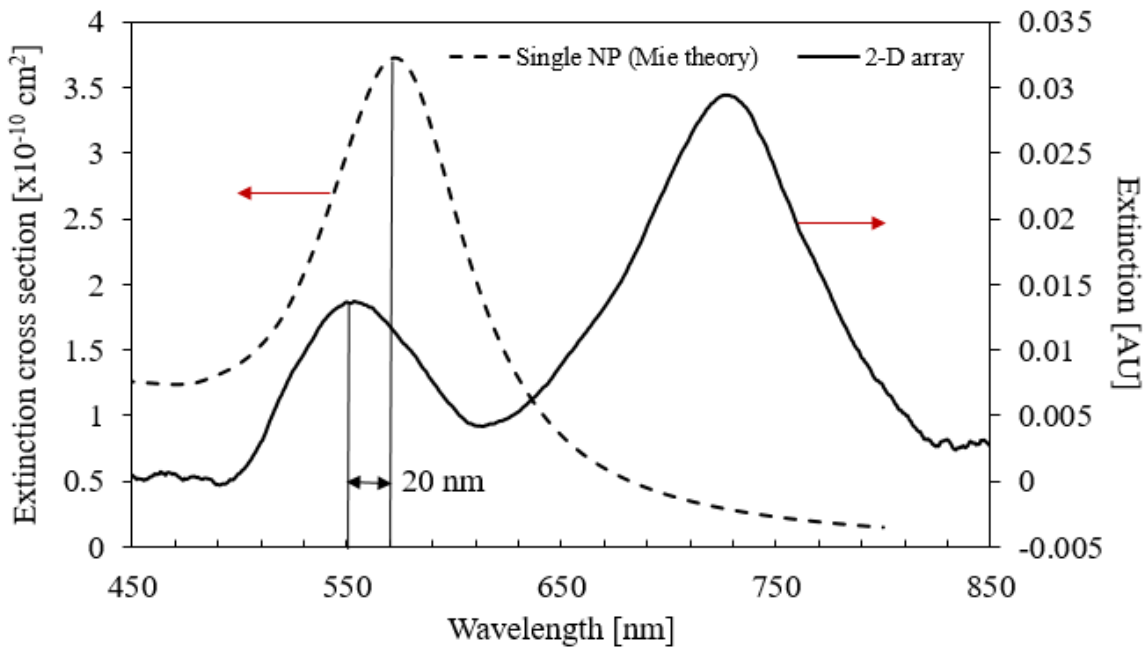
Figure 21. Comparison of extinction in absorbance units of a 2-D array (13223 active nodes) with Mie theory result for a single NP in extinction cross section (cm^2).

Coupled dipole approximation (CDA) to Maxwell's equations where electromagnetic field is considered as a collection of dipoles, on the other hand, could predict the behavior of resonances in 2-D arrays more accurately, which involves the interactions between particles.

3.4.2. CDA versus experimental results

In a CDA model, a square array of polarizable objects is considered to have smaller dimensions compared to incident wavelength of light where induced electromagnetic field can be approximated as dipolar. Each NP is considered as a point dipole with positive charge positioned at the origin and the negative charge oscillating around the axis of polarization. Electromagnetic fields surrounding each NP are then a combination of incident field and the scattered field from adjacent NPs. The overall polarization (P) as a function of local electromagnetic field is then expressed as:[85]

$$P = \frac{\alpha E_{inc}}{1 - \alpha S} \tag{3.6}$$

where E_{inc} represents the incident field, and S denotes the retarded dipole sum that considers far- and near-field dipole interactions from neighboring particles. For example, at lattice spacing close to the wavelength of light, far-field lattice diffraction is predominant in S. The optical extinction of the lattice excited by an orthogonally incident light of wavevector, k, is expressed as:

$$\sigma_{ext} = 4\pi k \, \Im \left(\frac{1}{1/\alpha - S} \right) \tag{3.7}$$

Recent work by DeJarnette *et al.* led to a rapid, semi-analytical solution (rsa) for CDA. The rsa-CDA model decreases the computational expense for 2-D arrays of spherical NPs, as it allows a double summation to calculate effects of off-diagonal and off-axial elements in the array. This decreases the number of function calls needed to calculate the retarded dipole sum while maintaining accuracy. [28,39,86]

Figure 22 shows a CDA simulation (ordinate is in extinction efficiency which is the ratio of extinction cross section and geometric cross section or area of the particle) for arrays of increasing sizes (5x5 to 30x30).[80] Note that the LPR blue-shifts; increases in magnitude, and CLR red-shifts;

increases in magnitude as the number of AuNPs increase. This is consistent with the trends observed in experiments. The results from Mie theory and CDA overall agree with experimental behavior of LPR and CLR features. These trends could be related back to the classical analogy theory discussed in Chapter 1 (Section 1.2.2).
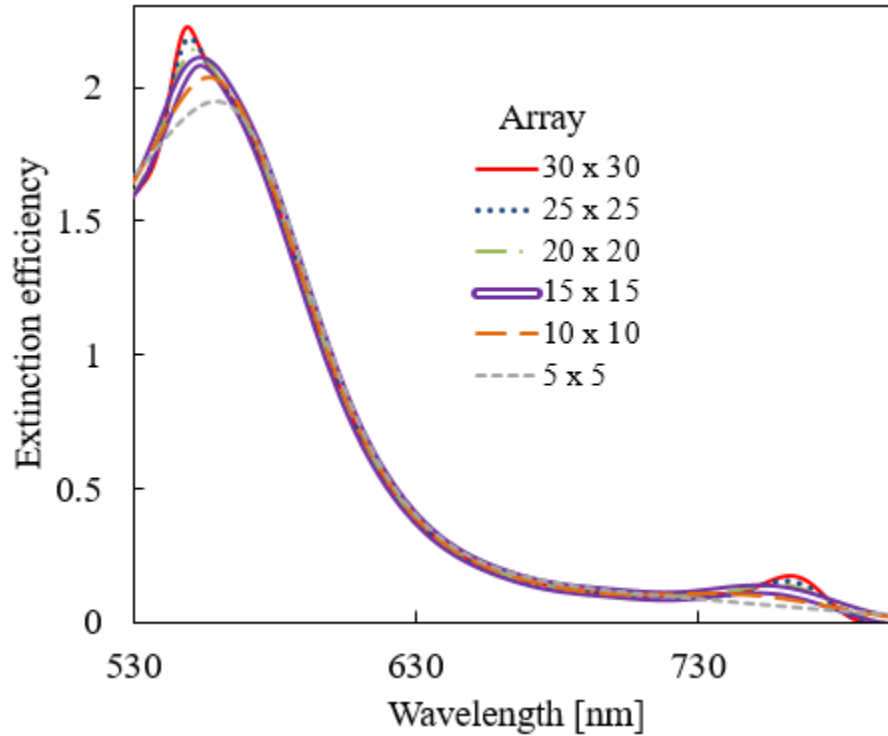
Figure 22. CDA simulation of arrays with increasing sizes (5x5 to 30x30).

Foremost, the presence of grating induces coupling between broadband LPR and narrowband diffractive modes, which blue-shifts the LPR feature, as evident in Figure 21, relative to a single NP. Now, as the array size increases, the coupling parameter increases causing further shifts in the coupled eigenmodes of LPR and CLR features (see Equations 1.3 to 1.6). In this case, CLR red-shifts and LPR blue-shifts as the coupling parameter increases by populating the array with more number of optically active nodes.

Classical analogy[43] also explains the concept of zero-frequency associated with the formation of an asymmetric lineshape where oscillator ω_1 will be driven out of phase with particle ω_2. In the present work, the same phenomenon tends to occur due to destructive interfere (180° phase change) of plasmons with in-plane diffracted light, owing to the grating. Consequently, a dip in the spectra can be noticed. This dip would ideally occur at the lattice spacing or grating constant. But in the presence of damping mechanisms, this dip would shift in wavelength (see Equation 1.6).

Finally, the results of rsa-CDA for arrays extending up to 301 x 301 matrix with ca.100000 active nodes (1 AuNP per node), and simulations of 1-D chains of silver (Ag) NPs evaluated using T-matrix and CDA by Zou et al.[87] (hollow circles) are compared to empirical CLR trends (filled black triangles, Figure 23) of 2-D arrays measured episcopically (hexagons) and diascopically (filled black squares).
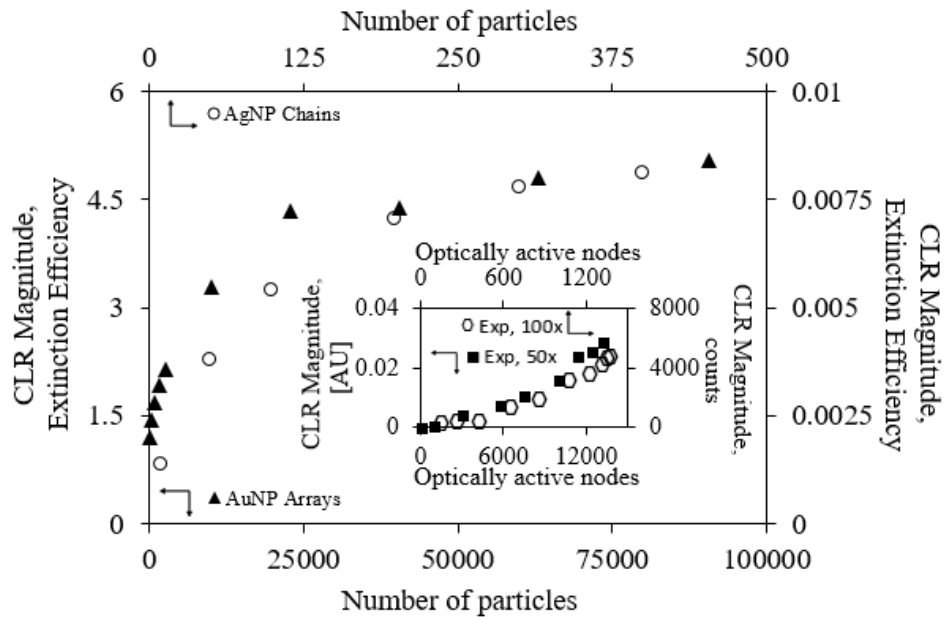
Figure 23. Experimental versus simulations: a) rsa-CDA for AuNP arrays (present work, filled black triangles), b) CDA and T-matrix for AgNP 1-D chains simulated by Zou et al.[87] (hollow circles). The inset shows a power-law dependence between active nodes and CLR magnitudes from episcopic (100x, hexagons) and diascopic (50x, filled squares) images.

While a logarithmic increase in the magnitude of extinction efficiencies with increase in population of active nodes was observed in simulations, a power-law increase of CLR magnitudes in AU with increase in active nodes was observed for 2-D arrays (inset, Figure 23). This trend persisted in both episcopic and diascopic modes. The dichotomy between experimental and theoretical trends may be caused due to the assumption of one NP per node in simulations.

The corresponding LPR peaks of 2-D arrays measured episcopically (100x, hexagons, counts) and diascopically (50x, filled black squares, AU) showed linear increases in magnitudes with increase in the population of active nodes, as shown in Figures 24a and 24b. The non-linear increase of CLR peaks with increase in nodal population is an interesting topic to consider for future research.
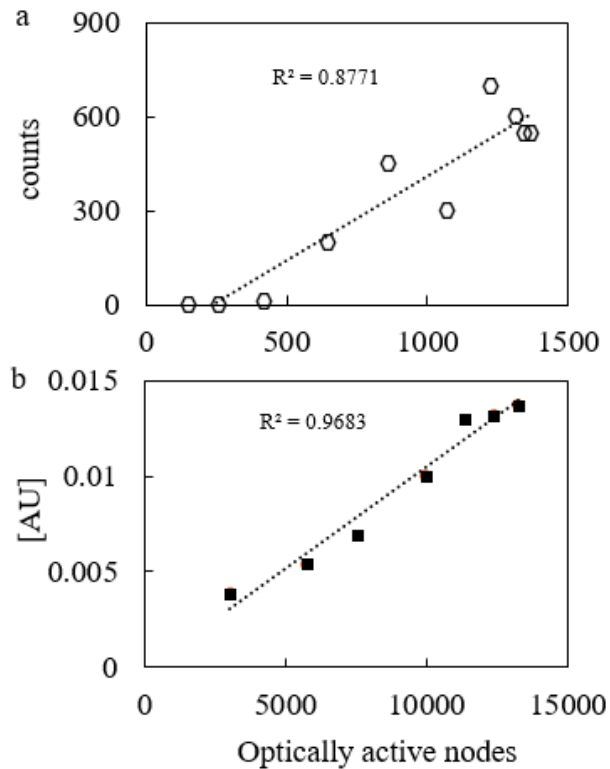
Figure 24. LPR increased linearly with increase in optically active nodes for a) episcopic (100x, hexagons), and b) diascopic images (50x, filled black squares).

42

3.5. Summary

Episcopic and diasopic illumination modes of an optical microscope (FOI: 60 μm; 200 μm) were used in the present work for capturing images/spectra at differential apertures or FOIs. Correlation of LPR and CLR resonances with optically active nodes in microscope images (FOI: 60 μm; 200 μm) was achieved *via* manual tracking of active nodes using ImageJ, and then isolation of 1-D linear chains into 2-D arrays in MATLAB using a subroutine based on the linear dependence of luma (array brightness) with the number of active nodes. The LPR blue-shifted and increased in magnitude while the CLR red-shifted and increased in magnitude with an increase in number of active nodes in the FOI. These energy shifts and increase in magnitudes conform to the blueprints of the classical analogy of Fano resonance. Statistical analysis revealed that a chain size of five on average led to the emergence of a CLR peak under 60 μm aperture in episcopic mode even prior to an LPR feature. Each active node represents a cavity with ≥ 1 AuNP (as suggested by SEM images of AuNPs transferred to glass). Empirical peak magnitudes at LPR and CLR maximas were cf. results of a single AuNP in Mie theory, and coupled dipole models for 2-D arrays (one NP per node). The energy shifts in LPR and CLR resonances in relation to increase in active nodes was corroborated by Mie theory and coupled dipole models. Overall, the CLR peak magnitude followed a power-law relation (in contrast to a logarithmic increase predicted by CDA), whereas the LPR magnitude increased linearly with increase in number of active nodes. The succeeding chapter deals with the optothermal characterization of arrays and comparison of empirical measurements with COMSOL results.

4. OPTO-THERMAL CHARACTERIZATION OF 2-D ARRAYS

This chapter will discuss the results of experimentally measured thermal responses from 2-D arrays at LPR, CLR and valley (dip) monochromatic wavelengths (λ_{LPR}; λ_{CLR}; λ_{valley}) obtained using a white-light source illumination set-up (Figure 25). These results will be correlated with the strength of LPR and CLR optical signals. The second part of this chapter will focus on finite element analysis (COMSOL) developed for simulating transient heat transfer in the system. Well-established models to date such as transient conduction in a finite slab (2-D), and convection from a vertical plate suspended in fluid (2-D) were first mimicked in COMSOL followed by their consortium into 3-D model in tandem with the addition of a radiation component. Finally, experimental thermal responses will be compared to COMSOL simulations.
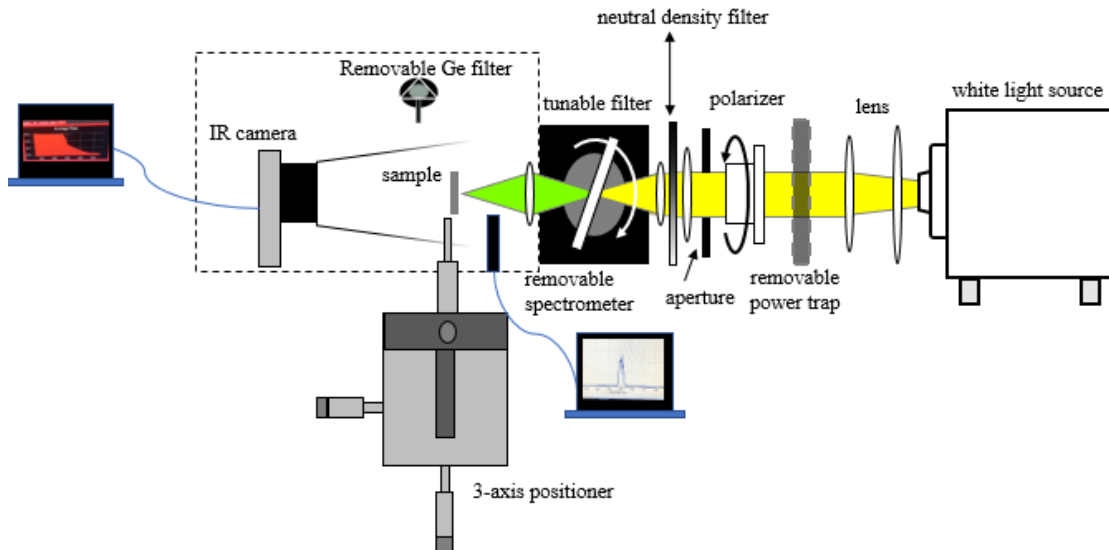
Figure 25. White light source set-up comprising of a white light source, lens, removable power trap, polarizer, neutral density filter, tunable filter, sample held by a 3-axis positioner and IR camera for irradiating 2-D arrays at λ_{LPR}, λ_{valley} and λ_{CLR}.

4.1. Experimental measurements of optothermal responses of 2-D arrays at λ_{LPR}, λ_{valley}, and

λ_{CLR}

Prior to thermal measurements, spectra of samples a-to-e fabricated using the self-assembly method delineated in Case b (Figure 10) were measured using a spectrometer (Avantes) annexed to the white-light source (HPLS-30-04, Thor Labs, USA) that has a visible light (400-750 nm) output of 10.2 W. The beam size was ~2.17 mm (ca. 2000 FOI). Only samples which showed distinguishable LPR and CLR peaks at these apertures were used for the thermal trials. Although samples produced by the method outlined in Case a also showed optical signatures, LPR and CLR features slightly overlapped which was not conducive for knowing their respective pristine thermal contributions. Also, deposition areas that were at least 2 mm x 2 mm gave rise to an optical response, on average, containing both LPR and CLR features.

The working mechanism of the white light source illumination set-up is illustrated as follows. The power source (far right in Figure 25) was initially warmed for 20 minutes, and then a turn knob was rotated to reach the lowest intensity. A 545 nm λ_{LPR} at this intensity gave an incident power of 5-7 mW. A USB thermal IR camera (far left, Schematic 12) purchased from Infrared Cameras Inc. (ICI-7320, P-series, TX, USA) plugged to a computer was placed in the path of the light source. The IR camera has a FOV of 36° and a focal plane array (microbolometer detector) that can sense long-range IR radiation (7000-14000 nm) from samples between -20°C to 50°C with an accuracy of ±1°C. The camera lens was sputtered with germanium to block light in the UV-visible to near-IR range. The software associated with IR camera that is installed in the computer allows taking the zero-point focal reference for camera when the camera cap covers the lens of the camera. Then, a feature known as image touchup can be used to filter out the noise and focus the camera on the sample suspended from a metal rod (with two glass slides) held by a 3-axis positioner. A

region of interest (box) was then selected on the sample using the zone-selection option of the IR software to keep a record of temperature changes in real-time. A removable power trap (dark grey) was initially kept in the path of the light source for containing the heat coming from the source. A neutral density filter (Thor Labs, USA, spectral sensitivity: 200-1200 nm) was used to reduce the intensity of the light when power trap was removed. But in the current work, neutral density filter was removed when thermal responses were recorded in order to use the entire incident power to irradiate the sample. Polarization of light was an option by adjusting the polarizer angles. For the current work, polarized light was used. Three tunable bandpass filters (Semrock, VersaChrome Edge^{TM}, TBP01-617, 697, and 796) were used to tune wavelengths between 500-800 nm. The angle of the filter can be adjusted to set the wavelength of light (±5 nm). At each angle, a narrow band of 15 nm light can be used with the maxima representing the desired wavelength. The annexed (removable) spectral collimator between the IR camera and the sample can be used to display the spectra on a computer screen *via* the Avasoft spectral suite software. Figure 25, for example, shows how the light changes its color to green at a λ_{LPR} of 545 nm. A movable 0.5-inch germanium (Ge) broadband precision window (WG90530-G, Thor Labs, USA) with a transparency in 7000 nm to 12700 nm regime further allowed reduction of the intensity of light in few experiments. The Ge filter was placed 14 cm away from the camera lens in these experiments such that it covered the sample, i.e., focal plane of sample was surrounded by the focal plane of the filter. After the desired wavelength was selected, a rectangular cardboard box was placed over the sample to preclude deleterious effects of convection air currents and other external disturbances.

An option of series image capture was selected in the IR suite to record five thermal images per second. Prior to the experiment, the sample's position was adjusted in such a way that the particle

area can be illuminated by the white light. Corresponding controls were illuminated at similar locations as their respective samples. After the cardboard box was placed over the sample while the power trap was placed in the light path, and neutral density filter was removed out of the light path, ambient temperature data form the region of interest (ROI) was recorded for 10 s. Then, the power trap was removed from the light path for direct illumination of the sample, and 2 min 50 s heating data was recorded. Then the power trap was moved back into the light path and a 3 min cooling data was recorded. Image files were saved in TIFF format for obtaining high quality temperature maps.

Each image corresponded to 320 x 240 pixels. These images were then imported into MATLAB and an average temperature of each image was calculated from the a) area containing optical active nodes that was illuminated by a light spot and b) an immediate region circumscribing it.[88,89] The average temperature increases at the last instant of heating was then calculated in MATLAB. Along with each sample trial, a control trial was conducted where the control was illuminated at the wavelength that was used for the sample. The controls had similar thicknesses and PDMS-PEO composition, except for AuNPs. Average temperature increases in controls due to white light were then subtracted from average temperature increases of their matching samples to account for the local temperature changes due to dissipation of plasmon resonances from optically active nodes (cavities filled with AuNPs). Initial thermal experimentation dealt with Samples a-and-b (Figure 19), which were suspended using another PDMS film (fused to the samples) in the path of the light source. But for ease of handling, larger sample sizes (c-e) were considered later.

Figure 26 shows the spectra of the samples. The peak heights (PHs) were measured at λ_{LPR} and λ_{CLR} using absolute baseline as the basis, i.e., extinction of all trials (triplicate measurements) across 450-500 nm for each sample were averaged and plotted. A tangent line to this average

extinction curve at the ascending tail of plasmon peak was then considered as the absolute baseline. The distance between the absolute baseline and the maxima of the peak was then considered as the PH. For example, Figure 26 shows a black dashed line that is representative of an absolute baseline.
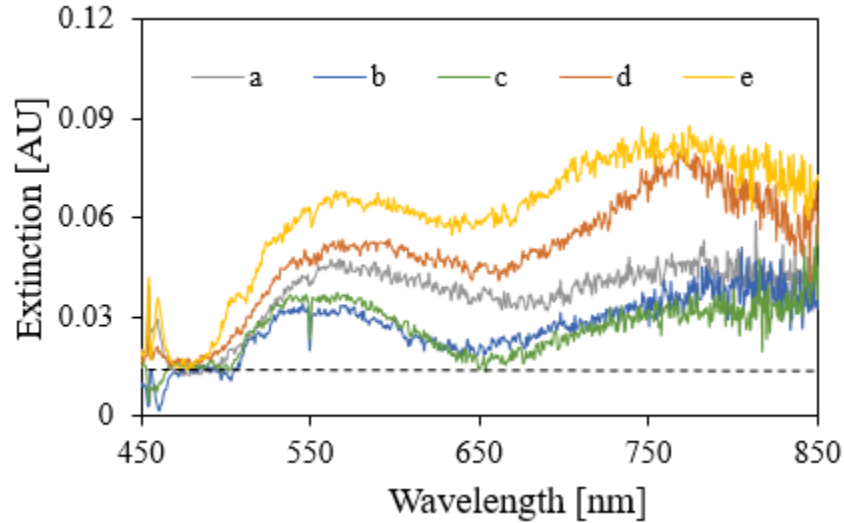
Figure 26. Extinction spectra (AU) of Samples a-to-e captured using white-light source illumination set-up.

Figure 27a shows the values of extinction/NP relative to NPs per unit area (cm^2) for 2-D arrays (0.014 % to 0.096 %, 100 nm NPs; filled green circles at λ_{LPR}; filled grey triangles at λ_{CLR}), and random dispersions of AuNP-PDMS previously produced by our group (Dunklin *et al.*[90–92]) that contain 16 nm (0.001 % to 0.015 %; filled violet diamonds) and 76 nm (0.005 % to 0.015 %; open violet diamonds) AuNPs. Additionally, random dispersion with 100 nm (0.0066 %; filled yellow diamond) AuNPs was produced in this work as a control. Pre-formed NPs were embedded in these dispersions.
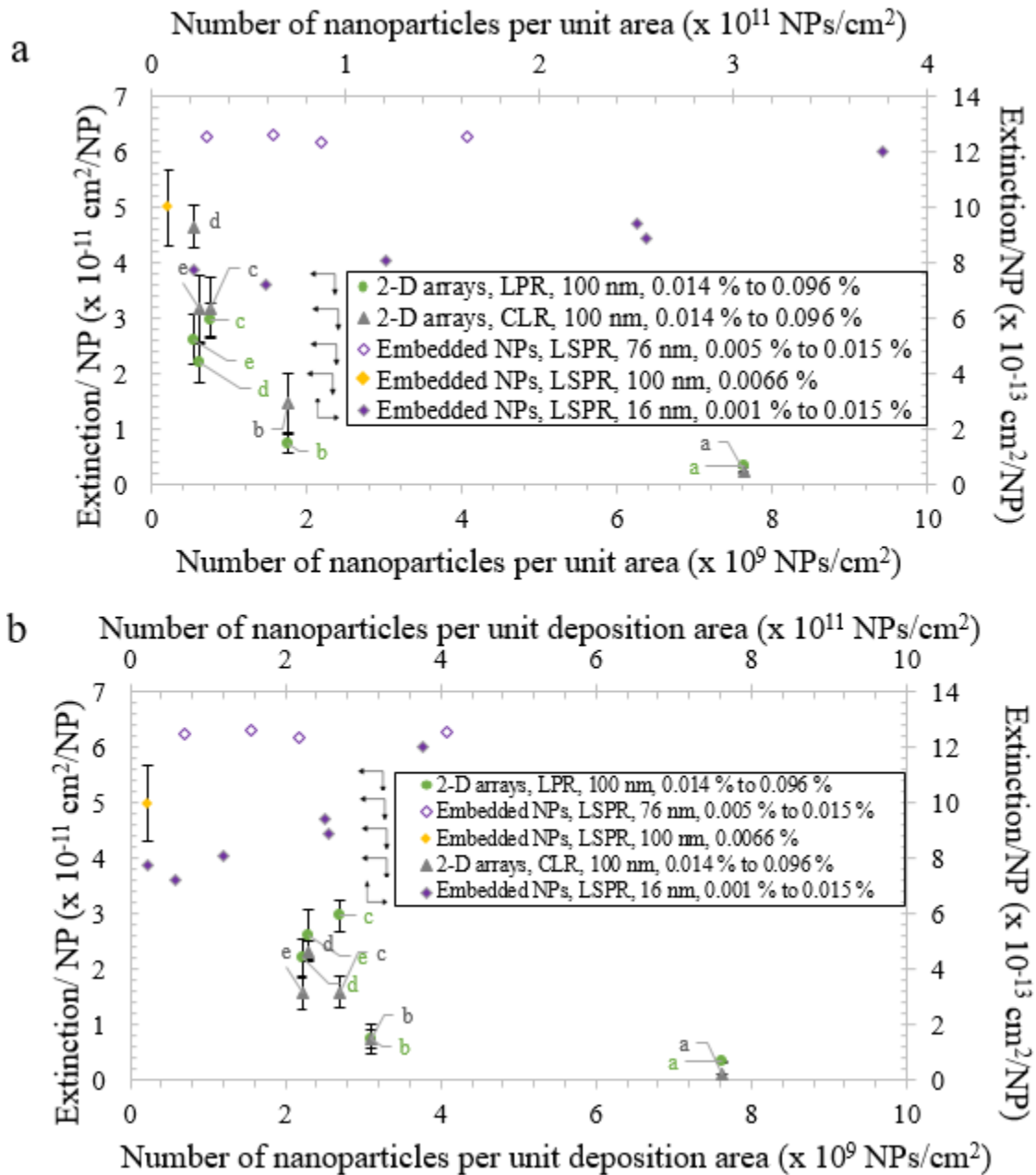
Figure 27. Extinction/NP for 2-D arrays (100 nm- filled green circles at λ_{LPR} and filled grey triangles at λ_{CLR}) compared with random dispersions of AuNPs (16 nm-filled violet diamonds, 76 nm-open violet diamonds, and 100 nm-filled yellow diamonds) in relation to a) number of NPs per unit area (cm^2), and b) number of NPs per unit deposition area (cm^2).

The extinction/NP for 2-D arrays was calculated by multiplying the measured PH of extinction (AU) at λ_{LPR} or λ_{CLR} by stamp area (cm^2), and dividing this product by the product of refractive index of the medium (1.45) and number of NPs. For random dispersions, extinction/NP was

49

calculated by dividing the measured PH of extinction (AU) at λ_{LPR} or λ_{CLR} by the product of refractive index of the medium (1.45), NPs/cm^3, and thickness (cm) of the films, respectively. The stamp area was replaced with deposition area in the calculations pertaining to Figure 27b.

Overall, the extinction/NP for 76 nm and 100 nm dispersions was up to ~6-fold higher compared to 100 nm, 2-D arrays at plasmon wavelengths (LPR for 2-D arrays and LSPR for random dispersions). It was assumed in the current work that all NPs were self-assembled on the stamp. Any minor losses of NPs to overhead cover slip surface during self-assembly may actually reduce the number of NPs on the stamp and concomitantly increase the value of extinction/NP for 2-D arrays (100 nm). Extinction/NP for 2-D arrays at λ_{CLR} was up to 2-fold higher compared to those at λ_{LPR} except for Sample a. Samples d-and-e which have a lattice spacing of 100 nm less compared to Samples a-and-c exhibited greater extinction/NP at λ_{CLR}. It may be speculated that the number of optically active nodes per unit area in samples d-and-e may be higher due to lower grating constant which may be causing higher extinction/NP. Data corresponding to 2-D arrays shifted right in Figure 27b when deposition area was considered in the abscissa. Extinction/NP of 2-D arrays (100 nm), and 76 nm and 100 nm random dispersions were up to 50-fold higher than 16 nm dispersions. Note that Figure 28 shows the Mie theory plots for extinction (solid line), absorption (dashed line) and scattering (dotted line) of 16 nm, 76 nm, and 100 nm NPs. The extinction cross section is the sum of scattering cross section and absorption cross section. For 100 nm NPs, scattering cross section is 75 % of its extinction cross section, whereas scattering cross section is ~50 % of extinction cross section for 76 nm NPs. For 16 nm NPs, it is close to zero. Also, extinction/NP for 100 nm dispersion is higher than 76 nm dispersion based on Mie theory plot. However, this is contradicted by Figures 27a and 27b, as NP losses to overhead coverslip occurred

during self-assembly. Additional data points corresponding to 100 nm dispersions at various Au

concentrations may provide more insight for reaching any concrete conclusions.
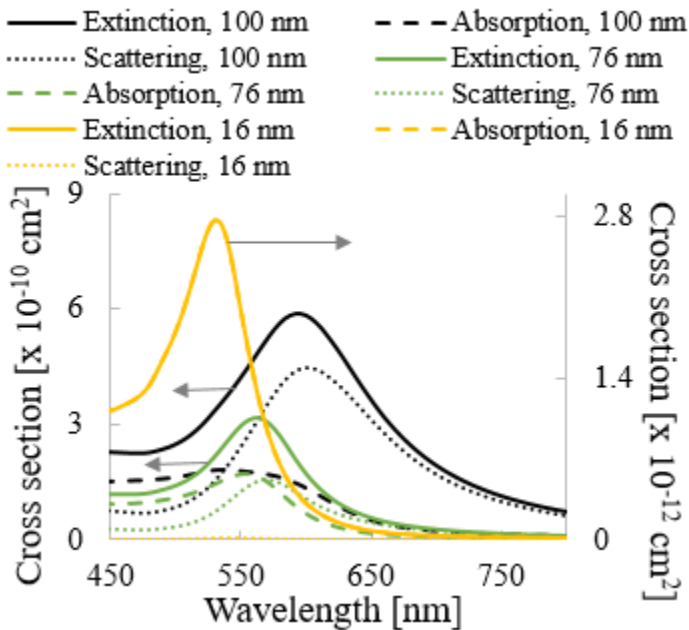
Figure 28. Mie theory plots of absorption, scattering and extinction cross sections for 16 nm, 76 nm, and 100 nm AuNPs.

Figure 29 shows similar trends where the abscissa was in terms of the number of NPs. The

corresponding sizes of samples, lattice configurations, and Au mass concentrations are enlisted in

Tables 6, 7, and 8 respectively.
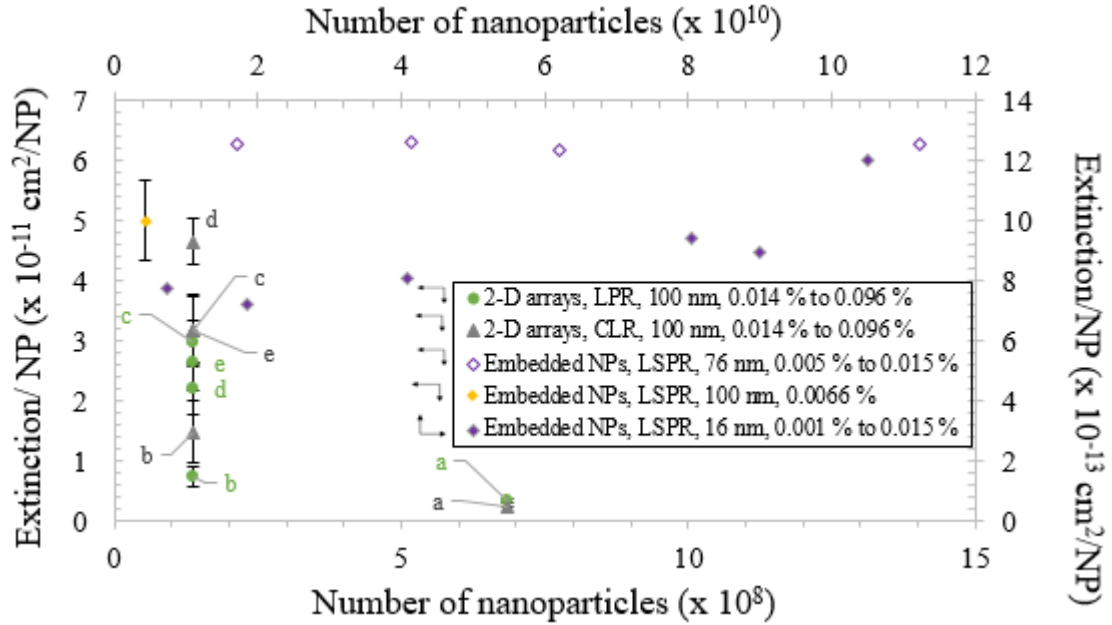
Figure 29. Extinction/NP for 2-D arrays (100 nm- filled green circles at λ_{LPR} and filled grey triangles at λ_{CLR}) compared to random dispersions of AuNPs (16 nm-filled violet diamonds, 76 nm-open violet diamonds, and 100 nm-filled yellow diamonds) in relation to number of NPs.

Table 6. Sample dimensions.

Sample	Length [cm]	Width [cm]	Thickness [cm]
a	0.3	0.3	0.085
b	0.3	0.26	0.032
c	0.45	0.4	0.032
d	0.5	0.5	0.032
e	0.5	0.45	0.032

Table 7. Lattice configurations of Samples a-to-e.

Sample	Lattice spacing [nm]	Cavity depth [nm]	Cavity diameter [nm]
a, b, c	700	150	260
d, e	600	150	260

Table 8. Au mass concentrations in 2-D arrays (Samples a-to-e) and random dispersions

Sample	Mass, mg	Mass %
a	0.006	0.095879846
b	0.0012	0.049714622
c	0.0012	0.021818182
d	0.0012	0.013953488
e	0.0012	0.014634146
100 nm:	0.000477675	0.0066
76 nm:		
	0.000947209	0.005
	0.00341382	0.0075
	0.002287117	0.01
	0.006187938	0.015
16 nm:		
	0.000298514	0.001
	0.000757252	0.002
	0.001677512	0.005
	0.003696747	0.0075
	0.003311903	0.01
	0.004318935	0.015

After measuring the optical responses of Samples a-to-e with white light source illumination set-up, their thermal responses were measured at similar aperture size or FOI (2.17 mm). Optical responses at λ_{LPR} (545-570 nm) and λ_{CLR} (747-780 nm) suggested that samples may exhibit temperature increases at these maximas. Hence, thermal characterization was conducted at these wavelengths. Additionally, wavelengths corresponding to valleys (dips) which appeared between LPR and CLR features in the 650-700 nm regime were also considered. Initial step of thermal characterization involved measurement of incident powers (using a power meter, PM 100D, Thor Labs, USA) in mW at the lowest intensity of white light source across λ_{LPR} (green), λ_{valley} (red), and λ_{CLR} (grey). Note that the color of light at λ_{LPR}, λ_{valley}, and λ_{CLR} are green, red, and colorless, respectively. Figure 30 indicated that incident power decreased from ~6 mW at λ_{LPR} to ~2 mW at λ_{CLR}.
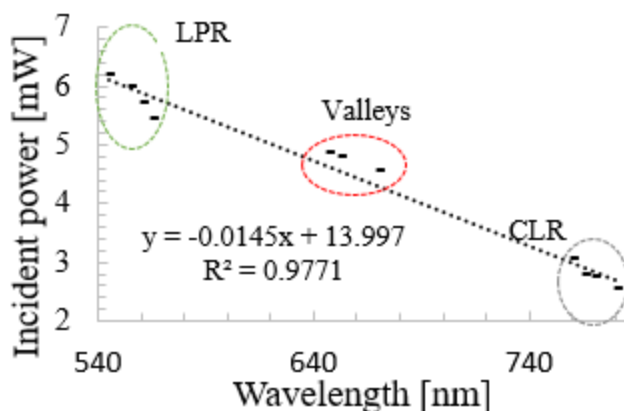
Figure 30. Decrease of incident power (mW) with increase in wavelength.

This suggested that temperature increases in controls due to white light irradiation need to be subtracted from temperature increases in samples with NPs at varying wavelengths, and powers for a common basis of comparison. The dimensions of controls used were similar to samples.

In order to compare the thermal responses of 2-D arrays in the current work with AuNP-polymer systems characterized to date, two bases of comparisons were considered. Variables such as ΔT (temperature increase in sample calculated based on the difference between ambient temperature and equilibrium heating temperature – similar temperature increase in control), incident intensity, which is the ratio of incident power in milliwatts (mW) divided by the area of the beam spot in cm^2 (spot size in the current work: 2.17 mm), and % Au concentration were considered based on the availability of data from literature. The first basis of comparison was ΔT / incident intensity. Availability of Au % further led to the use of a second basis of comparison, i.e., ΔT / (incident intensity * % Au). Figures 31a and 31b compare the current work with previous work based on these two bases of comparison at plasmon resonances. Each data point corresponding to 2-D arrays, and 76 nm and 100 nm dispersions represents an average of three trials. Each data point for 16 nm dispersion represents an average of two trials. The error bars were calculated using error propagation, where the error in temperature increases (ΔT = temperature of sample – temperature

54

of control) from three trials was considered as the basis. Thermal responses correspond to 2 min, 50 s of heating period when the samples and controls were irradiated with white light at the lowest intensity, and different monochromatic wavelengths. Figure 31a compares the responses from a) 2-D arrays (filled green circles; 0.014 % to 0.096 %), b) 16 nm (filled violet diamonds; 0.001 % to 0.015 %), c) 76 nm (filled violet diamond; 0.005 %), and d) 100 nm (filled yellow diamond; 0.0066 %) random dispersions of AuNP-PDMS (with pre-formed NPs),[90,92] e) a broadband multilayer plasmonic absorber consisting of a continuous Au back reflector (100 nm), a continuous silicon dioxide dielectric layer (60 nm), and a patterned Au front layer (100 nm) (red cross, Tagliabu *et al.*),[93] f) PDMS dispersions with reduced gold nanoparticles (*via* silicon hydroxide groups; blue asterisks, Li *et al.*),[94] and g) cellulose acetate dispersions where AuNPs using sodium borohydride (black cross, Vanherck *et al.*).[95] Note that while a laser with λ_{LSPR} of 514 nm (argon-ion) was used by Li *et al.* and Vanherck *et al.*, a laser at 532 nm was used by Tagliabue *et al.* In contrast to a monochromatic, coherent source of irradiation (laser), 16 nm, 76 nm, and 100 nm dispersions, and 2-D arrays were irradiated with an incoherent, white light source and still showed a thermal response. Especially, 76 nm and 100 nm dispersions were irradiated with white light when Ge filter was moved into the path for reducing the intensity of light further. However, Ge filter caused the focus of the sample to deteriorate which eventually gave rise to high error bars. Overall, 16 nm dispersions showed up to 6-fold higher responses compared to 2-D arrays. The 100 nm and 76 nm dispersions had responses within the higher and lower bounds of responses of 2-D arrays (considering all arrays). Data corresponding to Li *et al.* ranged between 0.004-0.01 K-cm^{-2} mW^{-1}. Delta T corresponding to this data was calculated with respect to an ambient temperature baseline because temperature increase in control (PDMS without NPs) was unavailable. Samples

prepared by Vanherck *et al.* had the highest thermal responses (0.1-0.2 K-cm^{-2} mW^{-1}). However, these trends slightly changed after accounting Au % in the calculations, as shown in Figure 31b.
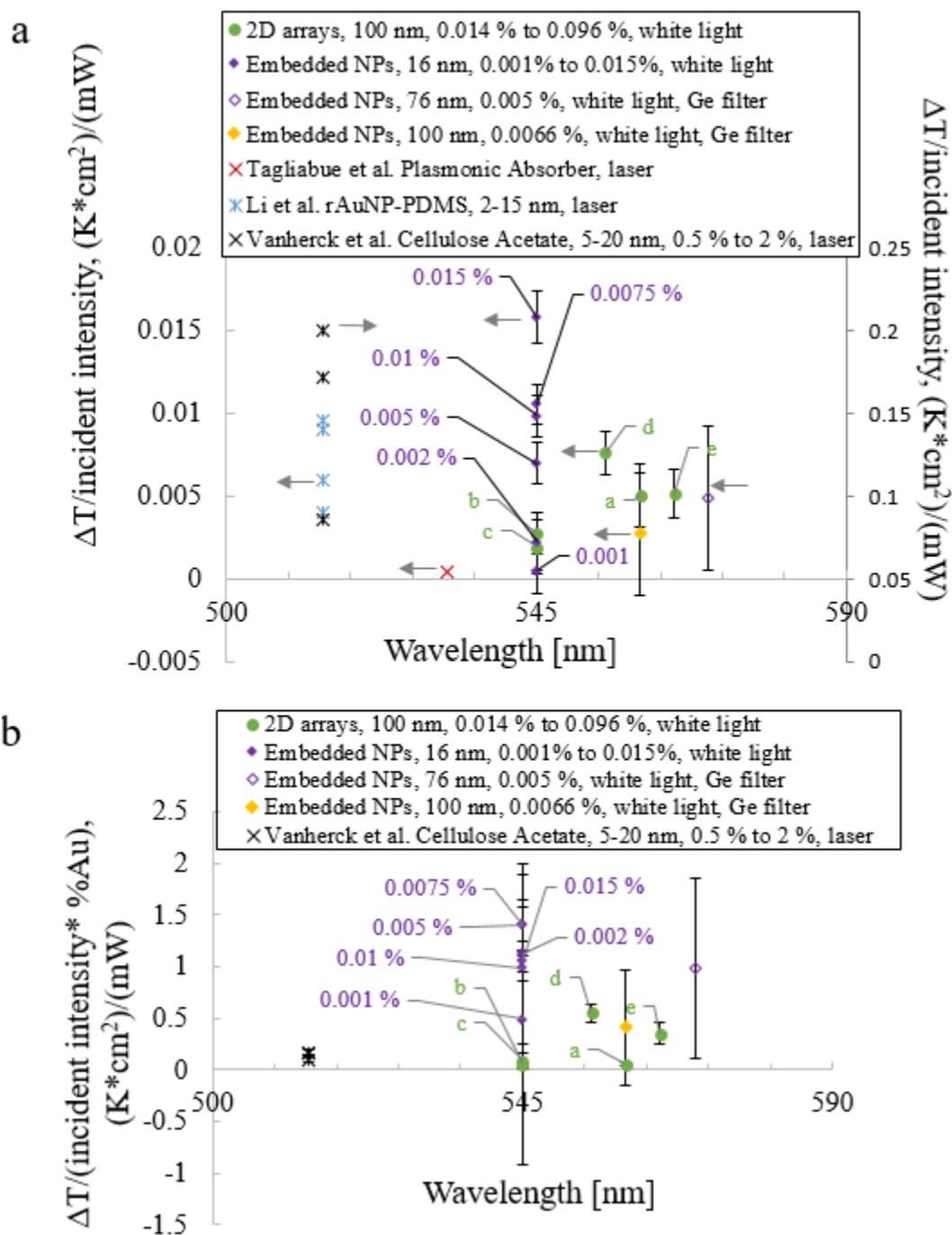
Figure 31. Comparison of thermal responses from different systems in terms of a) ΔT / incident intensity, and b) ΔT / (incident intensity * % Au). Films irradiated with white light were 2-D arrays (filled green circles; 0.014 % to 0.096 %), and random dispersions containing NPs such as 16 nm (filled violet diamonds; 0.001 % to 0.015 %), 76 nm (filled violet diamond;0.005 %), and 100 nm

(filled yellow diamond; 0.0066 %). Films irradiated with laser are represented by red cross (Tagliabue et al.), blue asterisks (Li et al.), and black crosses (Vanherck et al.).

While the trends corresponding to random dispersions and 2-D arrays remained similar at higher values of ordinate axis (up to 2 K-cm^{-2} mW^{-1}), data corresponding to the work of Vanherck *et al.* fell close to 0.1 K-cm^{-2} mW^{-1}. Works to date considered AuNP-PDMS dispersions and focused on laser irradiation of single/multivalent particle systems at plasmon wavelengths.[90,92–96] This work attempted to fill the knowledge gap associated with thermal behavior of 2-D arrays at different wavelengths (visible to NIR).

Figure 32a shows the experimental surface temperature profiles at equilibrium (160 s heating period) of Samples a-to-e at λ_{LPR} where the scale bars represent the temperatures which went up to ~302 K. The dashed regions overlaid on the plots represent the areas where particles self-assembled. Solid circles enclose the zones (10 pixels in diameter) considered by MATLAB subroutine to calculate the temperature increases in samples and their respective controls for estimating ΔT. Note that the size of the circle was always maintained at 10 pixels (diameter) when the thermal analysis was conducted.

Figure 32b shows various thermal responses of 2-D arrays in tandem with random dispersions at LSPR maximas ($\lambda_{545-570\,nm}$, 16 nm NPs, filled violet diamonds, 0.001 % to 0.015 %; $\lambda_{570\,nm}$, 76 nm dispersions, open violet diamond, 0.005 %; $\lambda_{560\,nm}$, 100 nm dispersions, filled yellow diamond, 0.0066 %), LPR maximas ($\lambda_{545-565\,nm}$, 2-D arrays-filled green circles), CLR maximas ($\lambda_{760-780\,nm}$, 2-D arrays-filled grey triangles, and open grey triangles associated with Ge filter; $\lambda_{770\,nm}$, 76 nm dispersions, open violet diamond, Ge filter; $\lambda_{770\,nm}$, 100 nm dispersions, filled yellow diamond, Ge filter), and valley minimas ($\lambda_{647-670\,nm}$, 2-D arrays-filled red squares; $\lambda_{660\,nm}$, 76 nm dispersions, open violet diamond, Ge filter; $\lambda_{660\,nm}$, 100 nm dispersions, filled yellow diamond, Ge filter).
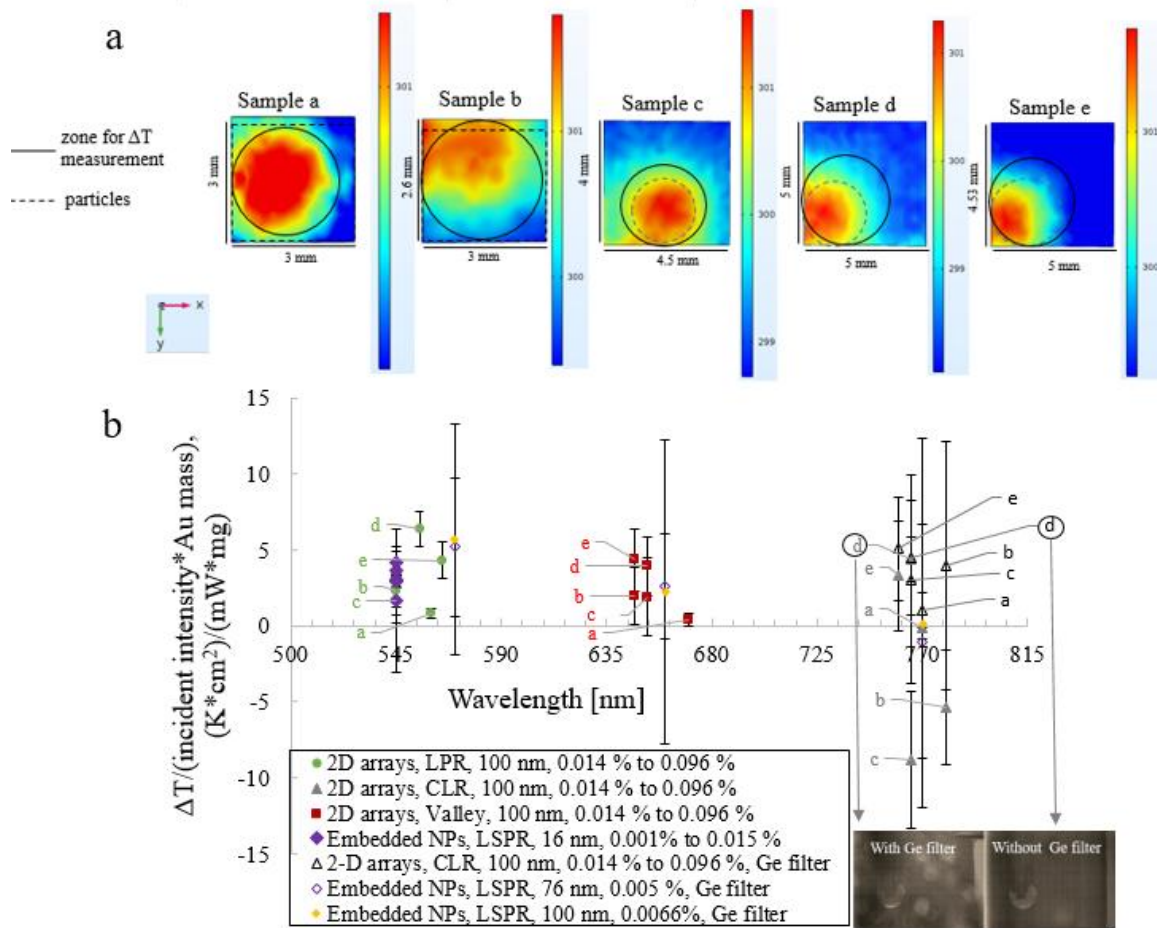
Figure 32.a) Experimental surface temperature plots (160 s heating) of Samples a-to-e at λ_{LPR} where particle zones and ΔT calculation zones are enclosed with dashed and solid shapes respectively, b) Thermal responses of 2-D arrays across λ_{LPR} (filled green circles), λ_{valley} (filled red squares), and λ_{CLR} (filled grey triangles; open grey triangles with Ge filter) in comparison with random dispersions of 16 nm (filled violet diamonds), 76 nm (open violet diamond, Ge filter), and 100 nm (filled yellow diamond, Ge filter) NPs.

The ordinate axis is shown in terms of ΔT during 2 min, 50 s heating, incident intensity, and Au mass calculated by multiplying the mass of a single NP with the number of NPs. The thermal responses of 2-D arrays were positive at λ_{LPR} and $\lambda_{Valleys}$, while they seemed to be negative for Samples a-to-c at λ_{CLR}. The temperature increases of samples relative to control were positive at λ_{CLR} for Samples d-and-e which had a grating constant of 600 nm (Type 1, Table 3) and greater extinction/NP on average compared to other samples (Type 2, Table 3). Also, Samples d-and-e

showed enhanced responses at λ_{LPR} and $\lambda_{Valleys}$. The 16 nm random dispersions (0.001 % to 0.015 % Au) showed comparable responses at λ_{LPR} as 2-D arrays. Although it was speculated that 2-D arrays may exhibit a thermal response at $\lambda_{Valleys}$ owing to broadband nature of plasmon resonance for 100 nm NPs (Mie plot, Figure 28), positive responses for Samples d-and-e were not expected at λ_{CLR}. Negative responses for Samples a-to-c at λ_{CLR} contradicted these results. Hence, Ge filter was incorporated into the system to reduce the intensity of white light and corresponding temperature spikes at first instances of heating and cooling, and prevent any deleterious effects of scattering that may have affected the thermal responses captured by the IR camera. The inset of Figure 32b shows pictures of Sample d taped to a PDMS film and suspended in air vertically, with and without Ge filter in the light path. Note that the focus of the sample with Ge filter is low which led to high error bars in the thermal responses estimated. The average thermal responses of 2-D arrays increased for all samples (except d) and were positive at λ_{CLR} after Ge filter was used, which are shown by grey triangles. However, high error bars suggested more control experiments were needed. The 76 nm and 100 nm dispersions; furthermore, were considered as negative controls that were irradiated when Ge filter was in the light path. They were irradiated at $\lambda_{660\,nm}$ and $\lambda_{770\,nm}$ in addition to λ_{LSPR}. The wavelengths, 660 nm and 700 nm, represent the average of all wavelengths corresponding to 2-D arrays at their corresponding valley and CLR resonances, respectively. Interestingly, the average thermal responses of random dispersions with particles of comparable sizes as in 2-D arrays decreased to almost zero going from λ_{LPR} to λ_{CLR}. This suggested that 2-D arrays may be prone to thermoplasmonic heating even at λ_{CLR} or NIR region compared with random dispersions. The occurrence of temperature increases at λ_{valley} and λ_{CLR} is an interesting outcome of these results. The absorption cross section of plasmonic NPs extends up to ~660 nm (Figure 28), which suggests that there may be slight excitation of AuNPs and occurrence

of plasmon resonance at λ_{valley} that could lead to probable temperature increases. However, ostensible temperature increases at λ_{CLR} was an interesting new finding. The mechanism that causes a temperature increase at λ_{CLR} is unknown, but ideas related to its occurrence can be interesting to consider. From the viewpoint of quantum-mechanical, analytical approach of dual resonances discussed in Chapter 1 (Section 1.2.2), it is possible that a narrow band resonance can excite a broadband plasmon resonance provided that these resonances are coupled. It may be possible that CLR is exciting the LPR and causing a temperature increase, but there is no solid evidence to corroborate this idea. Results herein suggest that NIR energy might excite LPR and elicit a temperature increase in samples containing 2-D NP lattices.

Figure 32b does not account for fraction of the power that is actually absorbed by the samples which resulted in thermoplasmonic heating. Only incident intensity in terms of incident power was considered. These results can also be plotted in terms of "extinguished intensity" and "absorbed, extinguished intensity". Consider Figure 33 which schematically depicts important optical relations that help to understand these terms. First, incident power is a summation of reflected (Figure 33a), transmitted (Figure 33b), and attenuated powers. Attenuated power can be further written in terms of scattering (Figure 33 c), diffraction because two NPs (Figure 33d), and absorption (Figure 33e) by NPs. Measured transmitted power was subtracted from the measured incident power at λ_{LPR} (Figure 32b) to calculate the extinguished power and the corresponding extinguished intensity.
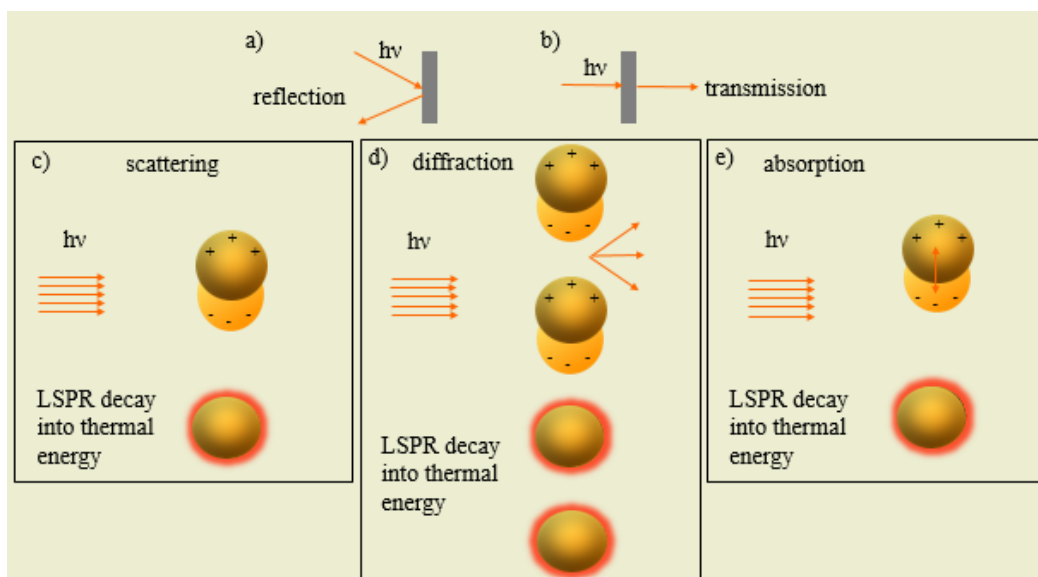
Figure 33. Optics related to incident power, which is the sum of reflection, transmission, and attenuation. Attenuation is further equal to the sum of scattering, diffraction, and absorption.

Figure 34a shows the thermal responses in terms of ΔT divided by the product of "extinguished power" and Au mass vs the wavelength (λ_{LPR}). Random dispersions with 16 nm NPs showed higher thermal responses compared to 2-D arrays on the basis of extinguished power. Results pertaining to 76 nm and 100 nm dispersions were inconclusive due to high error bars. The thermal responses shot up by ~2-fold for 2-D arrays while 3- to 8-fold for 16 nm dispersions compared to results shown in Figure 32b. Still, the extinguished power does not account for the absorption of samples (and particles). Therefore, the extinguished power was multiplied by the absorption fraction (absorption/extinction) at the corresponding λ_{LPR} of the sample (Mie plot, Figure 28, 100 nm NP) to give the absorbed, extinguished power.[97] This power was used as the basis for calculating absorbed, extinguished intensity (Figure 34b). The thermal responses (ordinate) shot up 5- to 6-fold for 2-D arrays (compared to Figure 32 b) and remained the same for 16 nm dispersions (see Figure 32b). This is because % scattering is close to zero at λ_{LPR}, and almost all absorption accounts for extinction for 16 nm dispersions (see Figure 28, Mie plot). As can be

observed in Figure 34b, the average thermal response for Samples d-and-e (Type 1, Table 3) touched ~31 K cm^2 mW^{-1} mg^{-1} and ~25 K cm^2 mW^{-1} mg^{-1}, respectively.
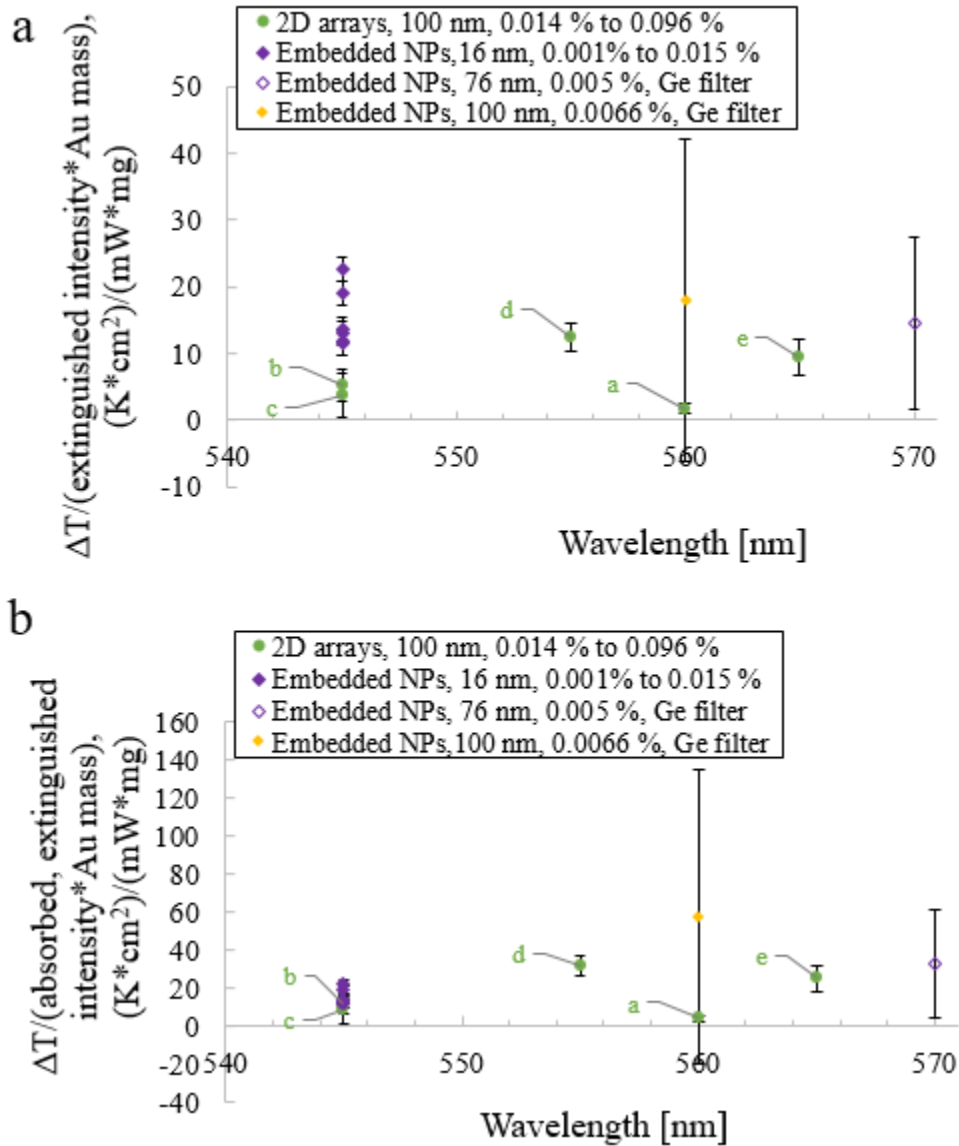
Figure 34. a) Thermal responses in terms of extinguished intensity vs wavelength at λ_{LPR}, and b) thermal responses in terms of absorbed, extinguished intensity vs wavelength at λ_{LPR}. 2-D arrays are represented by filled green circles, whereas filled violet diamonds correspond to 16 nm dispersions, open violet diamond corresponds to 76 nm dispersions, and filled yellow diamond corresponds to 100 nm dispersions.

Figures 34a and 34b represent both optical (Mie theory) and thermal (local temperature increases due to thermoplasmonic heating) responses of arrays and dispersions. This is one of the unique opto-thermal characterization methods used in the current work. In order to understand opto-thermal effects (solely in terms of absorbed, extinguished intensity) in 2-D arrays and random dispersions in relation to nanoparticle density, the abscissas in Figures 34a and 34b were replaced with NPs per unit area (cm^2) and NPs per unit deposition area (cm^2), respectively, to give Figures 35a and 35b. Samples d-and-e exhibited enhanced thermal behavior at a low NPs/cm^2 compared to other samples which had a 700 nm grating constant. It is speculated that higher number of active nodes per unit area in 600 nm grating may have contributed to this result.

The data corresponding to 2-D arrays shifted right (up to ~2-fold) when deposition area was considered in the abscissa. Overall, 2-D arrays, and 76 nm and 100 nm dispersions exhibited enhanced responses at two orders-of-magnitude lower nanoparticle density compared to 16 nm dispersions.
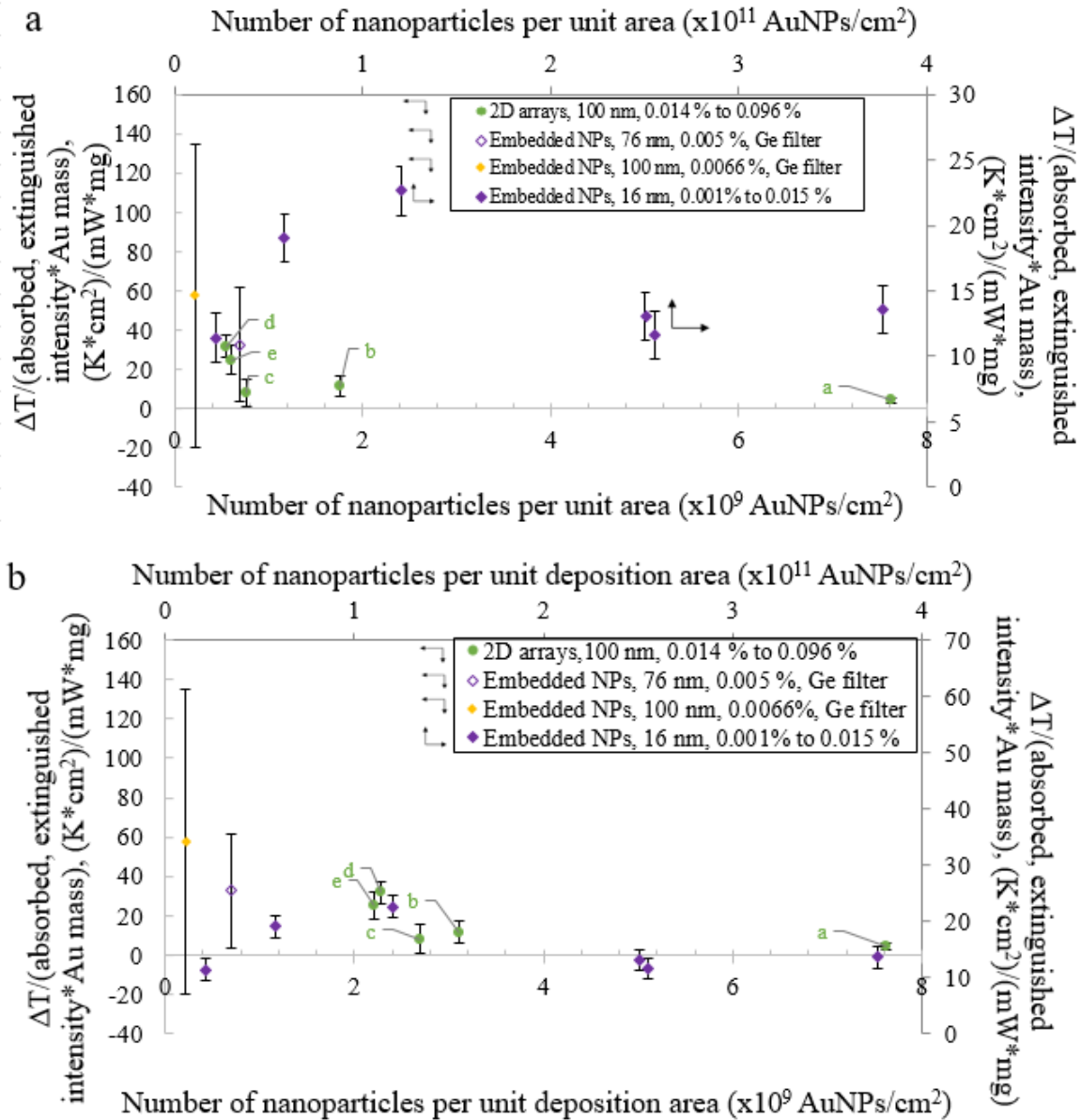
Figure 35. a) Thermal responses in terms of absorbed, extinguished intensity vs NPs per unit area (cm^2) at λ_{LPR}, and b) thermal responses in terms of absorbed, extinguished intensity vs NPs per unit deposition area (cm^2) at λ_{LPR}. 2-D arrays are represented by filled green circles, whereas filled violet diamonds correspond to 16 nm dispersions, open violet diamond corresponds to 76 nm dispersions, and filled yellow diamond corresponds to 100 nm dispersions.

Figures 36 shows the experimental heating-cooling curves, and topographical 3-D equilibrium

(160 s heating) temperature profiles of Sample a (and control), which is representative of 700 nm

lattice spacing (Type 2, Table 3) at λ_{LPR}. Figures 36a and 36b show the heating-cooling curve (0-

6 min) of sample and temperature map of sample relative to its length and width, respectively. Figures 36c and 36d show the heating-cooling curve (0-6 min) of control and temperature map of control relative to its dimensions, respectively. This particular sample was illuminated on center-left. Figures 37-40 represent similar profiles pertaining to Samples b-to-e, respectively. Note that Sample b (control) was illuminated near upper-left, Sample c (control) was illuminated at bottom-center, and Samples (and corresponding controls) d-and-e were illuminated at lower-left. Irradiation zone matches exactly with the zones particles assembled in Samples c-to-e. Samples a-and-b had particle coverage over a vast area, but they were irradiated only partially. Note that Sub-Figures a and c of Figures 36-40 correspond to heating-cooling curves of samples and their corresponding controls. In each case, temperature increase in sample was higher compared to control. However, temperature spikes at first instances of heating (post-10 s ambient) and cooling (post 2 min 50 s of heating) are caused due to white light which prevented from knowing the exact points in the temperature profiles which are appropriate for calculating heating and cooling time constants. Previous work within the group showed that these time constants are generally linear at the first instant of heating and cooling.[88] Using a combination of Ge and neutral density filters may: a) help reduce the excess intensity of white light, b) give zero temperature spikes in controls, and c) identify temperature increases solely due to thermoplasmonic heating in samples without the need for additional analysis in estimating ΔT.
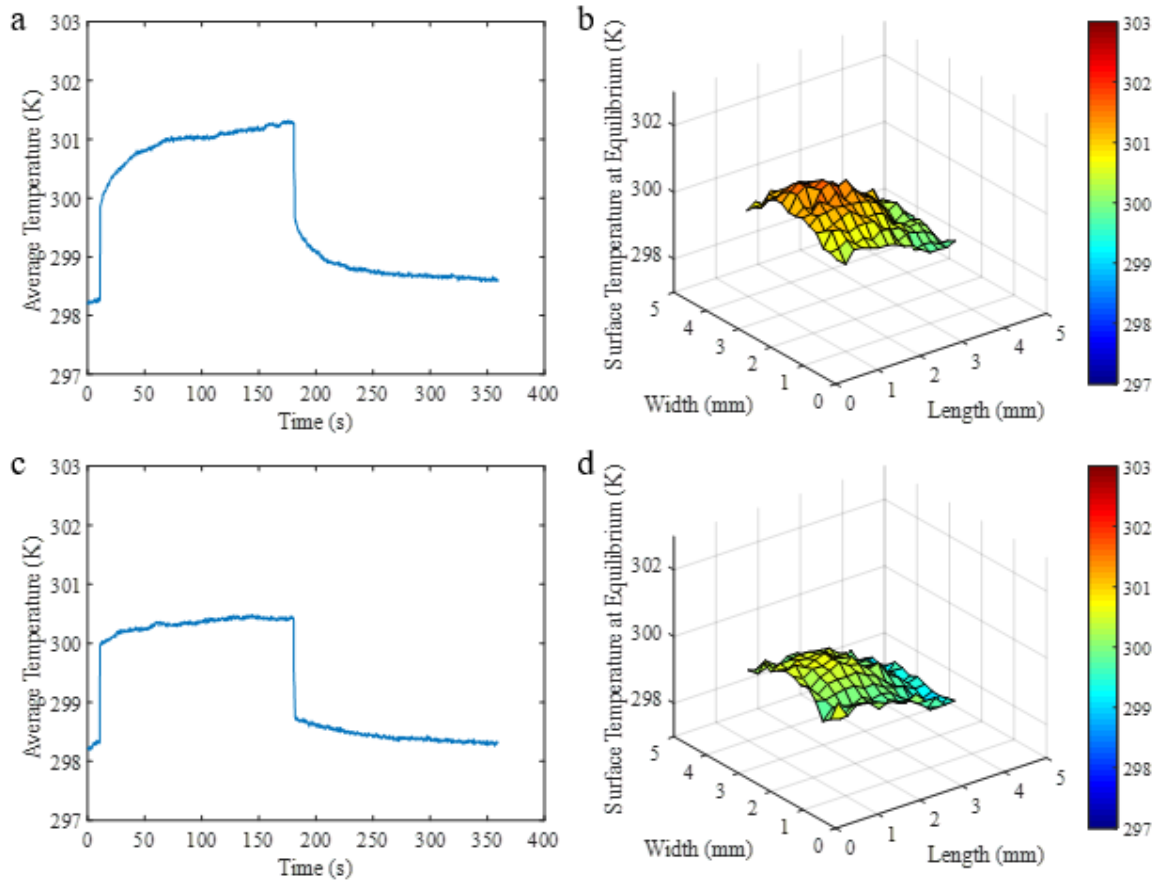
Figure 36. Experimental thermal profiles of Sample a (700 nm spacing, Type 2, Table 3) and its respective control: a) heating-cooling curve of sample, b) equilibrium (160 s heating) topographical temperature map of sample relative to this length and width (illuminated at center-left), c) heating-cooling curve of control, and d) topographical temperature map of control relative to this length and width (illuminated at center-left).
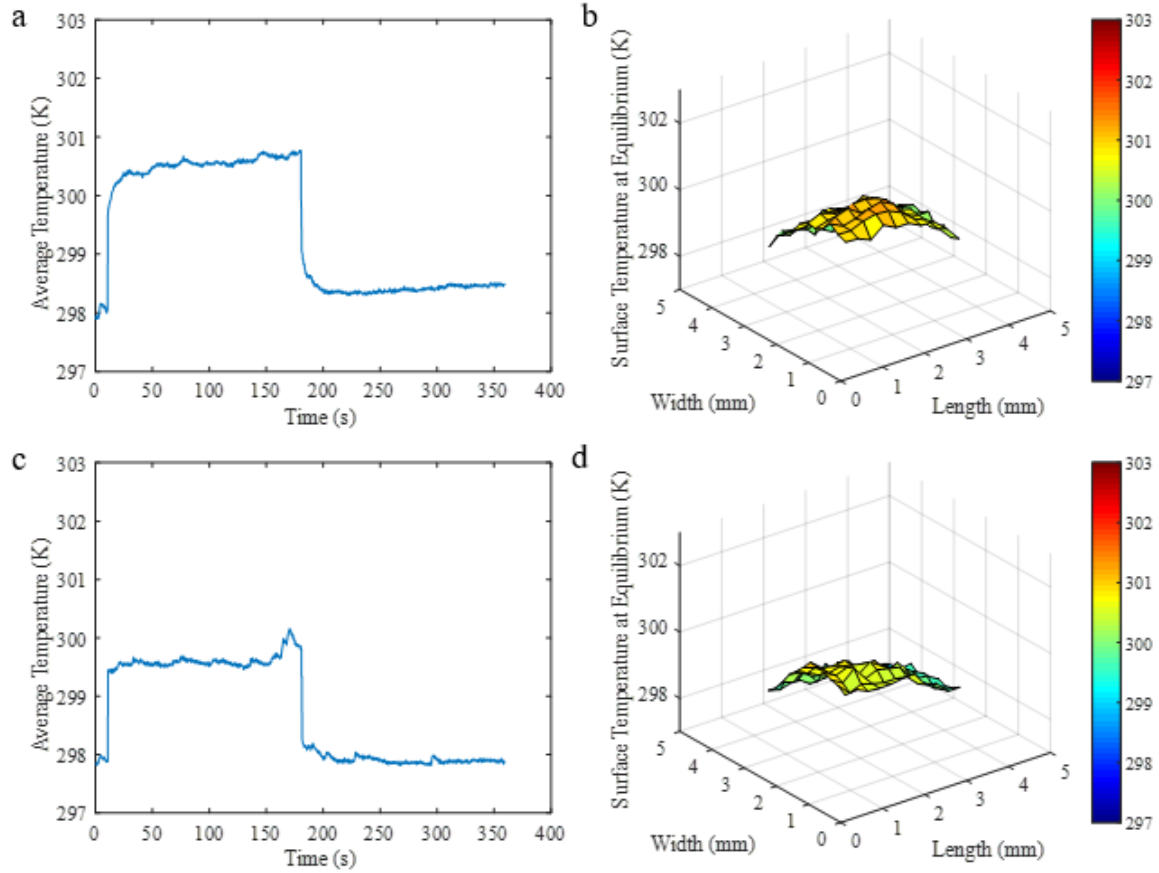
Figure 37. Experimental thermal profiles of Sample b (700 nm spacing, Type 2, Table 3) and its respective control: a) heating-cooling curve of sample, b) equilibrium (160 s heating) topographical temperature map of sample relative to this length and width (illuminated near upper-left), c) heating-cooling curve of control, and d) topographical temperature map of control relative to this length and width (illuminated near upper-left).
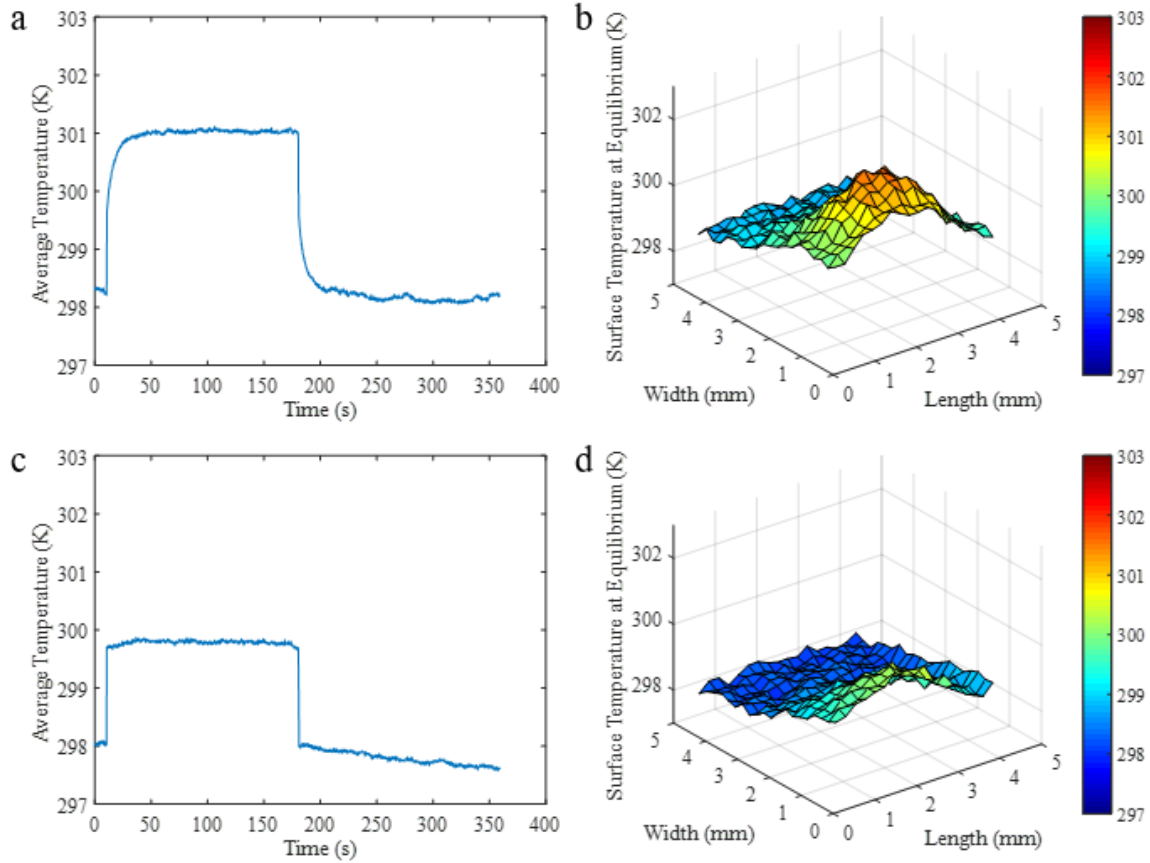
Figure 38. Experimental thermal profiles of Sample c (700 nm spacing, Type 2, Table 3) and its respective control: a) heating-cooling curve of sample, b) equilibrium (160 s heating) topographical temperature map of sample relative to this length and width (illuminated at bottom-center), c) heating-cooling curve of control, and d) topographical temperature map of control relative to this length and width (illuminated at bottom-center).
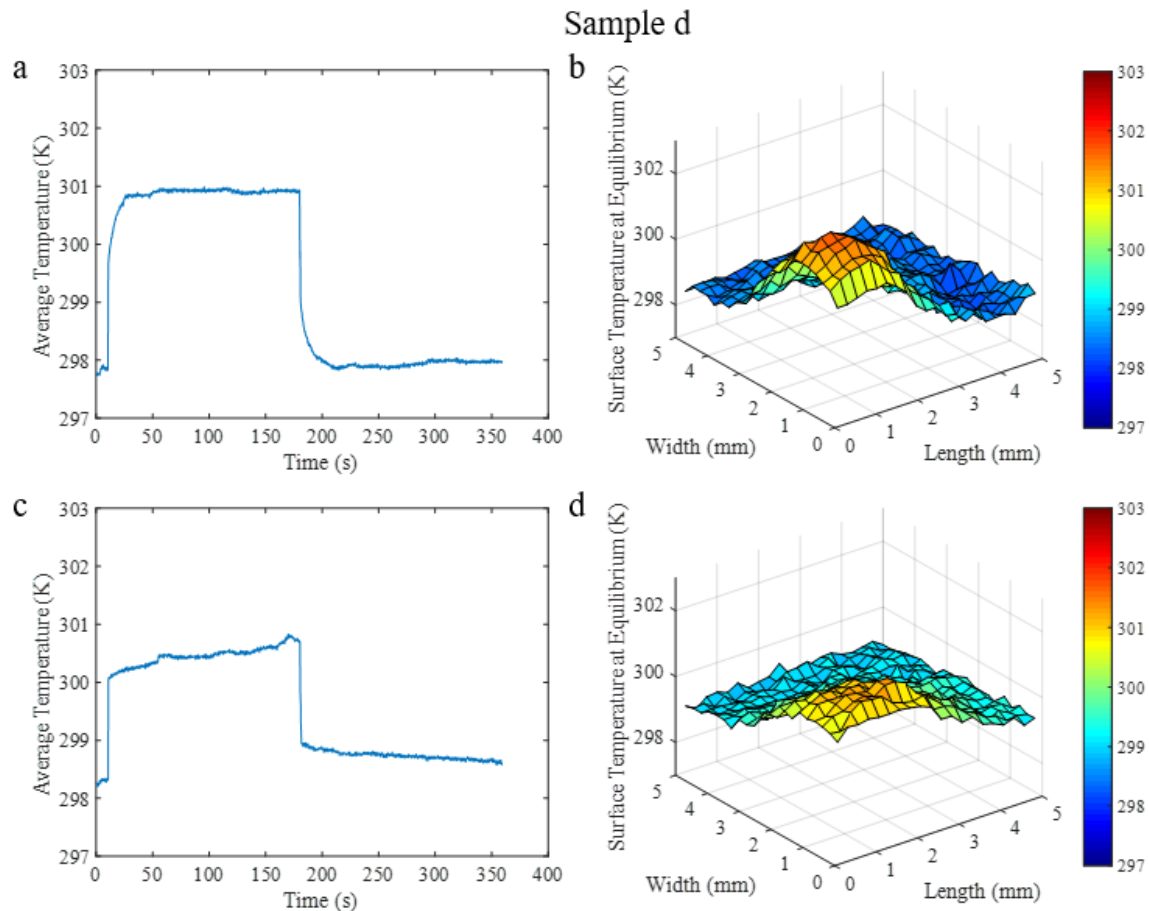
Figure 39. Experimental thermal profiles of Sample d (600 nm spacing, Type 1, Table 3) and its respective control: a) heating-cooling curve of sample, b) equilibrium (160 s heating) topographical temperature map of sample relative to this length and width (illuminated at lower-left), c) heating-cooling curve of control, and d) topographical temperature map of control relative to this length and width (illuminated at lower-left).

69
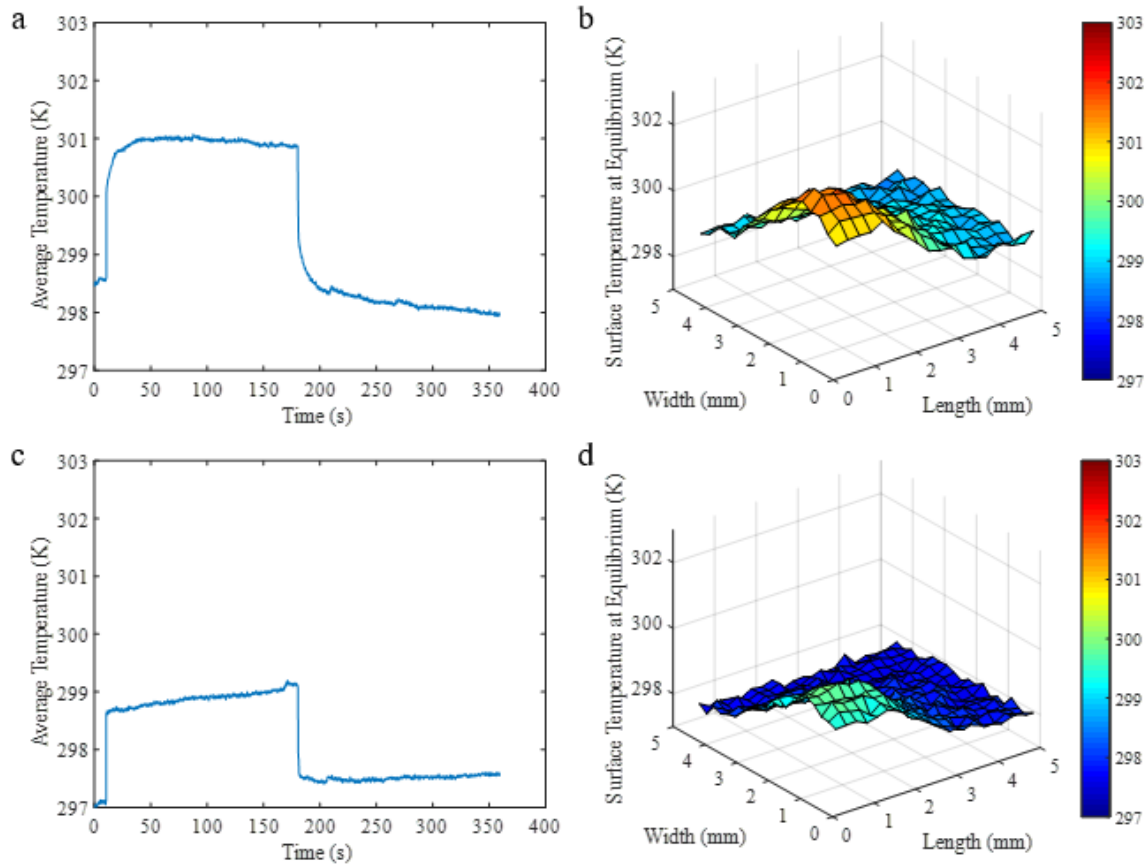
Figure 40. Experimental thermal profiles of Sample d (600 nm spacing, Type 1, Table 3) and its respective control: a) heating-cooling curve of sample, b) equilibrium (160 s heating) topographical temperature map of sample relative to this length and width (illuminated at bottom left), c) heating-cooling curve of control, and d) topographical temperature map of control relative to this length and width (illuminated at lower-left).

Figures 41a and 41b show the heating-cooling curves of 76 nm dispersion (0.005 %) and the corresponding control, respectively. Similarly, Figures 41c and 41d show the heating-cooling curves of 100 nm dispersion (0.0066 %) and the corresponding control, respectively. Note that the presence of Ge filter in the light path decreased temperature spikes; however, it resulted in more uncertainty in calculating time constants, and ΔT.
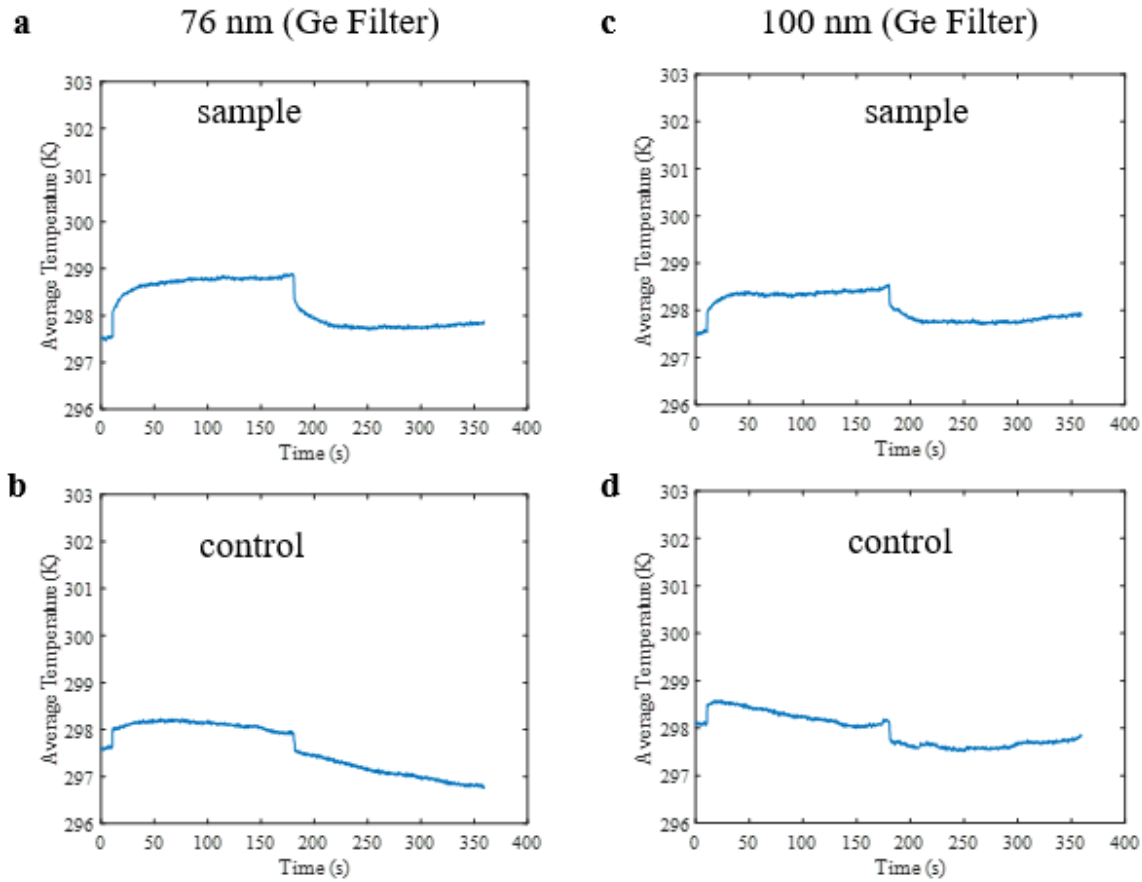
Figure 41. Thermal profiles obtained with Ge filter in light path: a) and b) show the heating-cooling curves of 76 nm dispersion (0.005 %) and the corresponding control, respectively. Similarly, c) and d) show the heating-cooling curves of 100 nm dispersion (0.0066 %) and the corresponding control, respectively.

4.2. Finite element modeling (COMSOL)

This work used The Heat Transfer in Solids module of COMSOL Multiphysics (COMSOL 5.3a, Stockholm, Sweden) for simulating the thermal profiles of 2-D arrays. The model used cross-platform finite element analysis to mimic transient heat transfer in the system assuming heat flux through Rayleigh convection, Fourier heat conduction and Stefan-Boltzmann radiation. When the heat source (laser) was applied, convective and radiative cooling boundary conditions determined the heat transfer rate into the surrounding environment (air). Temperature-dependent specific heat capacity, density, and thermal conductivity of bulk PDMS governed the temperature profiles

71

within the arrays. Previous work suggested that microscopic thermal transport in nanocomposites agree with bulk polymer when conductive inclusions or NPs are at relatively low concentrations.[98] Additionally, the PDMS-b-PEO copolymer concentration was 2 % in the membranes wherein major constituent of the copolymer was PDMS (75 % based on vendor specifications).

Following are the equations which represent the heat transfer mechanisms in the model. The Heat Transfer interface in COMSOL uses an elliptic partial differential equation for the Temperature, T, in the presence of zero velocity of fluid surrounding the material, as shown in Equation 4.1a, i.e., the equation governing energy conservation at steady-state:[99,100]

$$\rho C_p \frac{\partial T}{\partial t} + \nabla \cdot (q) = Q \tag{4.1a}$$

where ρ is the density of the material, C_p is specific heat capacity of the material, T is temperature, t is time, ∇ is the Del operator, q is the heat flux vector which is a function of the temperature gradient (∇T) and thermal conductivity of the material (k), as shown in Equation 4.1b (Fourier's law), and Q is the sum of total external heat sources (or sinks). Here, q is given by:

$$q = -k\nabla T \tag{4.1b}$$

The Dirichlet and Neumann boundary conditions at some boundaries (for Equation 4.1a) are given by:

$$T = T_0 \tag{4.1c}$$

$$-n \cdot (q) = q_0 \tag{4.1.d}$$

where n is the normal vector to the film surface, T_0 represents constraint temperatures, and q_0 represents constraint heat fluxes. Non-linearity can crop up occasionally in these equations, owing to one or more of the following reasons: temperature-dependency of material properties, heat sources being non-linear in temperature, and non-linear Neumann boundary conditions in terms of

temperature. But a convective cooling condition, as shown in Equation 4.2 keeps the linearity of

the problem at a constant heat transfer coefficient, h:

$$-n \cdot (q) = h(T_{inf} - T) \tag{4.2}$$

where T_{inf} represents the ambient temperature of the fluid away from the wall. In the current

model, empirically-derived heat transfer coefficients associated with external natural convection

from a vertical plate was used. The relation is given by Equation 4.3a:

$$h = \frac{k'}{L}(0.68 + \frac{0.67 Ra_L^{1/4}}{(1 + (\frac{0.492}{Pr})^{9/16})^{4/9}}) \qquad , Ra_L \leq 10^9 \tag{4.3a}$$

where L is the plate height, and Pr is the Prandtl number, i.e. $Pr = \frac{v}{\alpha}$, here v is kinematic

viscosity of the fluid and α is the thermal diffusivity of the fluid, and k' is thermal conductivity of

the fluid ($T > T_{inf}$). The Rayleigh number, Ra_L, is a dimensionless ratio associated with

buoyancy-driven flow, or free convection, and is expressed as:

$$Ra_L = \frac{g\beta(T - T_{inf})L^3}{v\alpha} \tag{4.3b}$$

where g is the acceleration due to gravity and β is the coefficient of thermal expansion of fluid.

Similarly, Surface-to-ambient radiation feature in COMSOL was utilized as one of the boundary

conditions. This condition may be written as:

$$-n \cdot (q) = \varepsilon\sigma(T_{inf}^4 - T^4) \tag{4.4}$$

where ε is the material emissivity (0.85 for bulk PDMS), and σ is the Stefan-Boltzmann constant.

Note that this radiative condition is strongly non-linear.

Preliminary simulations of transient heat transfer in this work considered a 2-D finite slab where

conduction was the primary heat transfer mechanism which changes the temperature over time.

The domain of the slab was defined between $x = -b$ and $x = +b$, where $b = 0.5$ mm. Initial

73

temperature was T_0 over the entire domain. At $t = 0$, the temperature at boundaries was increased

to T_1 (350 K). In order to compare this model with established models in literature, the following

dimensionless variables were introduced:

$$\Theta = \frac{T_1 - T}{T_1 - T_0} \tag{4.5a}$$

$$\eta = x/b \tag{4.5b}$$

$$\tau = \alpha' t / b^2 \tag{4.5c}$$

where Θ is the dimensionless temperature, η is the dimensionless distance, τ is the dimensionless

time (Fourier number), α' is the thermal diffusivity of the slab and t is the time. The model

equation is:

$$\frac{\partial \Theta}{\partial \tau} = \frac{\partial^2 \Theta}{\partial \eta^2} \tag{4.6}$$

where initial boundary conditions are $\eta = \pm 1$ and $\Theta = 0$. Temperature as a function of position was

evaluated at dimensionless times, viz.: 0.01, 0.04, 0.1, 0.2, 0.4, and 0.6. The resulting trends

matched the profiles calculated for finite slab using the analytical solution to this problem. Figure

42 shows these results.[101]

A 2-D COMSOL model freely available on web simulated the temperature profile of a vertical

plate suspended in air. This model calculates the velocity and temperature fields due to natural

convection from the vertical plate. Surface temperatures increased from 10˚C to 100˚C when the

ambient temperature was 20 ˚C. This vertical plate model, combined with finite slab model, and

previous model developed within the group were used as the basis for the three-dimensinonal (3-

D) dual-slab model in this work.[91,102,103]
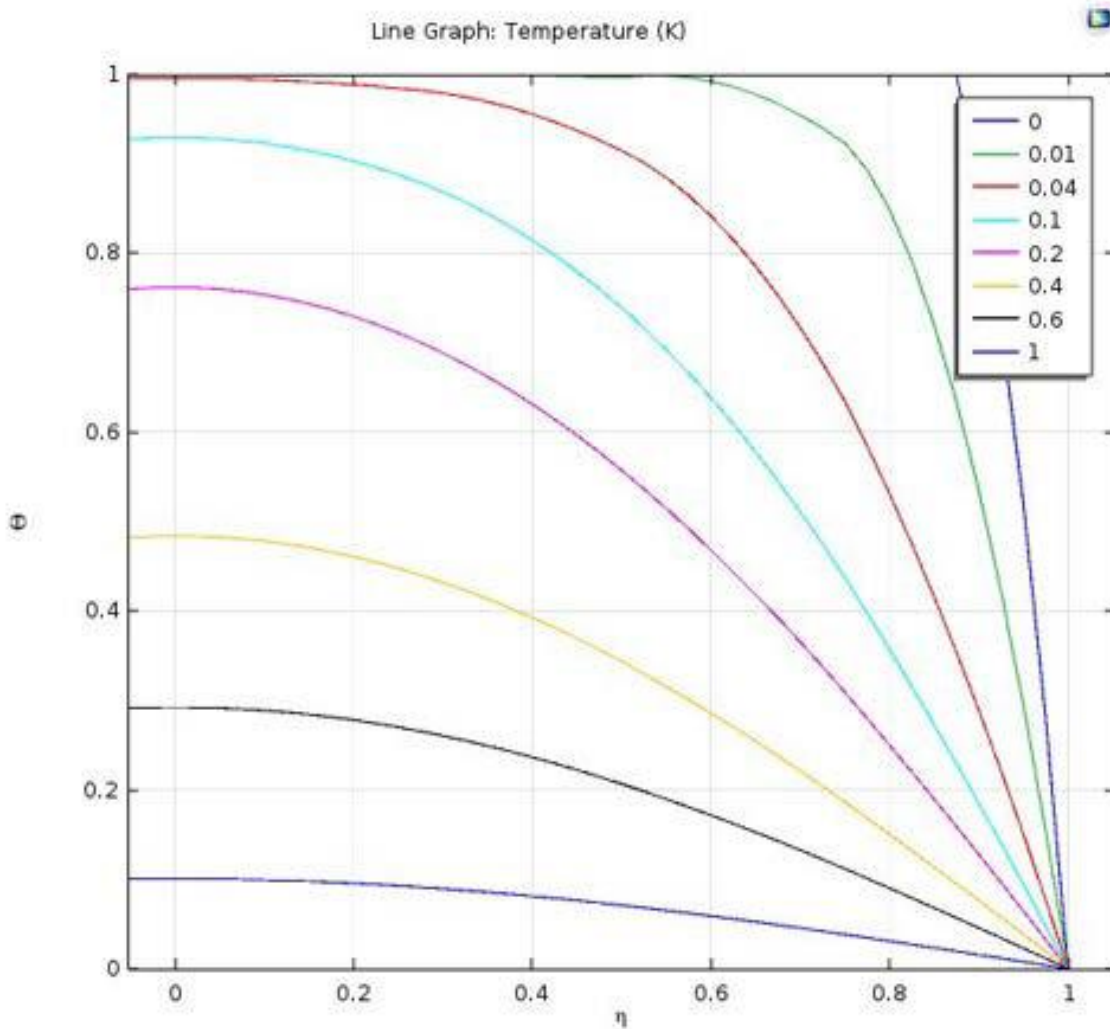
Figure 42. Temperature profile in a finite slab. The Legend shows dimensionless times.

In the current work, the 3-D model is composed of a thick film (0.32 mm for Samples b-to-e and 0.85 mm for Sample e) and a thin film of 150 nm that was overlaid on top of thick film. Here, the thin film represents the periodic lattice comprised of AuNPs. The volumetric Gaussian heat source (W m^{-3}) was provided to the thin film domain. The location of illumination and width of the Gaussian profile were designed based on experimental IR images of samples. The samples were illuminated in areas where particles were present. Controls were illuminated in matching areas as their respective samples for consistency. An equilibrium time of 160 s during heating was

considered when the temperatures in the system usually reached steady-state. The volumetric power (heat source) given in the COMSOL model represents the absorbed, extinguished power of the samples/controls. Figure 43 shows the surface temperature maps of each sample (one trial) where COMSOL profiles are compared with corresponding experimental maps at 160 s (λ_{LPR}).
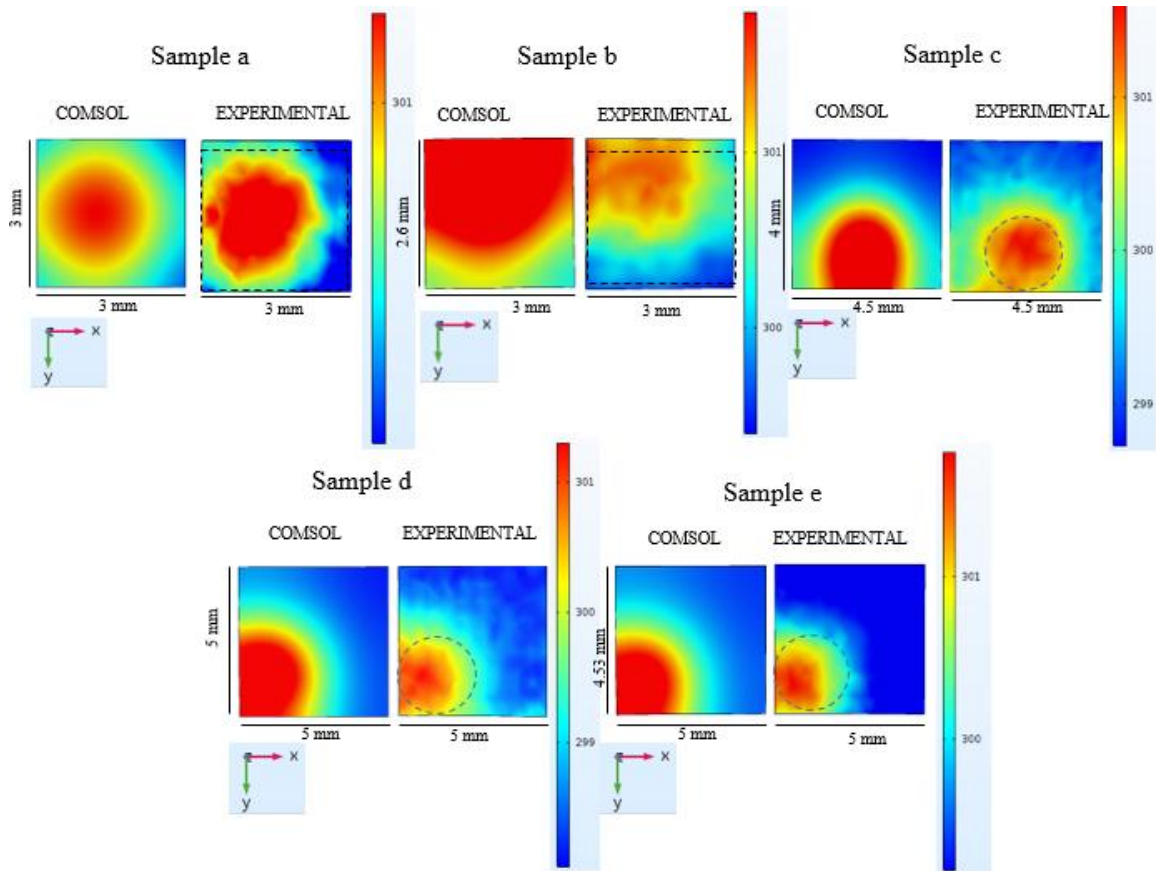
Figure 43. Surface temperature maps of Samples a-to-e generated using absorbed, extinguished powers at λ_{LPR}. The COMSOL results are compared with experimental profiles at 160 s. Dashed lines enclose particle areas.

The dashed lines overlaid on top of experimental maps represent the areas where particles self-assembled. Samples a-and-b are composed of particles in almost >70 % stamp area, whereas Samples c-e have particles at bottom-center, lower-left, and lower-left, respectively. A common color bar representing temperature scale was considered for the experimental and COMSOL

76

results for each sample. Average temperature increases at 160 s simulated in COMSOL for samples was on an average within 0.5 % (error percent) of experimental values at absorbed, extinguished powers. Figure 44 represents similar surface temperatures maps of COMSOL vs experiment at 160 s for each sample generated after using fitted absorbed, extinguished powers in mW as the
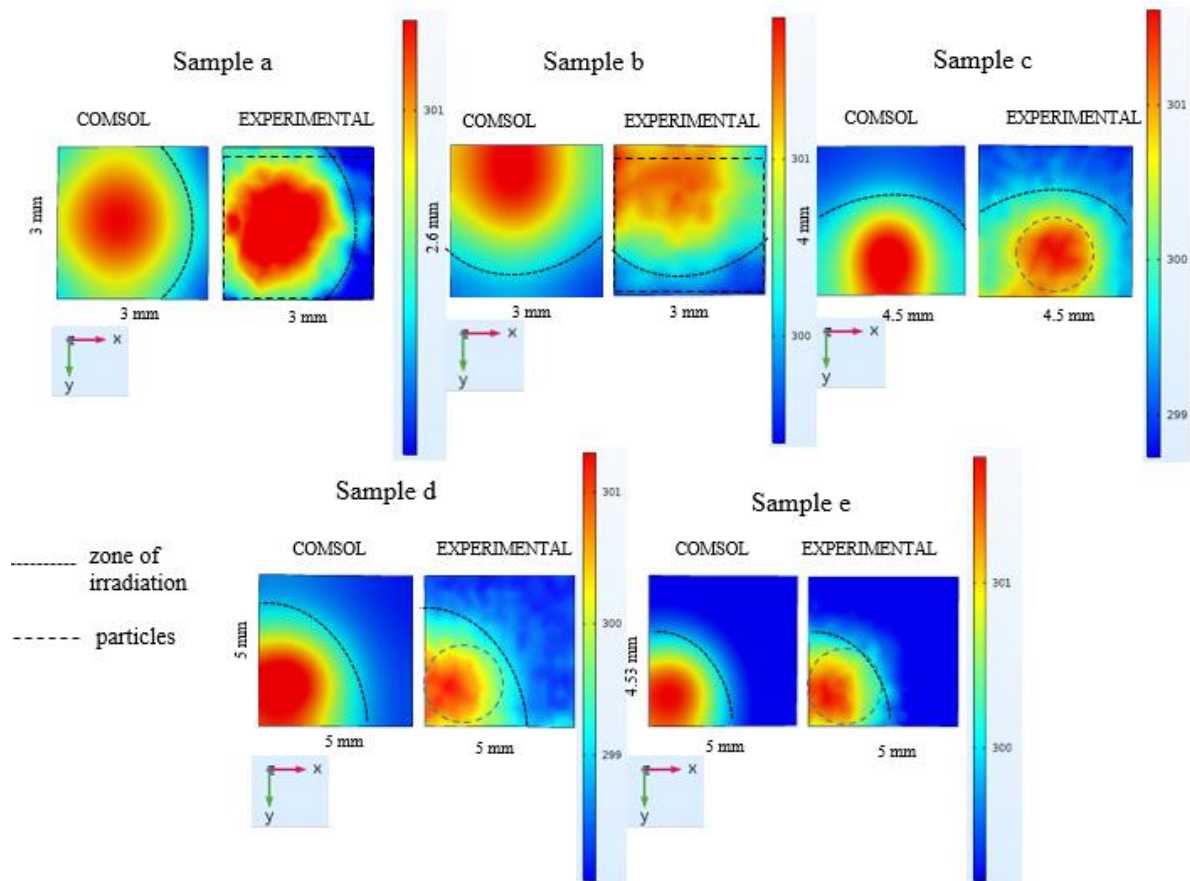
Figure 44. Surface temperature maps of Samples a-to-e generated using fitted powers at λ_{LPR}. The COMSOL results are compared with experimental profiles at 160 s. Dashed lines enclose particle areas. Dotted lines enclose irradiation zones.

input heat source (λ_{LPR}). The average temperatures (T) at 160 s were matched with experimental data by trial-and-error, and the corresponding fitted powers were noted. The dotted lines enclose the zones of radiation.

Figure 45a compares fitted powers with actual powers for sample data sets considered in Figures 43 and 44 in relation to T (average volumetric temperature at 160 s), sample area (cm^2) and number
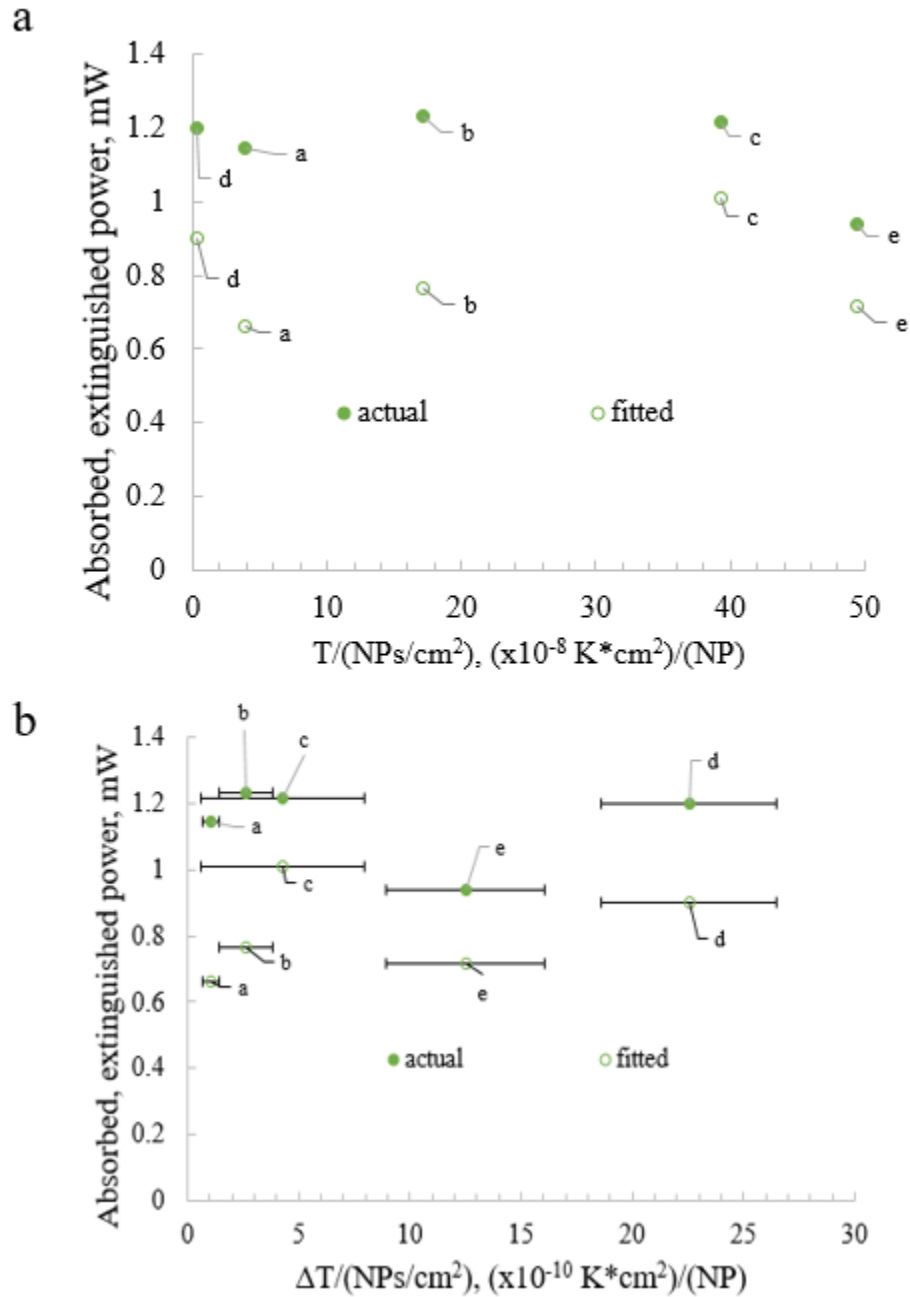
Figure 45. Fitted vs actual absorbed, extinguished powers for Samples a-to-e in relation to a) T, number of NPs, and sample area, and b) ΔT, number of NPs, and sample area

of NPs. The error % in power between fitted and actual data varied from 19 % (Sample d) to 73 % (Sample a). Figure 45b compares the fitted and actual powers based on experimental ΔT (sample temperature increase-control temperature increase) in abscissa. The error bars in abscissa were calculated using error propagation based on initial error bars in ΔT. Overall, COMSOL predicts

that lower powers (fitted) are needed to produce experimentally observed equilibrium heating temperatures (160 s). Note that accounting for reflection, diffraction, and scattering would further reduce the power actually absorbed by NPs that may give more accurate temperatures by the model. Also, the MATLAB subroutine that estimates volumetric temperature average (160 s) from experimental IR images could map temperatures in x- and y-directions. The code; however, assumes that the temperature in z-direction is constant. This may be another source of discrepancy in experimental versus COMSOL results at 160 s (0.5 % error).

4.3 Summary

The white light illumination set-up for opto-thermal measurements was illustrated. Heating and cooling over a period of 6 min were carried for each sample (and control) in triplicate at different wavelengths (λ_{LPR}; λ_{CLR}; λ_{valley}). The data corresponding to 2-D arrays with 100 nm NPs were compared with previous work involving 16 nm and 76 nm random dispersions. The extinction/NP for 2-D arrays, and 76 nm and 100 nm dispersions was up to 50-fold higher compared to 16 nm dispersions. The extinction/NP for 2-D arrays was slightly lower (2- to 6-fold) than 76 nm dispersions may be due to loss of particles to the overhead coverslip during self-assembly. Literature to date focused on AuNP-PDMS dispersions irradiated at plasmon wavelengths with laser. But opto-thermal characterization was conducted for 2-D arrays with white light as irradiation source in the current work. The temperature increase in samples relative to controls occurred at all tested wavelengths for 2-D arrays. Samples with 600 nm grating constant showed enhanced responses at λ_{LPR}, λ_{valley}, and λ_{CLR} (with and without Ge filter) relative to other samples, while all samples showed positive average thermal responses at λ_{CLR} (with Ge filter in light path). The average thermal responses for 76 nm and 100 nm random dispersions (negative controls), on the other hand, decreased from λ_{LSPR} to λ_{CLR} and touched almost zero at λ_{CLR}. Thermal responses

showed 3- to 5-fold increase at plasmon resonances with absorbed, extinguished powers relative to incident powers. Results herein suggest that 2-D arrays may be excited over a broad range of wavelengths (visible to NIR) with regular light. Experimentally measured average temperature profiles at 160 s (equilibrium) were compared to the results of 3-D COMSOL model. These temperatures were within 0.5 % at the actual absorbed, extinguished powers. Fitted powers were within 19 % (Sample d) to 73 % (Sample a) compared to actual powers at matched average temperatures (equilibrium). Overall, COMSOL mimicked experimentally measured temperature increases closely (0.5 % error).

5.   SPECIAL PROPERTIES OF 2-D ARRAYS AND THEIR APPLICATIONS

This chapter will discuss about concepts such as emergence and *critical point* of emergence which are properties of complex systems. These properties are speculated to have relevance to CLR features of 2-D metamaterial arrays, as noted in this work. The ensuing sections of this chapter will discuss various possible sustainable energy and biosensing applications of 2-D metamaterial arrays.

5.1. Complex systems, emergence, and *critical point* of emergence

Complex systems are composed of simple interacting components, which result in overall complex behavior of the system. Network theory commonly elucidates such systems as a network of nodes where the nodes denote the components and links between the nodes signify their interactions.[72] Common examples include organisms, climate, human brain, cities, universe, etc. Complex systems give rise to emergence and other distinct properties such as spontaneous order, feedback loops, adaptation, and nonlinearity, arising from relationships or interactions between their individual components and/or the environment.[104]

Complex systems are generally dissipative in nature, i.e. they tend to operate far from thermodynamic equilibrium in an environment with which interaction by exchanging matter and energy occurs. Nobel laureate Ilya Prigogine first coined the word 'disspative structures'. Often, dissipative systems are characterized by a dynamic regime in a certain reproducible steady state.[105] They differ significantly from systems close to equilibrium, which are governed by linear differential equations of entropy, i.e., entropy for an isolated adiabatic system (closed from environment) would be maximized as the system dissipates all its free energy according to the second law of classical thermodynamics. In dissipative systems, the total entropy is the summation of internal entropy and entropy exchanged with the environment and the laws of linear entropy are

violated. For example, imagine a box with molecules separated by a partition. One side has more number of molecules than the other by means of a pressure gradient from the environment; hence, the system is in a quasi-stable state far from equilibrium. Closing this system and removing the pressure gradient will allow the system to eventually reach equilibrium, thus resulting in a closed system.[105]

Emergence is a ubiquitous concept in science, arts, philosophy and systems theory, and one of the salient properties of dissipative, complex systems. Global patterns/entities for a complex system could emerge through the interactions among local entities such that a local entity alone cannot form a global pattern when it is isolated. For example, emergence of mind and its evolution is a special branch of study known as 'noogenesis' where the understanding of distinct properties of intellectual systems such as information logistics, intellectual energy, information speed, and intellectual potential *via* recapitulation theory is under pursuit by linking the development of human civilization to the evolution of human brain.[106,107]

Emergent phenomena can be found in both living (swarming, spontaneous order and self-organization in socio-economic systems, etc), and non-living systems (Bernard cells, tornadoes, weather, etc). Emergence has increasing relevance to novel technological advancements such as stigmergy-based spacecrafts,[108] multibot systems,[109] arrays or two-dimensional (2D) superlattices of NPs, etc.[110–112]

Particularly interesting property of emergent systems is the resilience to single-point failure, and prevalence of global patterns despite the failure of one or more individual entities as long as the system is above the 'critical point'.[111] Critical point may be the minimum number of individual entities necessary to interact and result in emergence of a global pattern/entity. Self-organized criticality (SOC) is an attribute of dynamical systems that have a critical point as an attractor.[113]

As Schrodinger hypothesized, order can arise from disorder in dissipative systems,[114] and this could be markedly observed in magnetically frustrated $ZnCr_2O_4$ where emergence of atypical composite spin degrees of freedom occur at a 'critical' low-temperature spin correlation length.[115,116] Reversible changes in optical properties of 2D super lattices of Ag and AuNPs by pressure-induced decreases in inter-particle spacing below the critical separation distance was recently reported.[110–112] Also, *in silico* simulations using string theory recently showed that increasing the fermion density above a quantum critical point would lead to the emergence of unusual Fermi liquid features.[117]

The results presented herein include the observation of emergence of CLR feature in 2-D arrays of optically active nodes. As indicated in Figure 17, a minimum number of optically active nodes concatenated in a chain may be needed for giving observable CLR features.

Also, *a posteriori* spectroscopic observation during real-time self-assembly in a ca. 200 x 200 microns' area of Type 2 lattice over a 3 h period of AuNP solvent evaporation suggested initial presence of LPR (550-560 nm) feature at 4 min of elapsed time post-sandwiching the AuNP drop between the stamp and the cover slip (Case b), the evolution of CLR peak (ca. 775 nm) within 15 min, stable increase and plateauing of CLR peak magnitude, and involution of CLR and LPR peaks. The time of involution was directly proportional to the rate of evaporation or receding of contact line. Spectral data was captured at six minute intervals from the same initial area of focus. At close to 136 min elapsed time, contact line completely receded past the area of focus. Figure 46 shows a glimpse of three spectra and evolution (dark blue arrow) and involution (light blue arrow) of CLR peaks. The CLR peak is enclosed inside a dashed red box. Note that similar trends were observed in supplementary trials. The 20x microscope objective in diascopic mode was focused on a plane at/near the focal plane corresponding to the stamp when the spectra were

captured. Still, the liquid layer on the stamp with particles was visible as its focal plane seemed to have overlapped with the plane of the stamp. During involution of resonances, particles present at the center of the area moved away to the contact lines, thereby causing a concentration gradient, as illustrated in Figure 9. This eventually resulted in depletion of particle concentration at the center of the FOI. It is speculated that a critical point within the 15 min elapsed time period might be associated with an interesting order in the stochastic movement of particles for a CLR peak to emerge, followed by its involution after the critical point of ordering was lost when the contact line receded.
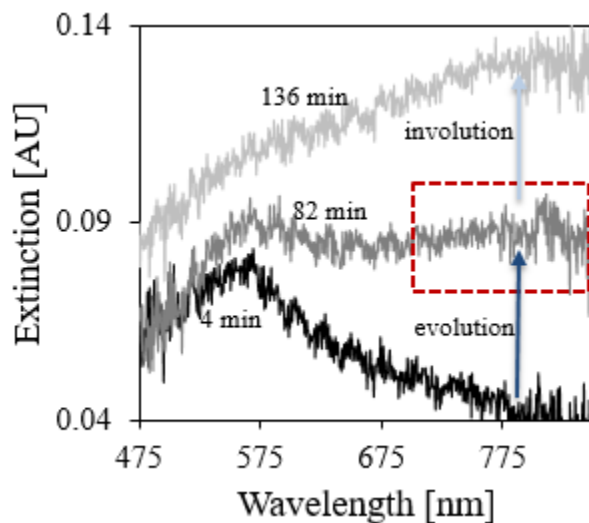
Figure 46. Initial occurrence of LPR followed by evolution (dark blue arrow) of CLR (red dashed box), and involution (light blue arrow) of CLR (ca. 775 nm) and LPR peaks.

5.2. Applications of 2-D arrays

5.2.1. Plasmonic pervaporation for biofuel recovery

Pervaporation allows chemical separations based on the partial pressure differences of components between the feed and permeate sides. Individual components diffuse into the membrane, and are obtained on the permeate side which is generally exposed to vacuum. High operating costs

associated with pervaporation result from heating the feed side continuously for providing a thermal gradient for separation. Unusual thermal properties of 2-D arrays observed at λ_{CLR} could offer alternate energy dissipation mechanisms in membranes compared to random dispersions for sustainable and scalable, plasmon-mediated pervaporation of butanol.[102,118] Enhanced plasmonic conversion to heat is desirably one of the salient objectives envisioned for these non-porous membranes. Increasing the membrane temperature is anticipated to increase the driving force. In lieu of uniform AuNP dispersion in the membrane with manifold AuNP layers, a singular lattice as discussed in this work could offer a tantamount plasmonic energy dissipation over an excitation bandwidth spanning visible to NIR regions. Also, a thin layer of AuNPs should result in enhanced mass transport across the membrane compared to a densely packed membrane. Another advantage of having a singular lattice is, concentration limits and NP aggregation associated with random dispersions can be prevented. Also, random dispersions have a high resistance to convective heat transfer with increase in characteristic length according the Biot number relation. Overall, incorporation of 2-D metamaterial arrays in membranes for pervaporation is speculated to increase the flux when irradiated over a broad range, i.e., visible to NIR, with regular white light instead of a laser. This could significantly decrease the operating costs and energy requirements of plasmonic pervaporation.

5.2.2. Ordered 2-D AuNP arrays and transition metal dichalcogenide (TMD) heterostructures

Monolayer (6.5 Å thick) TMDs with hexagonal structures are atomically thin, direct bandgap semiconductors of the kind MX_2 where M (molybdenum, tungsten, etc.) is a transition metal and X is a chalcogen atom (sulphur, selenium, or tellurium). These monolayers can be fabricated by exfoliation, chemical vapor deposition, and molecular beam epitaxy. TMD monolayers generally

have a direct bandgap, i.e., the lowest energy state in the conduction band and the highest energy state in the valence band have similar crystal momentum (k-vector) in the Brillouin zone (primitive cell in a reciprocal lattice similar to a Wigner-Seitz cell in the real Bravais lattice). This feature enables monolayer TMDs to have applications in optics as emitters and detectors, and electronics as field-effect transistors. [119,120]

Also, strong spin-orbital coupling, i.e., formation of a strong energy splitting between spin up and down states, or absence of degeneracy, occurs in the valence and conduction bands. Monolayer TMDs can absorb photons with energy $\geq$ its bandgap and are typically efficient emitters, too. Direct emission occurs in the form of three transitions called A, B, and C. Here, A and B have similar K but distinct spin-orbital coupling energy. [120]

Other interesting properties of monolayer or odd number layers of TMDs include absence of inversion center (non-centrosymmetric nature) which gives rise to important consequences. The first consequence is the formation of new degrees of freedom charge carriers that paved the path for a new field referred to as *valleytronics* whose name was derived from a blooming field of physics called *spintronics*.[121] The former involves utilizing the wave multiple extrema (maxima/minima) of the band structure for storing quantum information as discrete values of the crystal momentum. The latter involves spin states serving as the degrees of freedom for storing quantum data. The second consequence of non-centrosymmetry in TMDs involves the occurrence of non-linear optical phenomena known as second harmonic generation (SHG), which is a frequency doubling mechanism when the crystal is excited by a laser.[120] In addition to these properties, TMDs are susceptible to hot carrier injection (HCI) or hot electron transfer when they are in the presence of a metal. HCI is characterized by the movement of an electron or a "hole" (note that electron-hole pairs are quasi-particles generally referred to as excitons), owing to an

increase in kinetic energy, across a potential barrier (Schottky barrier) necessary to break an interface state. Here, "hot" refers to the effective temperature associated with the modeling of carrier density, but not the temperature of the system. [119,120]

Recent work within the group specifically focused on studying the SHG and HCI properties associated with TMDs in the presence of noble metal nanoantenna. The excitation and damping pathways of LSPR in heterostructures of Au nanoantenna and molybdenum- or tungsten-disulfide (MoS_2; WS_2) monolayers were investigated utilizing discrete dipole approximations (DDA) to Maxwell's equations, near-field electron energy loss (EELS), and far-field optical transmission UV-visible spectroscopy. For a Au (20 nm)-WS_2 heterostructure, conversion of resonant irradiation to injection of plasmonic hot electrons into the TMD was associated with a 11±5% quantum efficiency. Quantum efficiency represents damping of LSPR in the form of hot electron transfer relative to all other damping mechanisms. Also, second-order nonlinear frequency conversion process was reported for MoS_2 and WS_2, respectively, as measured by Hyper Rayleigh Scattering.[102,122–124]

Emergent far-field diffractive coupling (CLR) due to NP lattices could further enable order-of-magnitude enhancements of SHG in TMD monolayers, as reported recently in literature, where irradiation at the λ_{CLR} of a Au dimer lattice enriched the SHG signal by 30x.[125] Another report demonstrated 25x enrichment of photoluminescence from monolayer molybdenum diselenide ($MoSe_2$) by the CLR of a Au nanorod lattice.[126] Inking 2-D metamaterial arrays of AuNPs onto TMD monolayers for increasing SHG and hot electron transfer, for example, may offer enhanced energy dissipation pathways at λ_{CLR} and λ_{LPR} for next generation optoelectronics.

Furthermore, both chemically exfoliated metallic MoS_2 sheets and metal NP-decorated MoS_2 could effectively promote the efficiency of hydrogen evolution reaction (HER), as reported

recently. The photocatalytic activity of MoS$_2$ in the hydrogen evolution reaction was enhanced with plasmonic hot electron injection from Ag-Au nanorattles to MoS$_2$, thereby causing 2H-to-1T MoS$_2$ phase transition. Enhanced conductivity and reduced potential energy was overall demonstrated for this plasmon-enriched MoS$_2$ HER photocatalysis.[127]

5.2.3. Nanopore fabrication *via* dielectric breakdown for biosensing

Solid-state and biological nanopores for label-free single molecule detection,[128] DNA sequencing,[129] and protein-receptor binding[130] are of growing interest, owing to their robustness, versatility, portability and low capital costs. Attempts for *in situ* nanopore fabrication have been tried based on the effect of dielectric breakdown, where a transmembrane voltage induces an electric field that causes local failure in the dielectric membrane. The nanopore size can be modulated *via* short voltage pulses.[131,132] Plasmonic solid-state nanopores, in particular, present novel opportunities for cost-effective and high throughput promotion of dielectric breakdown. For example, Au bowtie nanoantennas gave rise to enhanced local electromagnetic fields at the nanoscale volume (hotspot) of a nanopore through which biomolecules can transmigrate when a direct current electric field was applied across a thin membrane under simultaneous optical illumination of the nanoantenna.[133] Integration of 2-D arrays of NPs with membranes could offer enhanced fields using infrared light at λ_{CLR} for dielectric breakdown at economical prices.

5.3. Summary

Concepts such as emergence and critical point of emergence in complex systems were discussed. The emergence of CLR feature even prior to LPR feature from a FOI containing a chain size of 5 active nodes suggested a plausible critical point of emergence for CLR feature in 2-D arrays (current work). This idea was further bolstered by spectroscopic observation of evolution and

involution of CLR and LPR features during the self-assembly process. Applications of 2-D arrays pertaining to plasmonic pervaporation for cost-effective biofuel recovery, optoelectronics and photocatalysis, and plasmon-induced dielectric breakdown were discussed.

6. CONCLUSIONS AND FUTURE DIRECTIONS

6.1 Summary

This work examined opto-thermal effects at plasmon and off-resonances in PDMS-PEO lattices of nanoimprinted cavities populated with AuNPs. Distinguishable temperature contributions at wavelengths corresponding to LPR (545-570 nm), valleys (650-670), and CLR (745-780 nm) were reported for the first time. Facile, bottom-up, and economical approach of template-assisted self-assembly delineated in Chapter 2 guided the deposition of particles into the cavities of PDMS-PEO. All-optical, mesoscopic characterization using episcopic and diascopic microscopy, and trichromatic particle analysis based on photometric properties of optically active nodes (luma) in Chapter 4 allowed extensive characterization of 2-D arrays at differential apertures, and correlation of optical signals with population of active nodes (AuNP-filled cavities). This technique further allowed characterization of 2-D arrays at the smallest aperture in episcopic mode that led to the speculation that a critical point of emergence for CLR peak may exist based on a minimum number of active nodes present in the lattice. Chapter 5 discussed about the results pertaining to temperature increases in these arrays at different wavelengths. Previously measured thermal responses corresponding to random particle dispersions were compared with the performance of 2-D arrays. In addition to showing thermal signatures at plasmon wavelengths, thermal signatures were obtained for 2-D arrays when illuminated with NIR light. A 3-D COMSOL model was developed that was tuned to successfully mimic the performances of these systems. The fabrication, characterization, and modeling of 2-D arrays developed herein supports design of resonant thermoplasmonic systems that have applications pertaining to sustainable energy and healthcare (Chapter 5).

6.2 Future Directions

Interesting thermal properties of 2-D metamaterials arrays observed at plasmon and off-resonances could assist in design of specialized membranes for plasmonic pervaporation that may allow alternate energy dissipation pathways and increased separation performance.[102,118]

Transfer of ordered arrays from PDMS-PEO lattice to a substrate coated with monolayer TMD could provide order-of-magnitude improvements in hot-electron transfer, photoluminescence, and SHG for applications concerning optoelectronics. [102,122–126] Preliminary results in the group related to transfer of AuNPs from PDMS-PEO to a charged glass proved to be successful (Section 3.4, Chapter 3).

Furthermore, CDA can be used to extract the absorption fractions of 2-D arrays at CLR and valley wavelengths to calculate absorbed, extinguished powers. This may allow detailed examination of thermal responses at off-resonances. A thermal model pertaining to heating in 2-D arrays that takes into account external and internal dissipation rates and allows to calculate heating and cooling time constants could be developed. Incorporating a combination of neutral density filter (200-1200 nm) and Ge filter into the current white light illumination set-up may prevent abnormal temperature spikes and any deleterious scattering effects. Opto-thermal results pertaining to irradiation of 2-D arrays with laser will be interesting to compare with the results obtained in the current work with white light source. Studies on characteristic length of 2-D arrays may be useful in considerations of future heat transfer models.

Finally, DDA coupled with rsa-CDA can be further used to study the optical responses of arrays based on different spatial conformations inside the cavities. Field enhancements of NP arrays on TMD monolayers could also be additionally explored using these computational tools.

REFERENCES

1. Chen, J., Shi, H., Sivakumar, B. & Peart, M. R. Population, water, food, energy and dams. *Renew. Sustain. Energy Rev.* **56,** 18–28 (2016).

2. Wagner, L., Ross, I., Foster, J. & Hankamer, B. Trading off global fuel supply, CO2 emissions and sustainable development. *PLoS One* **11,** e0149406 (2016).

3. Narbel, P. A. & Hansen, J. P. Estimating the cost of future global energy supply. *Renew. Sustain. Energy Rev.* **34,** 91–97 (2014).

4. Shafiee, S. & Topal, E. When will fossil fuel reserves be diminished? *Energy Policy* **37,** 181–189 (2009).

5. van Vuuren, D. P. *et al.* Energy, land-use and greenhouse gas emissions trajectories under a green growth paradigm. *Glob. Environ. Chang.* **42,** 237–250 (2017).

6. Newman, P. Decoupling economic growth from fossil fuels. *Mod. Econ.* **8,** 791–805 (2017).

7. Tummala, A., Velamati, R. K., Sinha, D. K., Indraja, V. & Krishna, V. H. A review on small scale wind turbines. *Renew. Sustain. Energy Rev.* **56,** 1351–1371 (2016).

8. Lund, J. W. & Boyd, T. L. Direct utilization of geothermal energy 2015 worldwide review. *Geothermics* **60,** 66–93 (2016).

9. Jang, Y. H. *et al.* Plasmonic solar cells: From rational design to mechanism overview. *Chem. Rev.* **116,** 14982–15034 (2016).

10. Watanabe, M. & Tryk, D. A. in *Electrochemical science for a sustainable society* 51–94 (Springer International Publishing, 2017). doi:10.1007/978-3-319-57310-6_3

11. Hajjari, M., Tabatabaei, M., Aghbashlo, M. & Ghanavati, H. A review on the prospects of sustainable biodiesel production: A global scenario with an emphasis on waste-oil biodiesel utilization. *Renew. Sustain. Energy Rev.* **72,** 445–464 (2017).

12. Chu, S. & Majumdar, A. Opportunities and challenges for a sustainable energy future. *Nature* **488,** 294–303 (2012).

13. Reineck, P., Brick, D., Mulvaney, P. & Bach, U. Plasmonic hot electron solar cells: The effect of nanoparticle size on quantum efficiency. *J. Phys. Chem. Lett.* **7,** 4137–4141 (2016).

14. Wang, X. *et al.* Simple fabrication of pineapple root-like palladium-gold catalysts as the high-efficiency cathode in direct peroxide-peroxide fuel cells. *J. Colloid Interface Sci.* **498,** 239–247 (2017).

15. Boltasseva, A. & Atwater, H. A. Low-loss plasmonic metamaterials. *Science.* **331,** 290–291 (2011).

16. Ozbay, E. Plasmonics: Merging photonics and electronics at nanoscale dimensions. *Science.* **311,** 189–193 (2006).

17. Andrew N. Shipway Eugenii Katz, I. W. Nanoparticle arrays on surfaces for electronic, optical, and sensor applications. *ChemPhysChem* **1,** 18–52 (2000).

18. Zhao, W., Brook, M. A. & Li, Y. Design of gold nanoparticle-based colorimetric biosensing assays. *ChemBioChem* **9,** 2363–2371 (2008).

19. Tiwari, P. M., Vig, K., Dennis, V. a. & Singh, S. R. Functionalized gold nanoparticles and their biomedical applications. *Nanomaterials* **1,** 31–63 (2011).

20. Zhu, Y., Ramasamy, M. & Yi, D. K. Antibacterial activity of ordered gold nanorod arrays. *ACS Appl. Mater. Interfaces* **6,** 15078–15085 (2014).

21. Saha, K., Agasti, S. S., Kim, C., Li, X. & Rotello, V. M. Gold nanoparticles in chemical and biological sensing. *Chem. Rev.* **112,** 2739–2779 (2012).

22. Hu, M. *et al.* Gold nanostructures: engineering their plasmonic properties for biomedical applications. *Chem. Soc. Rev.* **35,** 1084 (2006).

23. Ghosh, P., Han, G., De, M., Kim, C. K. & Rotello, V. M. Gold nanoparticles in delivery applications. *Adv. Drug Deliv. Rev.* **60,** 1307–1315 (2008).

24. Willets, K. a & Duyne, R. P. Van. Localized surface plasmon resonance spectroscopy and sensing. *Annu. Rev. Phys. Chem.* **58,** 267–297 (2007).

25. Barnes, W. L., Dereux, a. & Ebbesen, T. W. Surface plasmon subwavelength optics. *Nature* **424,** 824–30 (2003).

26. Theivasanthi, T. & Alagar, M. Anti-bacterial studies of silver nanoparticles. *arXiv* **1101,** 5 (2011).

27. Lisunova, M. *et al.* Modulation of plasmonic Fano resonance by the shape of the nanoparticles in ordered arrays. *J. Phys. D. Appl. Phys.* **46,** 485103 (2013).

28. DeJarnette, D., Norman, J. & Roper, D. K. Attribution of Fano resonant features to plasmonic particle size, lattice constant, and dielectric wavenumber in square nanoparticle lattices. *Photonics Res.* **2,** 15–23 (2014).

29. Forcherio, G. T., Blake, P., DeJarnette, D. & Roper, D. K. Nanoring structure, spacing, and local dielectric sensitivity for plasmonic resonances in Fano resonant square lattices. *Opt. Express* **22,** 17791–17804 (2014).

30. Cortie, M. B., Xu, X., Chowdhury, H., Zareie, H. & Smith, G. Plasmonic heating of gold nanoparticles and its exploitation. in (ed. Al-Sarawi, S. F.) 565 (2005). doi:10.1117/12.582207

31. Voisin, C., Del Fatti, N., Christofilos, D. & Vallée, F. Ultrafast electron dynamics and optical nonlinearities in Metal nanoparticles. *J. Phys. Chem. B* **105,** 2264–2280 (2001).

32. Grua, P., Morreeuw, J. P., Bercegol, H., Jonusauskas, G. & Vallée, F. Electron kinetics and emission for metal nanoparticles exposed to intense laser pulses. *Phys. Rev. B* **68,** 35424 (2003).

33. Theis, T. N. & Wong, H.-S. P. The end of Moore's law: A new beginning for information technology. *Comput. Sci. Eng.* **19,** 41–50 (2017).

34. Bejugam, V., Wei, X. & Roper, D. K. Reductive spectrophotometry of divalent tin sensitization on soda lime glass. *Applied Surface Science* **376,** 43–51 (2016).

35. Fano, U. Effects of configuration interaction on intensities and phase shifts. *Phys. Rev.* **124,** 1866–1878 (1961).

36. DeJarnette, D., Jang, G. G., Blake, P. & Roper, D. K. Polarization angle affects energy of plasmonic features in Fano resonant regular lattices. *J. Opt.* **16,** 105006 (2014).

37. Félidj, N. *et al.* Grating-induced plasmon mode in gold nanoparticle arrays. *J. Chem. Phys.* **123,** 221103 (2005).

38. Auguié, B., Bendaña, X. M., Barnes, W. L. & García De Abajo, F. J. Diffractive arrays of gold nanoparticles near an interface: Critical role of the substrate. *Phys. Rev. B - Condens. Matter Mater. Phys.* **82,** 155447 (2010).

39. DeJarnette, D., Roper, D. K. & Harbin, B. Geometric effects on far-field coupling between multipoles of nanoparticles in square arrays. *J. Opt. Soc. Am. B* **29,** 88–100 (2012).

40. Dejarnette, D., Norman, J. & Roper, D. K. Spectral patterns underlying polarization-enhanced diffractive interference are distinguishable by complex trigonometry. *Appl. Phys. Lett.* **101,** 183104 (2012).

41. Wang, X., Gogol, P., Cambril, E. & Palpant, B. Near- and far-field Effects on the plasmon coupling in gold nanoparticle arrays. *J. Phys. Chem. C* **116,** 24741–24747 (2012).

42. Halas, N. J., Lal, S., Chang, W.-S., Link, S. & Nordlander, P. Plasmons in strongly coupled metallic nanostructures. *Chem. Rev.* **111,** 3913–61 (2011).

43. Joe, Y. S., Satanin, A. M. & Kim, C. S. Classical analogy of Fano resonances. *Phys. Scr.* **74,** 259–266 (2006).

44. Francescato, Y., Giannini, V. & Maier, S. A. Plasmonic systems unveiled by fano resonances. *ACS Nano* **6,** 1830–1838 (2012).

45. Giannini, V., Francescato, Y., Amrania, H. & Phillips, C. Fano resonances in nanoscale plasmonic systems a parameter-free modeling approach. *Nano* **11,** 2835–2840 (2011).

46. Miroshnichenko, A. E., Flach, S. & Kivshar, Y. S. Fano resonances in nanoscale structures. *Rev. Mod. Phys.* **82,** 2257–2298 (2010).

47. Blake, P., Ahn, W. & Roper, D. K. Enhanced uniformity in arrays of electroless plated spherical gold nanoparticles using tin presensitization. *Langmuir* **26,** 1533–8 (2010).

48. Altissimo, M. E-beam lithography for micro-/nanofabrication. *Biomicrofluidics* **4,** 26503 (2010).

49. Langford, R. M. Focused ion beam nanofabrication: A comparison with conventional processing techniques. *J. Nanosci. Nanotechnol.* **6,** 661–668 (2006).

50. Nagpal, P., Lindquist, N. C., Oh, S.-H. & Norris, D. J. Ultrasmooth patterned metals for plasmonics and metamaterials. *Science* **325,** 594–7 (2009).

51. Colson, P., Henrist, C. & Cloots, R. Nanosphere lithography: A powerful method for the controlled manufacturing of nanomaterials. *J. Nanomater.* **2013,** 1–19 (2013).

52. Ahn, W. & Roper, D. K. Periodic nanotemplating by selective deposition of electroless gold island films on particle-lithographed dimethyldichlorosilane layers. *ACS Nano* **4,** 4181–9 (2010).

53. Viheriälä, J., Niemi, T., Kontio, J. & Pessa, M. in *Recent Optical and Photonic Technologies* 275–298 (2010). doi:10.5772/6917

54. McAlpine, M. C., Friedman, R. S. & Lieber, C. M. Nanoimprint lithography for hybrid plastic electronics. *Nano Lett.* **3,** 443–445 (2003).

55. Schift, H. Nanoimprint lithography: An old story in modern times? A review. *J. Vac. Sci. Technol. B Microelectron. Nanom. Struct.* **26,** 458 (2008).

56. Xia, Y. & Whitesides, G. M. Soft lithography. *Annual Review of Materials Science* **28,** 153–184 (1998).

57. Mcphillips, J. *et al.* Plasmonic sensing using nanodome arrays fabricated by soft nanoimprint lithography. 15234–15239 (2011).

58. Chen, K., Duy Dao, T. & Nagao, T. Tunable nanoantennas for surface enhanced infrared absorption spectroscopy by colloidal lithography and post-fabrication etching. *Sci. Rep.* **7,** 44069 (2017).

59. Fan, J. a. *et al.* Plasmonic mode engineering with templated self-assembled nanoclusters. *Nano Lett.* **12,** 5318–5324 (2012).

60. Malaquin, L., Kraus, T., Schmid, H., Delamarche, E. & Wolf, H. Controlled particle placement through convective and capillary assembly. *Langmuir* **23,** 11513–11521 (2007).

61. Yin, Y., Gates, B. & Xia, Y. Template assisted assembly: A practical route to complex aggregates of monodispersed colloids with well-defined sizes, spheres and structures. *J. Am. Chem. Soc.* **123,** 8718–8729 (2001).

62. Juillerat, F., Solak, H. H., Bowen, P. & Hofmann, H. Fabrication of large-area ordered arrays of nanoparticles on patterned substrates. *Nanotechnology* **16,** 1311–1316 (2005).

63. Cui, Y. *et al.* Integration of colloidal nanocrystals into lithographically patterned devices. *Nano Lett.* **4,** 1093–1098 (2004).

64. Kraus, T. *et al.* Nanoparticle printing with single-particle resolution. *Nat. Nanotechnol.* **2,** 570–6 (2007).

65. Hillborg, H. & Gedde, U. Hydrophobicity changes in silicone rubbers. *IEEE Trans. Dielectr.* **6,** 703–717 (1999).

66. Vargaftik, N. B., Volkov, B. N. & Voljak, L. D. International tables of the surface tension of water. *J. Phys. Chem. Ref. Data* **12,** 817–820 (1983).

67. Zhou, J., Ellis, A. V. & Voelcker, N. H. Recent developments in PDMS surface modification for microfluidic devices. *Electrophoresis* **31,** 2–16 (2010).

68. Wong, I. & Ho, C. M. Surface molecular property modifications for poly (dimethylsiloxane)(PDMS) based microfluidic devices. *Microfluid. Nanofluidics* **7,** 291–306 (2009).

69. Yao, M. & Fang, J. Hydrophilic PEO-PDMS for microfluidic applications. *J. Micromechanics Microengineering* **22,** 25012 (2012).

70. Yu, K. & Han, Y. A stable PEO-tethered PDMS surface having controllable wetting property by a swelling-deswelling process. *Soft Matter* **2,** 705 (2006).

71. Sperling, R. A. & Parak, W. J. Surface modification, functionalization and bioconjugation of colloidal inorganic nanoparticles. *Philos. Trans. R. Soc. London A Math. Phys. Eng. Sci.* **368,** (2010).

72. Arenas, A., Díaz-Guilera, A., Kurths, J., Moreno, Y. & Zhou, C. Synchronization in complex networks. *Phys. Rep.* **469,** 93–153 (2008).

73. Young, T. On the theory of light and colours. *Phil. Trans. R. Soc. Lond.* **92,** 12–48 (1802).

74. Poynton, C. A. *Digital Video and HDTV : Algorithms and Interfaces*. (Elsevier, 2012).

75.   ITU-R. BT.601: Studio encoding parameters of digital television for standard 4:3 and wide screen 16:9 aspect ratios. (2013). Available at: http://www.itu.int/rec/R-REC-BT.601/. (Accessed: 1st August 2016)

76.   Chen, G. H. *et al.* Detection of mercury(II) ions using colorimetric gold nanoparticles on paper-based analytical devices. *Anal. Chem.* **86,** 6843–6849 (2014).

77.   Cheng, X. *et al.* Color difference amplification between gold nanoparticles in colorimetric analysis with actively controlled multiband illumination. *Anal. Chem.* **86,** 7584–7592 (2014).

78.   King, N. S. *et al.* Fano resonant aluminum nanoclusters for plasmonic colorimetric sensing. *ACS Nano* **9,** 10628–10636 (2015).

79.   ImageJ. US National Institutes of Health, Bethesda, MD.

80.   Bejugam, V., French III, R. T., Forcherio, G. T. & Roper, D. K. *Optical characteristics of a lattice resonance supported by plasmonic nanoparticles deposited sparsely in a nanoimprinted polymer. In Progress.*

81.   French III, R. T. Characterization of coupled gold nanoparticles in a sparsely populated square lattice. (University of Arkansas, 2017).

82.   Mie, G. Pioneering mathematical description of scattering by spheres [J]. *Ann. Phys. (N. Y).* **25,** 337 (1908).

83.   Wriedt, T. in *Springer Series in Optical Sciences* **169,** 53–71 (Springer, Berlin, Heidelberg, 2012).

84.   nanoComposix · Plasmonics. Available at: http://nanocomposix.com/pages/plasmonics#plasmonic-nanoparticles. (Accessed: 12th April 2017)

85.   Blake, P., Obermann, J., Harbin, B. & Roper, D. K. Enhanced nanoparticle response from coupled dipole excitation for plasmon sensors. *IEEE Sens. J.* **11,** 3332–3340 (2011).

86.   Dejarnette, D. An extension to particle polarizability to predict coupling behavior in periodic nanoplasmonic arrays. (University of Arkansas, 2012).

87.   Zou, S., Janel, N. & Schatz, G. C. Silver nanoparticle array structures that produce remarkably narrow plasmon lineshapes. *J. Chem. Phys.* **120,** 10871–10875 (2004).

88.   Berry, K. R., Dunklin, J. R., Blake, P. A. & Roper, D. K. Thermal dynamics of plasmonic nanoparticle composites. *J. Phys. Chem. C* **119,** 10550–10557 (2015).

89.   Roper, D. K. *et al.* Effects of geometry and composition of soft polymer films embedded with nanoparticles on rates for optothermal heat dissipation. *Nanoscale* **10,** 11531–11543 (2018).

90. Dunklin, J. R. & Roper, D. K. Heat dissipation of resonant absorption in metal nanoparticle-polymer films described at particle separation near resonant wavelength. *J. Nanomater.* **2017,** 1–9 (2017).

91. Dunklin, J. R., Forcherio, G. T., Berry, K. R. & Roper, D. K. Gold nanoparticle-polydimethylsiloxane thin films enhance thermoplasmonic dissipation by internal reflection. *J. Phys. Chem. C* **118,** 7523–7531 (2014).

92. Dunklin, J. R., Bodinger, C., Forcherio, G. T. & Roper, D. K. Plasmonic extinction in gold nanoparticle-polymer films as film thickness and nanoparticle separation decrease below resonant wavelength. *J. Nanophotonics* **11,** 16002 (2017).

93. Tagliabue, G., Eghlidi, H. & Poulikakos, D. Rapid-response low infrared emission broadband ultrathin plasmonic light absorber. *Sci. Rep.* **4,** 7181 (2014).

94. Li, Y., Verbiest, T. & Vankelecom, I. Improving the flux of PDMS membranes via localized heating through incorporation of gold nanoparticles. *J. Memb. Sci.* **428,** 63–69 (2013).

95. Vanherck, K., Hermans, S., Verbiest, T. & Vankelecom, I. Using the photothermal effect to improve membrane separations via localized heating. *J. Mater. Chem.* **21,** 6079 (2011).

96. Chen, Z. *et al.* Imaging local heating and thermal diffusion of nanomaterials with plasmonic thermal microscopy. *ACS Nano* **9,** 11574–11581 (2015).

97. Roper, D. K., Ahn, W. & Hoepfner, M. Microscale heat transfer transduced by surface plasmon resonant gold nanoparticles. *J. Phys. Chem. C* **111,** 3636–3641 (2007).

98. Ebadi-Dehaghani, H. & Nazempour, M. in *Smart Nanoparticles Technology* (InTech, 2012). doi:10.5772/33842

99. Wilkes, J. O. Introduction to COMSOL Multiphysics (Formerly , FEMLAB). (2009). Available at: https://cdn.comsol.com/documentation/5.3.0.316/IntroductionToCOMSOLMultiphysics.pdf. (Accessed: 25th September 2017)

100. Kothadran. *Fundamentals of Heat and Mass Transfer*. (John Wiley & Sons, 2011).

101. H. S. Carslaw, J. C. J. *Conduction of Heat in Solids, , Oxford*. (Clarendon Press, 1959).

102. Dunklin Jeremy. Plasmon-mediated energy conversion in metal nanoparticle-doped hybrid nanomaterials. (University of Arkansas, 2017).

103. Building and solving a non-isothermal laminar flow model. (2008).

104. Spurrett, D. Complexity and post-modernism: Understanding complex systems. *South African J. Philos.* **18,** 258–274 (1999).

105. Schneider, E. D. & Kay, J. J. in *Reflections on the Future of Biology* (eds. Murphy, M. & O'Neill, L.) **8,** 161–172 (Cambridge University Press, 1995).

106. Todd, P. B. Teilhard and other modern thinkers on evolution, mind, and matter. *Teilhard Studies* **66,** 1–18 (2013).

107. Chardin, P. T. De. *Pierre Teilhard de Chardin Phenomenon of Man , 1959*. (1959).

108. Tripp, H. & Palmer, P. Stigmergy based behavioural coordination for satellite clusters. *Acta Astronaut.* **66,** 1052–1071 (2010).

109. Gerkey, B. P. & Matarić, M. J. Sold!: Auction methods for multirobot coordination. *IEEE Trans. Robot. Autom.* **18,** 758–768 (2002).

110. Markovich, G. *et al.* Architectonic quantum dot solids. *Acc. Chem. Res.* **32,** 415–423 (1999).

111. Ayyub, P. Aligned nanorod arrays: Additive and emergent properties. *J. Clust. Sci.* **20,** 429–451 (2009).

112. Brust, M. Nanoparticle ensembles: Nanocrystals come to order. *Nat. Mater.* **4,** 364–365 (2005).

113. Bak, P., Tang, C. & Wiesenfeld, K. Self-organized criticality. *Phys. Rev. A* **38,** 364–374 (1988).

114. Schrödinger, E. *What is Life? The Pysical Aspect of the Living Cell*. (Cambridge University Press, 1944).

115. Lee, S. H. *et al.* Emergent excitations in a geometrically frustrated magnet. *Nature* **418,** 856–858 (2002).

116. Balents, L. Spin liquids in frustrated magnets. *Nature* **464,** 199–208 (2010).

117. Cubrovic, M., Zaanen, J. & Schalm, K. String theory, quantum phase transitions, and the emergent Fermi liquid. *Science.* **325,** 439–444 (2009).

118. Russell, A. Plasmonic pervaporation via gold nanoparticle- functionalized nanocomposite membranes. (University of Arkansas, 2012).

119. Wang, Q. H., Kalantar-Zadeh, K., Kis, A., Coleman, J. N. & Strano, M. S. Electronics and optoelectronics of two-dimensional transition metal dichalcogenides. *Nat. Nanotechnol.* **7,** 699–712 (2012).

120. Mak, K. F. & Shan, J. Photonics and optoelectronics of 2D semiconductor transition metal dichalcogenides. *Nat. Photonics* **10,** 216–226 (2016).

121. Xu, X., Yao, W., Xiao, D. & Heinz, T. F. Spin and pseudospins in layered transition metal dichalcogenides. *Nat. Phys.* **10,** 343–350 (2014).

122. Forcherio, G. T. Infrared energy conversion in plasmonic fields at two dimensional semiconductors. (2017).

123. Forcherio, G. T., Benamara, M. & Roper, D. K. Electron energy loss spectroscopy of hot electron transport between gold nanoantennas and molybdenum disulfide by plasmon excitation. *Adv. Opt. Mater.* **5,** 1600572 (2017).

124. Forcherio, G. T. & Roper, D. K. Spectral characteristics of noble metal nanoparticle-molybdenum disulfide heterostructures. *Adv. Opt. Mater.* **4,** 1288–1294 (2016).

125. Walsh, G. F. & Dal Negro, L. Enhanced second harmonic generation by photonic-plasmonic fano-type coupling in nanoplasmonic arrays. *Nano Lett.* **13,** 3111–3117 (2013).

126. Taghinejad, H. *et al.* Lattice plasmon induced large enhancement of excitonic emission in monolayer metal dichalcogenides. *Plasmonics* 1–7 (2016). doi:10.1007/s11468-016-0470-4

127. Kang, Y. *et al.* Plasmonic hot electron enhanced MoS_2 photocatalysis in hydrogen evolution. *Nanoscale* **7,** 4482–4488 (2015).

128. Bonome, E. L. *et al.* Multistep current signal in protein translocation through graphene nanopores. *J. Phys. Chem. B* **119,** 5815–5823 (2015).

129. Ando, G., Hyun, C., Li, J. & Mitsui, T. Directly observing the motion of DNA molecules near solid-state nanopores. *ACS Nano* **6,** 10090–10097 (2012).

130. Wei, R., Gatterdam, V., Wieneke, R., Tampé, R. & Rant, U. Stochastic sensing of proteins with receptor-modified solid-state nanopores. *Nat. Nanotechnol.* **7,** 257–263 (2012).

131. Sze, S. M. Current transport and maximum dielectric strength of silicon nitride films. *J. Appl. Phys.* **38,** 2951–2956 (1967).

132. Kwok, H., Briggs, K. & Tabard-Cossa, V. Nanopore fabrication by controlled dielectric breakdown. *PLoS One* **9,** e92880 (2014).

133. Pud, S. *et al.* Self-aligned plasmonic Nanopores by optically controlled dielectric breakdown. *Nano Lett.* **15,** 7112–7117 (2015).